INAUGURAL – DISSERTATION
zur Erlangung der Doktorwürde
der
Naturwissenschaftlich-Mathematischen
Gesamtfakultät
der
Ruprecht-Karls-Universität
Heidelberg

vorgelegt von

Mustafa Sayın

aus Trabzon, Türkei

Tag der mündlichen Prüfung
21.11.2014

Generation of Nanostructured Surfaces by Self-Assembly Strategies for Site-Selective Protein Adsorption

Gutachter:
Prof. (apl.) Dr. Reiner Dahint
Prof. Dr. Joachim Spatz

I would like to dedicate my thesis

to my wife and lovely son

TABLE OF CONTENTS

ABSTRACT

The aim of this study is to generate nanopatterned surfaces with feature sizes between 10 and 100 nm on large lateral scale in order to investigate confinement effects on the activity of adsorbed enzymes. To achieve this purpose, novel patterning techniques based on colloidal lithography were developed to generate five different types of nanopatterned surfaces: i) metal-semiconductor nanopatterns, ii) charge heterogeneous 2D and 3D nanopatterned polyelectrolyte multilayers (PEMs), iii) gold nanoparticle arrays on charge heterogeneous nanopatterned PEMs, iv) metal-dielectric hybrid nanopatterns, and v) nanopatterned oligo(ethylene)glycol silane self-assembled monolayers (SAMs). All of the fabricated nanopatterned surfaces were characterized by X-ray photoelectron spectroscopy (XPS), atomic force microscopy (AFM), scanning electron microscopy (SEM), ellipsometry and UV-visible spectroscopy.

Metal-semiconductor nanopatterns and charge heterogeneous 2D and 3D nanopatterned PEMs were chosen for protein adsorption investigations based on their excellent reproducibility and the capability to produce uniform and high density nanopatterns. Specifically, porous metal-semiconductor nanopatterns with 25 nm (type A25) and 60 nm (type A60) adsorption site diameter and honeycomb-like dielectric nanopatterns with 60 nm (type B60) and 100 nm (type B100) adsorption site diameter were fabricated to evaluate the specific enzymatic activity of surface-bound glucose oxidase (GOx). The amount of GOx adsorbed onto these nanopatterned surfaces was quantified by enzyme linked immunosorbent assays (ELISA). The specific activity of GOx on the nanopatterned surfaces was compared to the specific activity of GOx on poly(allyamine hydrochloride) coated non-patterned surfaces and in solution phase. It was found that the confinement of GOx into nano-domains of patterned substrates has a significant effect on protecting the enzymatic activity of GOx. When the adsorption site diameter was selected similar to enzyme size, the activity of the protein was well preserved and only a small loss of activity was observed. This is in line with the observation that proteins tend to unfold and lose their activity upon contact with surfaces which offer sufficient free surface area. We may therefore conclude from the study that geometrical confinement is a promising strategy to overcome this problem and stabilize surface-bound enzymes.

KURZFASSUNG

Das Ziel dieser Arbeit ist es, nanostrukturierte Oberflächen mit Strukturgrößen zwischen 10 und 100 nm großflächig herzustellen, um die Auswirkung lateralen Confinements auf die Aktivität adsorbierter Enzyme zu untersuchen. Um dieses Ziel zu erreichen, wurden neue, auf kolloidaler Lithographie basierende Strukturierungsmethoden entwickelt, um fünf verschiedene Typen von nanostrukturierten Oberflächen zu erzeugen: i) Metall-Halbleiter Nanostrukturen, ii) Ladungsheterogene 2- und 3-dimensional nanostrukturierte Polyelektrolyt-Multilagen, iii) Goldnanopartikel-Arrays auf ladungsheterogenen Polyelektrolyt-Multilagen, iv) Metall-dielektrische Hybrid-Nanostrukturen v) Nanostrukturierte selbstorganisierende Monolagen (SAMs) von Oligo(ethylengykol)-Silanen.Alle hergestellten nanostrukturierten Oberflächen wurden mittels Photoelektronenspektroskopie (XPS), Rasterkraftmikroskopie (AFM), Rasterelektronenmikroskopie (REM), Ellipsometrie und UV-Vis-Spektroskopie charakterisiert.

Metall-Halbleiter-Nanostrukturen und ladungs-heterogene 2- und 3-dimensional nanostrukturierte Polyelektrolyt-Multilagen wurden für die Untersuchungen zur Proteinadsorption ausgewählt, da sie sehr gut reproduzierbar sind und eine hohe Dichte von Nanostukturen einheitlicher Größe aufweisen. Für die Analyse der enzymatischen Aktivität oberflächengebundener Glucose-Oxidase (GOx) wurden Metall-Halbleiter-Nanostrukturen mit einem Domänendurchmesser von 25 nm (Typ A25) und 60 nm (Typ A60) sowie wabenförmige dielektrische Nanostukturen mit einem Domänendurchmesser von 60 nm (Typ B60) und 100 nm (Typ B100) hergestellt. Die auf den Nanodomänen adsorbierte Menge GOx wurde mittels enzymgekoppeltem Immunoadsorptionstest (ELISA) ermittelt. Die spezifische enzymatische Aktivität von auf den nanostrukturierten Oberflächen adsorbierter GOx wurde mit der spezifischen Aktivität von GOx auf Poly(allyamin hydrochlorid) beschichteten, nicht strukturierten Oberflächen sowie mit der spezifischen Aktivität von GOx in Lösung verglichen. Die Experimente zeigen, dass ein Confinement von GOx in Nanodomänen der strukturierten Oberfläche einen signifikanten Einfluss auf den Erhalt der enzymatischen Aktivität besitzt.

Wenn der Durchmesser des Adsorptionsplatzes ähnlich der Enzymgröße gewählt wurde, konnte die Aktivität der Proteine weitgehend erhalten werden und nur ein geringer Aktivitätsverlust wurde beobachtet. Das stimmt mit der Beobachtung überein, dass Proteine dazu neigen, sich zu entfalten und ihre Aktivität zu verlieren, sobald sie mit einer Oberfläche in Kontakt kommen, welche genug freien Raum hierfür zur Verfügung stellt. Die durchgeführten Untersuchungen lassen daher die Schlussfolgerung zu, dass räumliches Confinement eine vielversprechende Strategie darstellt, dieses Problem zu umgehen und oberflächengebundene Enzyme zu stabilisieren.

INTRODUCTION

Surface-bound biomolecules play an important role in biotechnology and biomedicine. They are used, for example, in heterogeneous immunoassays and biosensors for the specific detection of dissolved antigens, DNA and peptide chips for genome and proteome analysis, and cell membrane models[1-5]. On the other hand, non-specifically adsorbed proteins significantly affect the biocompatibility of artificial biomaterials. In order to achieve or maintain the desired function of biomolecule-decorated surfaces, the molecular conformation as well as the amount and composition of the immobilized biomolecules is crucially important[3, 5, 6].

Proteins tend to unfold and therefore lose their original functionality when they are adsorbed onto homogeneous surfaces. It is expected that unfolding can be prevented by adsorbing proteins onto nanopatterned surfaces where nanoscale adsorption sites are embedded into a protein resistant matrix as depicted in Figure1. If the lateral dimensions of the adsorption sites match the size of the protein, unfolding of the protein should be avoided and, therefore, the conformation and original functionality preserved. Furthermore, if the dimensions of the adsorption sites are deliberately tuned, this may lead to partial unfolding of the proteins resulting in partial loss of its original function. Therefore, it can be speculated that this concept of lateral protein confinement may facilitate the fabrication of surfaces with tunable biological function, providing new options in the design of tailored biofunctional surfaces.

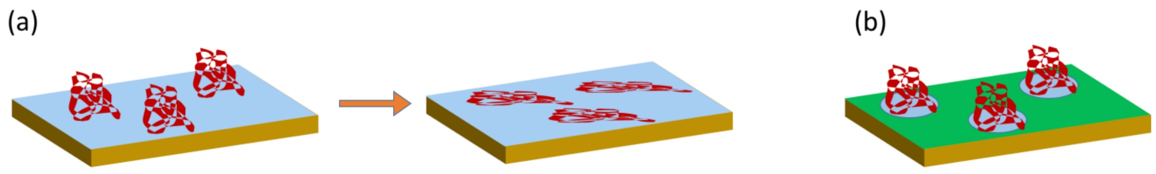

Figure 1: a) The adsorption of proteins on surfaces usually leads to their denaturation and loss of original activity. b) Embedding of nanoscale adsorption sites (blue) into an inert matrix material (green) may inhibit protein unfolding beyond the borders of the adsorption site, so that the native conformation of the protein will be stabilized.

In this thesis, several strategies for the fast and cost-effective formation of large-scale surface nanostructures via self-assembly processes were developed. Selected samples were used to investigate the impact of surface nanostructures on the activity of a surface-bound model protein, Glucose oxidase (GOx). For this purpose, GOx was confined into nanostructured surfaces with well-defined size, chemical functionality and topography of adsorption sites in order to prevent unfolding and loss of its biological function.

1 THEORY

1.1 Self-assembled monolayers

Self-assembled monolayers (SAMs) are organic assemblies which generally form spontaneously on solid surfaces by adsorption of molecular components from gas or solution phase to build up large ordered domains [7-9]. SAM consisting of a headgroup, tail and functional group is shown in Figure 1.1. The molecules forming SAMs have a chemical functionality or headgroup, which provides specific affinity for the substrate. The SAM formation on the substrate is chemisorption of molecules onto the substrate surface via the headgroups and followed by a slow organization of tail groups. The functional group determines the chemical and physical properties of SAM [7, 9-11]. Therefore, SAMs provide convenient and flexible tools for tuning the interfacial properties of metals, semiconductors and metal oxides.

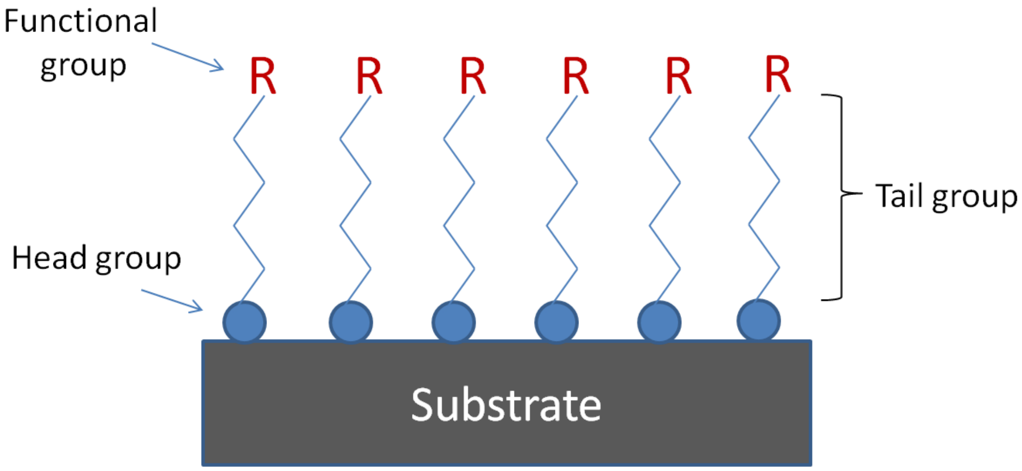

Figure 1.1: Representation of SAM structure.

SAMs are extensively used in nanoscience and nanotechnology due to their convenient preparation (ultrahigh vacuum or other sophisticated setups are not required). Moreover, SAMs have the ability to be formed on objects of all sizes to give precious functions to preformed nanoscale materials such as thin films, colloids, etc. In addition, they can change the interfacial properties of surfaces, such as wetting, adhesion and friction[7, 12].

Orgonosilicon and orgonosulfur derivatives are the most commonly used organic molecule classes for SAM production. Generally, organosilicon SAMs are prepared with alkylchlorosilanes, alkylalkoxysilanes, and alkylaminosilanes on hydroxyl terminated silicon oxide, quartz, glass, mica and germanium oxide substrates thanks to formation of Si-O-Si bonds with surface silanol groups (-SiOH). On the other hand, orgonosulfur SAMs can be formed with di-*n*-alkyl disulfides, thiophenols, mercaptopyridines, mercaptoanilines, thiophenes, cysteines, thiocarbaminates, thiocarbamates, thioureas and mercaptoimidazoles on transition metal surfaces [7, 9, 12]. Among orgonosulfur molecules, alkanethiols are widely used to form SAMs on noble metals such as gold, silver, palladium and platinum. The interaction of alkenethiols and the noble metal surfaces is through high affinity of thiol head group for the noble metal surface to provide the opportunity of generating well-defined organic surfaces with applicative and highly modifiable chemical functionalities [7, 9, 10].

1.2 Polyelectrolyte Coatings

Polyelectrolytes (PE) are polymers that carry ionizable groups in their repeating units. In polar solvents, these ionizable groups disassociate and leave their charges on the polymer chains and release the counterions into the solution[13, 14]. Polyelectrolytes can be either negatively or positively charged. Positively charged electrolytes generally carry protonated amino groups, like in poly(allyamine), poly(ethyleneimine) and poly(L-lysine). On the other hand, deprotonated acidic groups provide the negative charge of the anionic polyelectrolytes [13, 15, 16]. Polyacrylic and polymethacrylic acids and their salts, and polystyrene sulfonates are the main examples of widely used anionic polyelectrolytes.

Polyelectrolytes can be used as a flexible coatings to alter the physical and chemical properties of the surfaces by changing the surface charge to yield bonding or adsorption of different molecules, nanoparticles etc [17-19]. Moreover, polyelectrolytes can generate heterogeneously charged patterned surfaces when they are combined with suitable lithographic methods such as microcontact printing and colloidal lithography as used in this thesis. Therefore, heterogeneously charged patterned surfaces can be used for directed self-assembly of charged species such as the site specific adsorption of proteins onto charged domains or formation of negatively charged gold nanoparticle arrays (cf. section 4.2.1). Furthermore, polyelectrolytes can be employed for producing multilayer thin films known as polyelectrolyte multilayers (PEMs) [20]. These thin films are generated by using the layer-by-layer (LBL) deposition technique which is described in the next section below.

1.3 LBL deposition

Layer-by-layer (LBL) deposition is a thin film fabrication technique. The films are produced by depositing consequent layers of oppositely charged materials with washing steps in between (Figure 1.2) [21]. LBL deposition as a multilayer build-up technique is mainly based on electrostatic interaction [22-24]. Other interactions such as hydrophobic attraction or hydrogen bonding may also be partially involved in this process[25]. The outstanding property of LBL is its high control over the thickness, which results from linear growth of the films with the number of bilayers. Based on the fact that each bilayer can be as thin as 1 nm, the LbL deposition method presents easy control over the film thickness with a resolution of 1 nm [18, 24, 26]. By denoting these two oppositely charged polyelectrolytes as “+” and “–“, and the washing step as ”W”, a simple representation can be made. To prepare a thin film by LbL with 4 bilayers one would deposit W+W- W+W- W+W- W+W-W, which will result to a thin film with 4 bilayers, specifically +-+-+-+-.

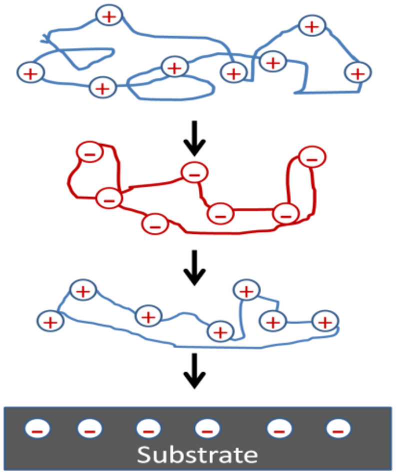

Figure 1.2 Schematic representation of LBL by charged polyelectrolytes.

LBL self-assembly is one of the most multipurpose and expedient techniques for surface modification. A broad variety of charged species, in addition to the polyelectrolytes, metal nanoparticles or bio-macromolecules can be built-in into the assembled layers, which permits the fabrication of functionalized and highly tuned surfaces with precise control over the charge density, composition, morphology and chemical activity [20, 21, 23, 24]. Using LBL as a synthetic tool, a broad spectrum of possibilities to produce polyelectrolyte films of targeted architectures and charge designs is accessible in addition to their simple preparation and tunable surface properties. Due to these convenient features, patterned polyelectrolyte films formed by LBL assembly are potential candidates for templates in colloidal patterning and also in a wide range of applications, such as biosensors, antireflection coatings, organic light-emitting devices, nonlinear optics, biomedical coatings, filtration membranes, and superhydrophobic surfaces [21, 24-28].

1.4 Protein resistant films

Understanding and controlling the interaction between artificial surfaces and proteins are crucial parameters in several medical and biochemical applications. There are two types of interactions take place between molecules; specific and unspecific. The specific-interaction of biomolecules, such as antibody-antigen, antibody-peptide are commonly used in biomedical diagnostics [2, 6, 29]. On the other hand, the unspecific interactions limit the accuracy of these methods as well as limit the determination of biocompatibility of artificial materials which are in contact with biological fluids such as incorporated catheters and prostheses[3, 4, 6, 29]. Therefore, it is important to prevent unspecific interaction of biomolecules with artificial surfaces. One of the most common and promising approach to generate protein resistant surfaces is functionalization of surfaces with ethylene glycol (EG) moieties[29, 30]. The protein resistance (repellent) properties of poly(ethylene glycol) (PEG) functionalized surfaces have been explained by having a resistance to dehydration and steric confinement of the swollen polymer[2, 29, 31, 32]. However, this model cannot explain the protein resistance of oligo(ethylene glycol) (OEG) terminated alkanethiolate self- SAMs on metal surfaces introduced by Whitesides et al. [29]. The OEG terminated alkenethiolate SAMs do not show neither significant swelling nor high conformational freedom. There are two possible models proposed which are i) on the importance of SAM/water interaction of the surface or ii) repulsive electrostatic forces. The detailed discussion on protein resistance and important parameters impacting the protein resistance can be found in the reference [30] and the references therein.

1.5 Micro- and nanopatterning of surfaces

In addition to homogeneously modified and gradient surfaces, chemical micro- and nanopatterned surface have become more important recently. The micro- and nanopatterned surfaces can be prepared by different methods such as microcontact printing, photochemically inititated insertion, electron beam lithography, block copolymer micelle lithography and colloidal lithography. All of these techniques will be discussed briefly. Since colloidal lithography was employed to generate nanopatterned surfaces for protein adsorption in this thesis, it will be extensively discussed below.

Microcontact printing (μCP) is a useful non-lithographic technique, which enables the generation of patterned surfaces in the micrometer and nanometer range [33]. Generally, microcontact printing technique is employed to the immobilization of alkanethiolate SAMs on noble metals such as gold, silver and palladium [34]. Moreover, this technique can also be applied to non-metallized surfaces, such as glass or Si/SiO_2, by immobilization of organosilane SAMs. Microcontact printing technique is generally utilized to generate patterns in the micrometer regime whereas the lower dimension limit is about 30nm [35, 36].

On non-metal surfaces micro-structures are alternatively generated by photochemically initiated insertion of terminally functionalized primary alkenes into the Si–H bond of newly etched silicon, through Si–C single bond formation [37, 38]. The dimensions of the pattern is determined by the photomask used. Non-functionalized substrate surface can be utilized to interact with a different type of alkene in a second illumination step.

Since conventional lithographic techniques are limited to generate patterns smaller than 100 nm in size due to diffraction, tremendous effort was put on development of alternative techniques such as electron beam lithography for generation of smaller than 100 nm sized patterns. In addition to physical modification of the surfaces by mask techniques or direct electron beam writing, chemically contrasted nanopatterns can also be generated [39, 40]. Currently, the smallest structures feasible are lines of approximately 20 nm in width. The chemically contrasted nanostructures generated by this technique might serve as a template in subsequent coupling reactions, therefore, being the basis for a variety of surface functionalization.

Generation of nanopatterned surfaces with macroscopic dimensions can be complex and highly time-consuming by sequential repetition of the mentioned techniques above. Nevertheless, availability and formation of macroscopic masks for nanostructures are rare. Nanostructure formation techniques based on self-assembly processes are promising alternatives such as block copolymer micelle nanolithography and colloidal nanolithography. In block copolymer micelle nanolithography, gold salt loaded micelles are deposited on a surface as densely-packed monolayers. By subsequent reduction of $HAuCl_4$ which is then followed by removal of the organic compounds, quasi-hexagonal structures of gold nanoparticles are formed on surfaces [41]. By changing the micelle loading and polymer chain length, nanoparticle patterns with a diameter of 2 to 50 nm with a center-to-center distance about 30 to 300 nm can be fabricated[42]. Consecutive growth of the gold nanoparticles is achievable by metal deposition from gold salt solutions. In colloidal lithography, monodisperse nanoparticles are deposited as a densely packed monolayer on a substrate. The nanoparticle monolayer acts as a mask in chemical derivatization of the surface by blocking nanometer size surface areas by particle/surface contact [43, 44]. After successful removal of the particles, the uncoated surface regimes may be further modified (Figure 1.3).

Colloidal lithography has several advantages over other techniques to generate nanopatterned surfaces such as size of the patterns can be tuned easily by changing the size of the colloidal masks[45]. Moreover, nanopatterned surfaces prepared by colloidal lithography can easily be analyzed by spectroscopic techniques due to easy large scale sample fabrication with reasonable expenditure of cost and time.

1.5.1 Colloidal Lithography

In last decades, precise patterning of colloids on surfaces have attracted extensive interest according to their potential applications in photonic crystals, data storage and electronic devices, growth of inorganic nanowires, actuators, and microelectronic circuits [23, 44, 46, 47]. To this end, it is very essential to develop efficient techniques for low-cost and high-throughput fabrication of 2D and 3D, large-area colloidal patterns with tunable structural parameters. To achieve these goals, strong and weak interactions which are in charge of directed self-assembly of colloids, like ionic, covalent, metallic, hydrogen and coordination bonding, and van der Waals, capillary, π-π, electrostatic and hydrophobic forces should be deliberately tuned according to intended purposes[48]. Among these interactions, electrostatic interactions are widely utilized in the phenomenon of directed self-assembly of colloids since they are long-range and rapid [44, 46, 47]. To employ electrostatic interactions as a main driving force for colloidal patterning, generally patterned polyelectrolytes and functional patterned surfaces have been used as templates.

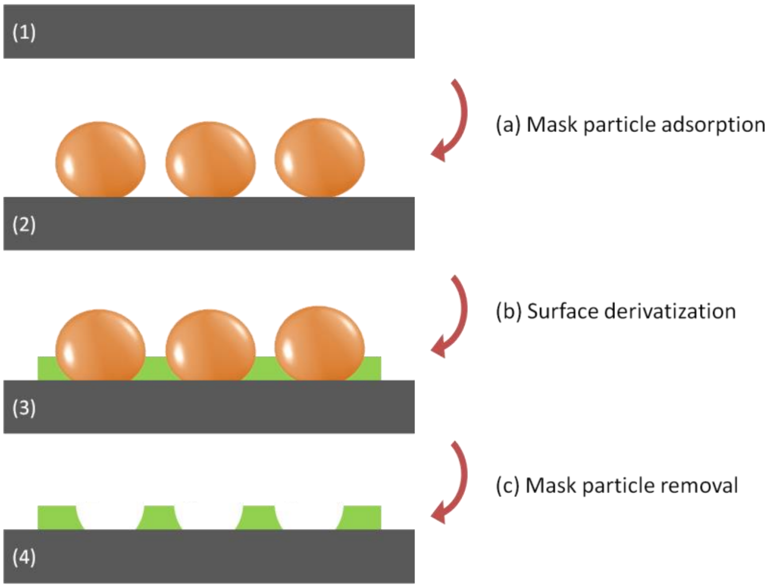

Figure 1.3 Schematic representation of surface nanopatterning by colloidal lithography. (a) Monolayers of monodisperse nanoparticles are deposited in a quasi-crystalline structure on a substrate and (b) the nanoparticle monolayer acts as a mask in chemical derivatization of the surface by blocking nanometer size surface areas by particle/surface contact. Last step (c) is removal of the particles. The uncoated surface regimes may be further modified.

There are also challenges in colloidal lithography such as (i) formation of the mask particle monolayer and (ii) the removal of mask nanoparticles below 100 nm. In this thesis, the first challenge was overcome by employing a so-called "self-assembly floating technique" and electrostatic deposition for different types of mask nanoparticles. To overcome the second challenge, a new technique called "nanoparticle blasting cleaning" was developed and employed. In the following section, self-assembly floating and electrostatic particle adsorption will be briefly discussed.

1.6 Mask particle deposition

1.6.1 Self-assembly floating method

An essential step in the fabrication of nanopatterned SAMs and PEMs is the deposition of mask nanoparticles on solid substrates such as Si (100) wafers, glass slides and flat metal films. There are several methods for mask nanoparticle deposition on solid surfaces employed in literature like self-assembly floating, spin-coating and electrostatic deposition [49-52]. The self-assembly floating has the advantage over the other methods that it generates more densely packed and almost defect free mask nanoparticle monolayers compared to spin coating [53, 54]. Moreover, self-assembly floating is employed to deposit mask nanoparticles larger than 100 nm more effectively without aggregation than electrostatic deposition.

The self-assembly floating method is commonly conducted in two main steps: As the first step, mask nanoparticles are transferred to a water/air interface by using a glass slide which is dipped into the water phase to disperse the mask nanoparticles [49, 53-56]. The quality and the density of the mask nanoparticle film on water can be adjusted and improved by means of adding amphoteric molecules such as anionic surfactants (e.g. sodium dodecyl sulfate) and nonionic surfactants (e.g. Triton X 400) [52, 56]. Afterwards, the mask nanoparticle monolayer is lifted off mechanically upon contact with the desired substrate.

The self-assembly floating method is extensively used for the preparation of patterned SAMs and PEMs in this thesis. For a detailed discussion on self-assembly floating and its theoretical background the reader is referred to Denkov et al [57].

In this thesis, the self-assembly floating method was employed to deposit amino-terminated silica nanoparticles with diameters in the regime of 70 - 500 nm.

1.6.2 Electrostatic deposition of Mask Nanoparticles

In electrostatic deposition technique nanoparticles, which are charge-stabilized to prevent aggregation, are deposited on oppositely charged substrates. This method is employed by simply immersing the charged substrate into the nanoparticle solution for a certain time. The deposited nanoparticle density on a substrate can be tuned by altering the surface charge density, nanoparticle concentration, pH of the medium, incubation time and particle size [58-62].

In this thesis, the electrostatic deposition technique was used to deposit monodisperse citrate capped (negatively charged) gold nanoparticle with sizes of 10 - 80nm on poly(allylamine hydrochloride) (PAH) and (3-aminopropyl) triethoxylsilane (APTES) coated silicon wafers.

1.7 Mask particle removal

During the preparation of nanopatterned surfaces by colloidal lithography, the deposited mask nanoparticles have to be removed from the substrate surface as discussed in section 1.4.1. The mask nanoparticles deposited by self-assembly floating can easily be removed from the substrate surface by conventional cleaning techniques such as ultrasonic cleaning [63, 64]. On the other hand, the mask particles with sizes smaller than 100 nm are harder to remove. Therefore, in this thesis a new removal technique, nanoparticle blasting cleaning, was employed to remove the mask nanoparticles having sizes of 10 - 100 nm.

A variety of cleaning methods have been developed for removal of sub-micrometer particles from surfaces such as ultrasonic, electrospray, cryogenic aerosol, supersonic nanoparticle beam and laser cleaning. Brief information on each cleaning technique will be given below. Further discussion and detailed information can be found in the references [63, 64] and the references therein.

In cryogenic aerosol cleaning, the deposited mask particles are bombarded by fine particles (bullet particles) of volatile material with high velocity. The removal of the mask nanoparticles takes place when the transferred energy from bullet particles is sufficient to overcome the adhesion energy between mask nanoparticle and substrate [63, 65]. This technique can remove particles larger than 50 nm.

Electrospray cleaning technique is based on generating small particles moving at a high speed as in cryogenic aerosol cleaning. However, in this technique bullet particles are generated by applying a voltage between a nozzle and emitter electrode where the kinetic energy of the bullet particle is altered [65, 66]. This technique can remove particles down to size of 50 nm.

Supersonic nanoparticle beam cleaning explores the possibility of using bullet particles which are smaller than 100 nm to remove nanoparticles down to 20 nm by collisions [67, 68]. The bullet particles are generated by a condensable gas which is pre-cooled close to the triple point of the condensed gas and then expanded through a supersonic Laval nozzle in a vacuum environment. The size and the velocity of the bullet particles are controlled by nozzle contour, stagnation pressure and temperature

In laser cleaning technique, a pulsed laser source is utilized for particle removal. Laser cleaning technique has three different variants according to their particle removal mechanisms: i) dry laser cleaning (DLC), ii) laser induced plasma cleaning (LIP) and iii) wet/steam laser cleaning (WLC) [63]. Laser cleaning techniques can remove nanoparticles having sizes down to 40 nm [63].

Even if the techniques mentioned above can remove nanoparticles down to 20 - 50 nm in size, there are drawbacks of these techniques. They are not time- and cost-efficient as well as sophisticated set-ups are required to employ these methods. On the other hand, ultrasonic cleaning technique has low cost and quick turn over to remove nanoparticles down to 100 nm. The ultrasonic cleaning technique is limited to remove down to 100 nm nanoparticles [69]. Therefore, a new nanoparticle removal technique, nanoparticle blasting cleaning, was developed. It is based on ultrasonic cleaning to remove mask nanoparticles with an ordinary ultrasonic cleaner, thus, providing time- and cost-efficiency.

Detailed information on the working principles of both ultrasound and nanoparticle blasting cleaning techniques are extensively discussed in section 4.1.1.

1.8 Protein Structure and Adsorption Mechanism

Proteins are biochemical compounds consisting of one or more polypeptides folded into globular or fibrous forms. A polypeptide is a single linear chain of amino acids bonded together by peptide (amide) bonds between the carboxyl and amino groups of adjacent amino acids[70]. The organization level of protein molecules are described by their structures. Protein structures can be classed into four different types: i) The primary structure refers to the linear sequence of amino acids in the polypeptide chains. This is the basic structure of proteins as they are assembled by ribosomes translating mRNA. [70-72] ii) The secondary structure refers to highly regular local sub-structures. These are generated by patterns of hydrogen bonds between the peptide groups in the main chain. The main types of secondary structure are the alpha helix and beta sheets, as suggested by Linus Pauling in 1951. iii) Tertiary structure refers to the three-dimensional structure of a single protein molecule. This is driven by non-specific hydrophobic interactions, and stabilized by tertiary interactions such as salt bridges, hydrogen bonds, tight packing of side chains, and disulfide bonds. iv) Quaternary structure is the highest level of protein organization and refers to the three-dimensional arrangement of macromolecular substructures of a protein. It is stabilized by the same interactions stabilizing the tertiary structure [70-72].

Proteins can undergo structural changes when they interact with or are adsorbed onto surfaces due to the fact that they are large amphiphatic molecules which makes them surface-active. As a consequence, they have a natural tendency to migrate and accumulate at interfaces[73]. The origins of these interactions which contribute to protein adsorption are found in intermolecular forces, such as Coulomb forces, Van der Waals forces, Lewis acid-base forces, and more entropically based effects such as hydrophobic interactions, conformational entropy and restricted mobilities [71, 73-76].

Among these interactions, surface wettability, i.e. being hydrophobic or hydrophilic, determines protein adsorption onto the surface after initial contact[74]. Figure 1.4 explains the adsorption mechanism of proteins on hydrophobic and hydrophilic surfaces. As hydrophobicity increases the amount of adsorbed protein increases and the protein spreads on the surface. Hydrophobicity gradient surfaces, as developed by Elwing et al., have been powerful tools in establishing this principle [77]. Using the wettability gradient method, it was shown that anti-fibrinogen and anti-high molecular weight kinonogen immunoglobulins bind to both hydrophilic and hydrophobic areas of the gradient but binding at the hydrophilic areas decreases with increasing incubation time. Moreover, anti-human serum albumin immunoglobulin binding increases with increasing incubation time at the hydrophobic end of the gradient [77].

Another important parameter in protein adsorption is its local charge which depends on pH and ionic strength, as well as the global charge of the protein and the adsorbing surface [70]. Using ellipsometry, Malmsten et al. have shown that the head group of phospholipids on surfaces has an effect on serum protein adsorption[78]. Serum protein adsorption was low on neutral or charge-shielded phospholipids such as phosphatidylcholine, phosphate idylethanolamine, sphingomyelin or phosphatidylinositol (similar to water-soluble polymers such as

PEO or poly(ethylene oxide)-block-poly(propylen oxide) (PEO-b-PPO)) while adsorption was extensive on charged phospholipids such as phosphatidic acid, diphosphatidylglycerol or phosphatidylserine (similar to silica or methylated silica) [78].

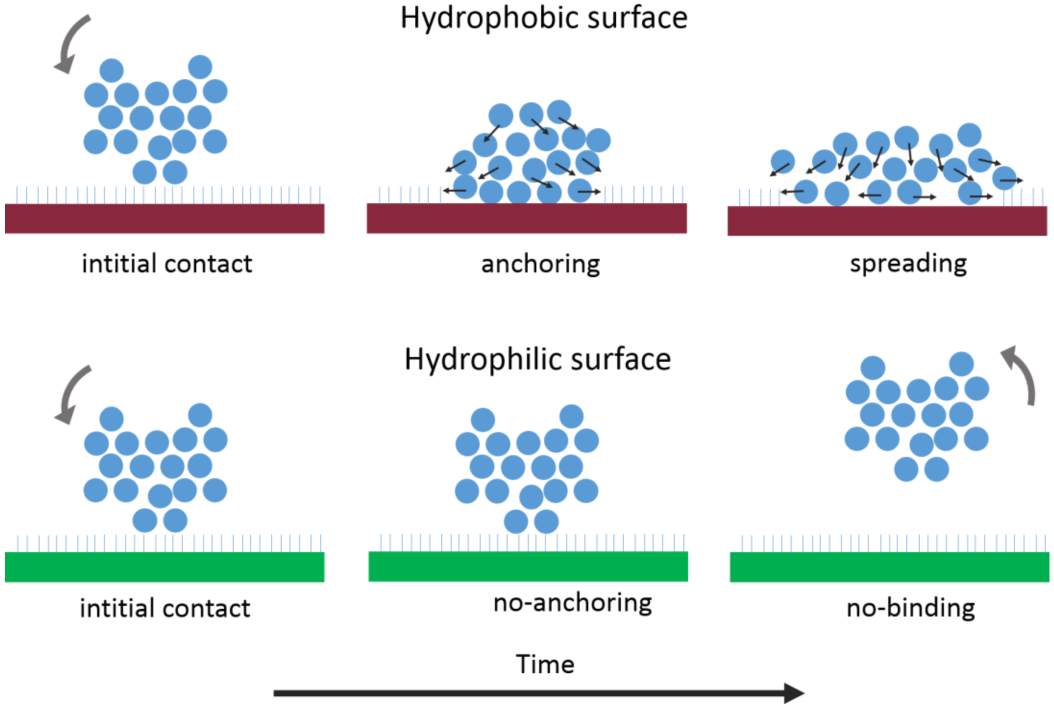

Figure 1.4: Schematic representation showing the adsorption mechanisms of proteins on hydrophobic and hydrophilic surfaces [73].

Some proteins experience structure changes during or after adsorption onto the surfaces. The area, which a protein resides on the surface, is called the footprint of the protein. The footprint of the protein generally increases with the residence time of the protein on the surface [72, 73, 78]. The increase in the footprint of the protein with time is called spreading (Figure 1.4). The spreading process is affected by the protein and surface properties. Generally, protein adsorption is only partially reversible because proteins undergo structural changes due adsorption onto the surface and they interact with the surface via many functional groups [73]. Changing pH or increasing ionic strength can desorb proteins [77].

After protein adsorption onto the surfaces, generally protein can undergo structural changes in a short time period (in milliseconds). These changes in protein structure can result in loss of protein structure which is called denaturation. Denaturation takes place with the loss of the secondary and tertiary protein structures present in the original state [71, 74, 76]. This happens under external stress such as strong acids and bases, inorganic salts, organic solvents, or heat [73]. However, only the interactions stabilizing secondary and tertiary structures are interrupted and the peptide bonds between amino acids remain intact. Therefore, the primary structure remains unaffected after denaturation [70, 73, 76]. Nevertheless, because of the fact that all levels of protein structure contribute to its function, denatured proteins cannot perform their tasks properly.

1.9 Enzyme immobilization

Enzymes are biomacromolecules that catalyze biochemical reactions in living systems. Enzymes can catalyze a number of very complex chemical conversions which cannot be accessed by ordinary organic chemistry methods [79]. Therefore, enzymes are very interesting for biotechnological applications [79, 80].
The reactions can be catalyzed by enzymes in three different states: i) as individual molecules in solution, ii) as aggregates with other entities and iii) attached to surfaces [81]. The last scenario is very important if enzymes are to be used for biotechnical purposes [79, 81].

The term immobilized enzyme was defined by Katchalski-Katzir et al. as “enzymes physically confined or localized in a certain defined region of place with retention of their catalytic activities and which can be used repeatedly and continuously” [81]. Immobilized enzymes are widely used in industrial processes such as production of sugars, amino acids and pharmaceuticals [79, 81]. Moreover, besides industrial process applications, immobilization techniques serve as a basis for the production of biotechnological products used in diagnostics, chromatography and biosensors [80-83].

The enzymes can be adsorbed onto a surface through interactions which can be classified into two broad categories: i) irreversible and ii) reversible methods. Enzymes immobilized by reversible methods can be desorbed from the surface under mild conditions. Reversible methods are shown in Figure 1.5. A detailed description and discussion can be found in the reference [81-83] and references therein. Irreversible immobilization refers to surface adsorbed enzyme which cannot be desorbed without destroying either the substrate or the biological structure of the enzyme. Irreversible immobilization methods are summarized in Figure 1.5. For a detailed discussion the author suggests [81] and the references therein.

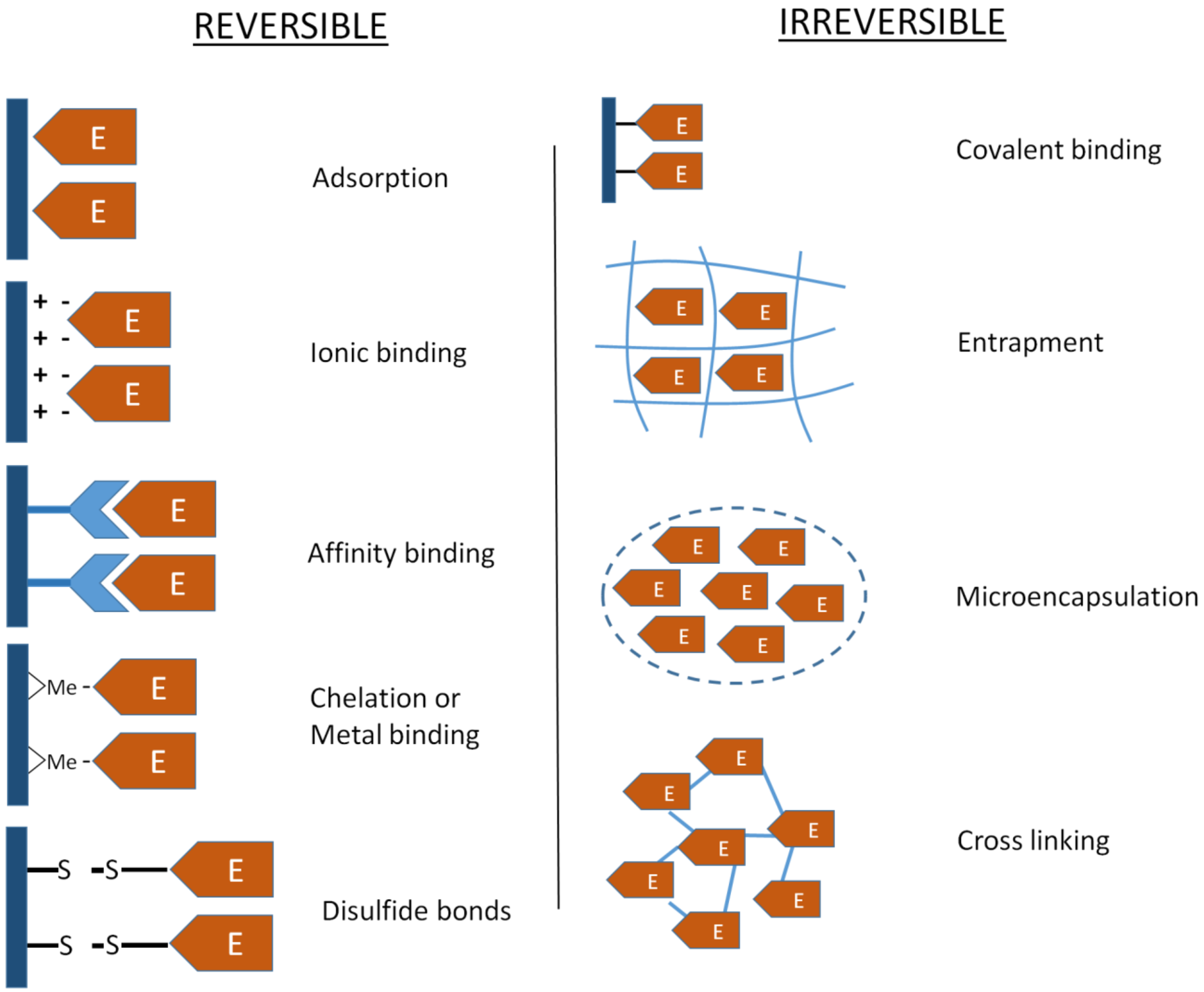

Figure 1.5: Reversible and irreversible enzyme immobilization methods.

Enzymes have the tendency to aggregate in solution phase and become less accessible for the substrate (steric restrictions). Therefore, immobilization of the enzymes onto surfaces might be a strategy to improve enzymes' catalytic activity

[79]. Moreover, in some cases the catalytic activity can be enhanced up to hundred fold (hyper-activity) since these steric restrictions are prevented by immobilization of enzymes to adsorption domains within a patterned inert matrix [79, 84]. The patterned inert matrix provides the necessary spacing which prevents aggregation of the enzymes and increases the accessibility of the active site of the enzymes.

1.10 Protein quantification

Enzyme-Linked Immunosorbent Assay (ELISA) is an analytic biochemistry assay for the detection of the presence of immunogenic analyte (a so-called antigen) in a sample. ELISA uses specific antibodies to bind to antigens which have been present in the sample and absorbed onto a surface [3, 85]. The antibodies are tagged with an enzyme that catalyzes a reaction that can be monitored by spectroscopic techniques such as UV-Vis spectroscopy. A spectrophotometric response (i.e. a change in color) indicates the presence of the substance of interest in the sample (Figure 10). The above scenario is called a direct ELISA.

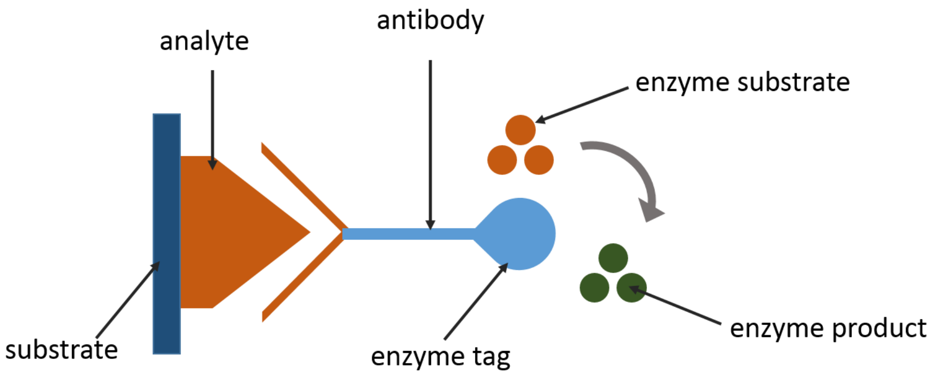

Figure 1.6: Schematic representation of a direct ELISA.

Enzyme-tagged antibodies are not readily available for a wide-range of analytes. Thus, the analyte is often first reacted with a specific primary antibody. Afterwards, an enzyme-tagged secondary antibody is specifically bound to the primary antibody. This type of ELISA is indirect, in contrast to direct ELISA (Figure 11) [3, 85, 86].

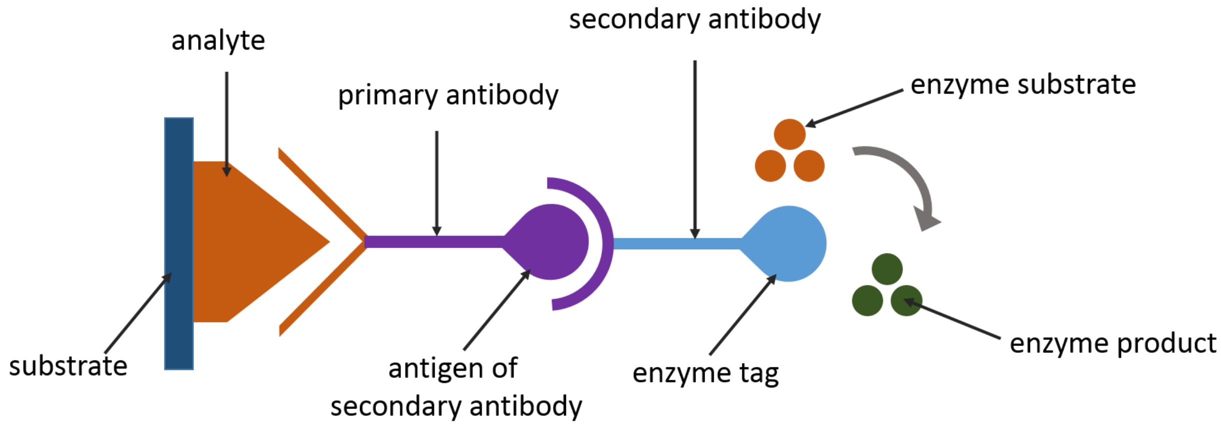

Figure 1.7: Schematic representation of an indirect ELISA.

ELISA is designed to detect the amount or presence of a protein contained in a liquid sample or adsorbed to a substrate. In the first case, the antigen of interest must first be bound to a surface such that a clear correlation exists between the concentration of the analyte in solution and protein surface density. This can, e.g. be achieved by immobilization of capture antibodies (not shown in Figs. 1.6 and 1.7) at the surface. The substrates are then immersed in a solution with the analyte, washed to remove weakly or non-specifically bound adsorbates, and then incubated with the respective antibodiy solutions. The rate at which the enzyme tag of the bound antibody converts its substrate into the product (monitored by spectroscopic techniques) is compared to rates at which known solutions of enzyme-tagged antibodies catalyze the same reaction in order to determine how much enzyme-tagged antibodies were bound to the adsorbate [85, 86].

In this study, the indirect ELISA method was employed. In order to determine the specific enzyme activity, i.e. the average activity per molecule, the determined absolute activity must be normalized to the amount of immobilized GOx. A detailed discussion on the indirect ELISA for the determination of surface-bound GOx can be found in section 3.9.

1.11 Model protein

In this study, a well-known enzyme, glucose oxidase (Aspergillus niger), whose catalytic activity is easily detectable and whose size corresponds to the dimensions of nanostructures prepared, served as a model protein.

Glucose oxidase (GOx) is a homodimer having 605 amino acids per monomer and has a total molecular mass of 131 kDa. The size of GOx is about 216.4 x 67.5 x 67.5 Å per monomer and it has a pI of 5.02. Its secondary structure contains 34% α-helix, 23% ß-sheet, and 43% random coil [87, 88]. It catalyzes the oxidation of β-D-Glucose to δ-gluconolacton, which spontaneously hydrolizes to gluconic acid and H_2O_2 which can be detected in a color reaction using horse radish peroxidase (HRPO) enzyme [87, 88]:

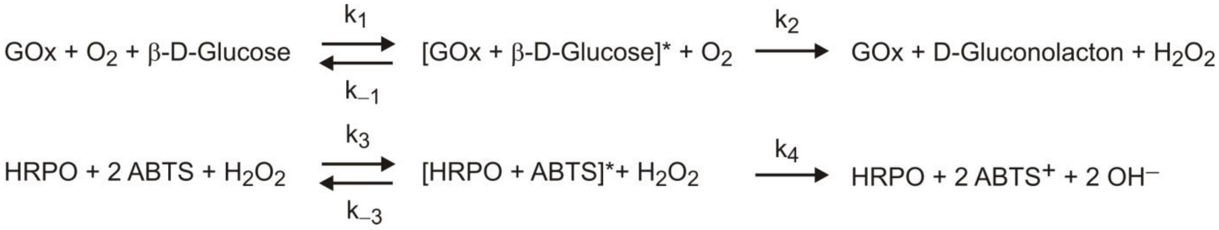

$$\text{GOx} + O_2 + \beta\text{-D-Glucose} \underset{k_{-1}}{\overset{k_1}{\rightleftharpoons}} [\text{GOx} + \beta\text{-D-Glucose}]^* + O_2 \xrightarrow{k_2} \text{GOx} + \text{D-Gluconolacton} + H_2O_2$$

$$\text{HRPO} + 2\,\text{ABTS} + H_2O_2 \underset{k_{-3}}{\overset{k_3}{\rightleftharpoons}} [\text{HRPO} + \text{ABTS}]^* + H_2O_2 \xrightarrow{k_4} \text{HRPO} + 2\,\text{ABTS}^+ + 2\,OH^-$$

1.12 Enzyme kinetic

The catalytic reaction kinetics of GOx can be described by Michaelis-Menten Theory. In this theory, the substrate, S, binds reversibly to an enzyme, E, to form an enzyme-substrate complex, ES*, with a rate constant k_1. ES* generates the product, P and regenerates the free enzyme E in an irreversible reaction with a rate constant k_2 as shown below [89]:

$$E + S \underset{k_{-1}}{\overset{k_1}{\rightleftharpoons}} ES^* \xrightarrow{k_2} E + P$$

k_{-1} is the rate constant for dissociation of ES* into E and S.

The concentration changes within time can be expressed by the following four differential equations:

$$\frac{d[S]}{dt} = -k_1[E][S] + k_{-1}[ES]^* \qquad \textit{(equation 1.1)}$$

$$\frac{d[E]}{dt} = -k_1[E][S] + k_{-1}[ES]^* + k_2[ES]^* \qquad \textit{(equation 1.2)}$$

$$\frac{d[ES]^*}{dt}=k_1[E][S]-k_{-1}[ES]^*-k_2[ES]^*$$

(equation 1.3)

$$\frac{d[P]}{dt}=k_2[ES]^*$$

(equation 1.4)

The enzyme substrate complex, ES*, is a transient product. Therefore, the formation rate can be assumed to be constant and the steady state approximation can be applied as in equation 1.5:

$$\frac{d[ES]^*}{dt}=0$$

(equation 1.5)

Assuming that the sum of the concentrations of free enzyme E and enzyme in the ES complex is equal to the initial concentration of the enzyme, E_0, equation 1.6 follows from Equation 1.4 for the product formation rate:

$$\frac{d[P]}{dt}=k_2[ES]^* \quad =\frac{k_2 k_1[E]_0[S]}{k_1[S]+k_2+k_{-1}}=\frac{k_2[E]_0[S]}{[S]+(k_{-1}\ +k_2)/k_1}$$

(equation 1.6)

By expressing the Michaelis-Menten constant K_M as,

$$K_M=\frac{k_{-1}+k_2}{k_1}$$

(equation 1.7)

the reaction rate, in Equation 1.6, can be expressed as

$$V=\frac{d[P]}{dt}=\frac{k_2[E]_0[S]}{[S]+K_M}$$

(equation 1.8)

For excess substrate concentration, $S \gg K_M$ can be assumed and the maximum reaction rate, V_{max}, is calculated as

$$V_{\max}=k_2[E]_0$$

(equation 1.9)

The maximum reaction rate (V_{max}) and Michaelis-Menten constant K_M can directly be determined from the substrate concentration vs. reaction rate graph as shown in Figure 1.8. K_M is the substrate concentration at half maximum of the reaction rate. K_M is one of the important parameters to determine the substrate affinity of an enzyme. As K_M becomes smaller, the affinity of the enzyme is higher [90, 91].

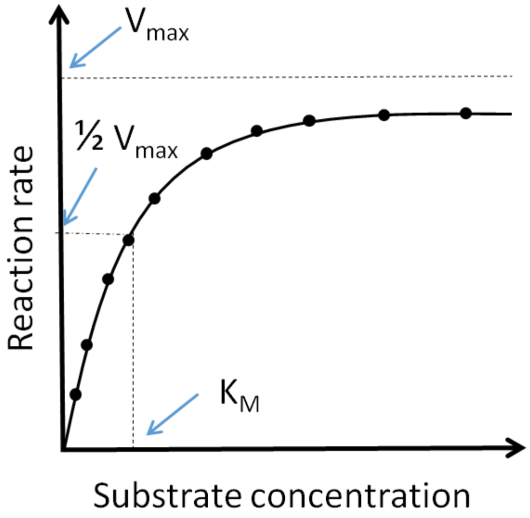

Figure1.8: Schematic plot of reaction rate vs. substrate concentration indicating the determination of K_M and V_{max}.

2 ANALIYTICAL METHODS

In this part of the thesis, the instrumental analysis techniques and the methods which were used to evaluate and analyze the prepared samples are introduced in terms of their basic principles. For this chapter the references [56, 92-99] were used.

2.1 UV-Vis Spectroscopy

Ultraviolet–visible (UV-Vis) spectroscopy is a reflectance or adsorption spectroscopy which uses the ultraviolet or visible spectral region. UV-Vis spectroscopy is a common technique for quantitative analysis for many different analytes, like biological macromolecules, transition metal ions, highly conjugated organic compounds etc. With this technique it is possible to work with gas or liquids as well as solid substances[96].

2.1.1 Principles

When radiation interacts with matter several phenomena consisting of reflection, scattering, absorbance, photochemical reaction, fluorescence and phosphorescence can happen. In UV-Vis spectroscopy generally it is desired to observe only adsorption while doing the measurement. The absorption of light by matter increases the energy content of the molecules, resulting in possible transitions between the different electronic levels. The UV-Vis region of the electromagnetic spectrum can be absorbed by molecules which have non-bonding electrons or pi-electrons, causing these electrons to be excited to higher anti-bonding molecular orbitals. Wavelength of the light adsorbed is directly related to the energy gap between the HOMO (highest occupied molecular orbital) and the LUMO (lowest unoccupied molecular orbital).

The difference between the incident radiation (I_0) and transmitted radiation (I) is giving the amount of light absorbed when light passes through a sample and it can expressed as either transmittance ($T = I/I_0$) or absorbance ($A = -\log T$) . It is also possible to measure the intensity of reflected light from a sample. The ratio between the intensity of reflected radiation from a sample (I) and the intensity of the incident radiation (I_0) is called reflectance ($R = I/I_0$).

The Beer-Lambert law indicates that the absorbance of a solution is changing proportionally to the path length and the concentration of the absorbing species (equation 3.1). Therefore, it is possible to quantitatively analyze the concentration of the absorbing species in the solution by keeping path length as fixed and using a calibration curve or reference molar extinction coefficients.

$$A = \log (I/I_0) = \varepsilon \cdot c \cdot L \qquad \textit{(equation 2.1)}$$

A	*Absorbance*
L	*Path length*
c	*Concentration*
ε	*Extinction coefficient*

2.1.2 Instrumentation

The main components of UV-Vis spectrometer are: a light source that produces a broad band of electromagnetic radiation; a dispersion device that separates particular wavelengths from the broad band radiation; one or more detectors to measure intensity of radiation; sample holder and optical components such as fibers, lenses or mirrors to transmit radiation through the instrument. A schematic diagram of a UV-Vis spectrometer that used in ELISA experiments is shown in Figure 2.1.

UV-Vis spectrometers can be classified into two groups according to light paths: single beam and double beam. In single beam instruments all of the light beam passes through the sample and is carried to the detector. In double beam instruments light is split into two beams. One beam passes through the sample and the other passes through the reference and then they reach two different detectors. As a light source a tungsten–halogen lamp (300-2500 nm) and a deuterium arc lamp (190-400 nm) can be used together to obtain a continuous beam of light at both UV and visible wavelengths. In general, prisms or holographic gratings are used as dispersion devices and they disperse different wavelengths of the light at different angles. The detector is typically a photodiode, a photodiode array, a photomultiplier tube or a charge-coupled device (CCD). Photomultiplier tubes and single photodiode detectors are used with scanning monochromators, while moving grating diffract each wavelength in sequence to detector. On the other hand, CCDs and photodiode array devices consist of many detectors placed in one or two dimensional arrays and they are used with a fixed monochromator, such as a grating. These detectors are simultaneously collecting light of different wavelengths on different pixels.

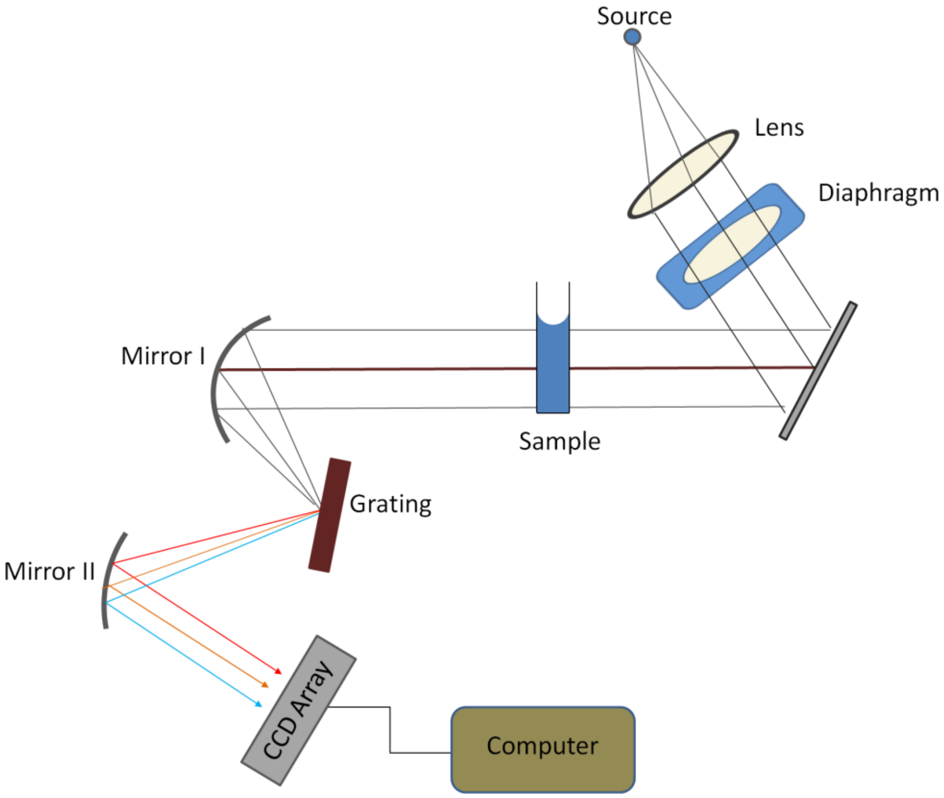

Figure 2.1: Schematic sketch of a UV-Vis spectrometer based on a grating spectrograph with an array detector. Using a lens and a diaphragm the radiation coming from tungsten and deuterium lamp is aligned parallel and the beam diameter is adjusted. Light transmitted through the sample is reflected from a collimating mirror (Mirror I) to a grating, which disperses the light beam into its component wavelengths. Dispersed light is then focused by a mirror onto a CCD array. The computer processes the output data coming from the array detector.

2.2 Scanning Electron Microscopy (SEM)

A scanning electron microscope provides an image of the surface of a sample with high magnification. The resolution of the SEM may be down to a few nanometers. Sample images with magnifications from 10 to 300,000 can be collected. SEM is not limited to topographical information; it is also capable to give information about the composition of the near surface region of the material[92, 99].

2.2.1 Principles of operation

An electron beam is focused on the surface and scans it. While electrons are penetrating the sample, a couple of interactions occur at the surface of sample which cause emission of electrons or photons from the surface. A sensible amount of electrons emitted can be collected by detectors, converted to a voltage and amplified. The amplitude of the voltage determined by the amount of detected electrons. While the electron beam scans the sample surface, the voltage is synchronously applied to grid of cathode ray tube (CRT) and the intensity of light spot is regulated. Every point that the beam hits on the surface is plotted directly onto a corresponding point on the screen. The applied voltage generates or changes the intensity of the light spot on the CRT screen so that an image is obtained.

In principle three types of images can be obtained from SEM. They are called: secondary electron (SE) images, backscattered electron (BSE) images and elemental X-ray maps. It is easy to separate backscattered electrons and secondary electrons due to their different energies. Two different mechanisms generate these two types of electrons. The interaction of high energy primary electrons with an atom causes either inelastic scattering with electrons or elastic scattering with the atomic nucleus. Energy transfer occurs during the inelastic collision with an electron. If the energy transfer is not so high, the emitted electron most likely does not leave the surface because it has not gained sufficient energy. However if the transferred energy overcomes the work function of the material, the emitted electron can leave the sample surface. The energy of the emitted electrons is a conventional indicator to categorize them as secondary electron if it is less than 50 eV. The majority of the secondary electrons is generated within the first couple of nanometers of the sample surface. Secondary electrons which are produced in deeper parts of the sample undergo further inelastic collisions which decrease their energy and confine them inside the sample.

The primary electrons which are scattered with no loss of energy from the nucleus of an atom after elastic collisions are called back scattered electrons (BSE). These elastic collisions may happen after a couple of inelastic collisions which are lowering the energy of the primary electrons. On the other hand, back scattered electrons may have energies similar to that of the primary electrons. These electrons leave the sample surface with an energy of more than 50 eV including Auger electrons. Backscattering is enhanced if the atomic number of the material increases.

The primary beam current I_0 can be defined by the Kirchhoff current law *(equation 2.2)*. The sum of the BSE current I_{BSE}, the SE current I_{SE} and the sample current i_{SC}, transmitted through the sample to ground, gives I_0:

$$I_0 = I_{BSE} + I_{SE} + i_{SC} \qquad \textit{(equation 2.2)}$$

In the SEM there is another interaction between the electrons and the material which is very significant and occurs when a primary electron collides with a core electron and ejects it from an atom. The excited atom emits a characteristic X-ray photon or Auger electron. These X-ray signals can be classified with an energy dispersive X-ray detector or by a wavelength spectrometer. These energy or wavelength distributions are unique for each element so that the SEM generates elemental images which represent the fractional distribution of elements in the field of scanned surface. The primary electrons can travel inside the sample substantial distances before they lose so much of their energy by collisions that they can no longer excite atoms to emit X-ray photons.

2.2.2 Instrumentation

A SEM consists mainly of a vacuum chamber, an electron gun, magnetic focusing lenses, apertures, a stigmator, deflection coils, the stage region and the electronic unit including control panel, scanning modules and power supplies. The schematic representation of SEM instrumentation can be seen in Figure 2.2.

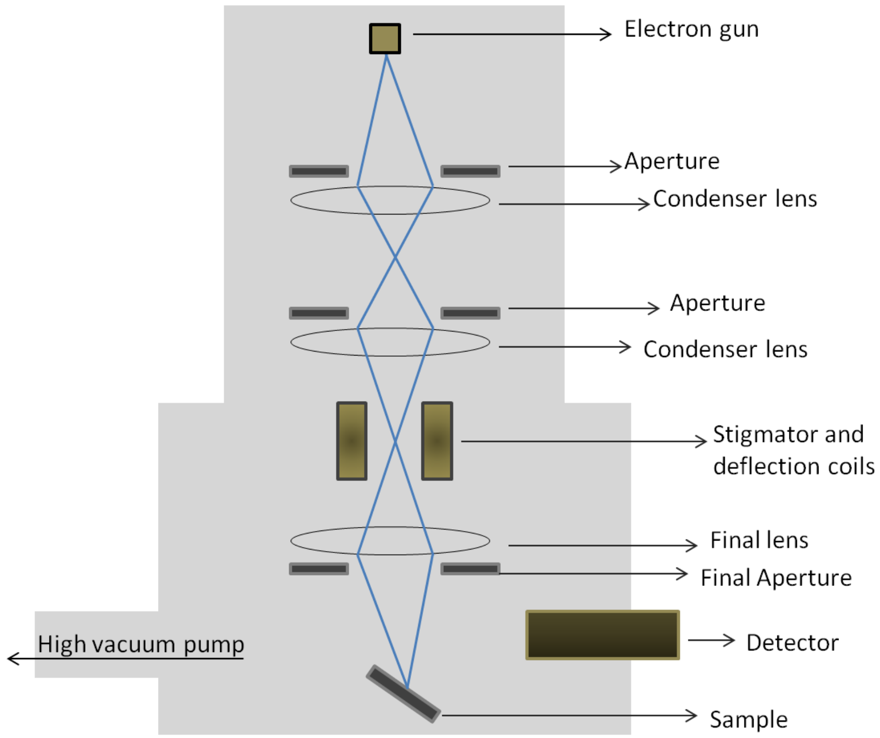

Figure 2.2: Schematic of the SEM column and sample chamber.

The vacuum is crucial for the system because the electron gun can work properly only at low pressure. Generally in SEM systems, diffusion pumps are used and they usually supported by rotary pumps. Mainly three types of electron sources are used in SEMs. They are: thermionic tungsten, LaB_6 and hot and cold field electron beam filaments. Tungsten filaments are heated up by applying voltage to them. The temperature of the filament increases to about 3000 °C and electrons start to be emitted via thermionic emission. These filaments have short life times of 50-150 hours because of evaporation, but they are relatively cheap. The LaB_6 filaments are produced by placing LaB_6 crystal on tungsten or rhenium. As a result of the lower work function than tungsten, LaB_6 can be operated at lower temperatures and it yields a higher amount of electron emission. On the other hand, LaB_6 filaments require higher vacuum than tungsten filaments to attain good stability and long life-time. In new SEM systems, field emission electron sources are favored according to their high resolution and low voltage applications. These sources have very sharp tips and a strong electric field generated at the tip allows electrons to leave the source even at low temperatures.

The disadvantages are that they are more difficult to work with and that they need very high vacuum and regular cleaning and sharpening.

2.2.3 Sample requirements

SEM requires very simple sample preparation if the sample is vacuum compatible. If the sample is conductive, the main limitation is whether the specimen will fit onto the stage or into the sample chamber. In the case of an insulator sample, there are two main approaches that can be used. The simplest approach is coating the sample surface with a very thin conducting film of gold, titanium, carbon or some other metal. Additional care should be taken to keep away from artifacts and distortions caused by agglomeration or non-uniform coatings. If an X-ray analysis is to be made with an insulator sample which is metal coated, additional attention must be paid to eliminate or correct for any X-ray peaks coming from the deposited layer. Insulating samples can also be analyzed by SEM without conductive film coating by using low primary beam voltages (> 2keV). This approach is reasonable when one is willing to compromise image resolution to some extent.

2.3 Atomic force microscopy

Atomic force microscopy (AFM) or scanning force microscopy (SFM) is a high-resolution scanning probe microscopy. It is a real-space imaging technique that can generate 3-D topographical images of the sample surface on areas larger than 250 x 250 μm with a lateral resolution of less than a nanometer and vertical resolution of less than an Angstrom. AFM is more powerful than any other high-resolution profilometer because of its excellent resolution and the fact that it is also free from many of the artifacts that the others suffer from. AFM is only sensitive to topography and it analyzes the surface independently from the optical properties of the surface. Insulator, semiconductor, conductor, transparent and opaque materials can be analyzed under air, liquid or in vacuum. AFMs are much simpler to operate compared to electron microscopes. Because the AFM can be operated under ambient conditions, set-up time is around a couple of minutes and AFM needs very little or no sample preparation[95, 97, 99].

2.3.1 Principles of operation and instrumentation

Atomic force microscopy uses flexible cantilevers with a sharp tip. The cantilever is mounted on a millimeter sized holder chip and has dimensions of about a few micrometers. The radius of the tip is around a couple of nanometers. When the tip comes close to the specimen surface, typically fractions of a nanometer, van der Waals forces between tip and specimen deflect the cantilever. The extent of deflection is related to the distance between tip and specimen and is generally determined by a laser spot reflected from the top surface of the cantilever onto an position-sensitive photodetector (PSPD). For scanning the tip in the x, y and z directions across the sample a tripod of piezoelectric transducers is used and a feedback loop operates on the scanner to maintain a required position of the tip with respect to the sample. A schematic sketch of an atomic force microscope is shown in Figure 2.3

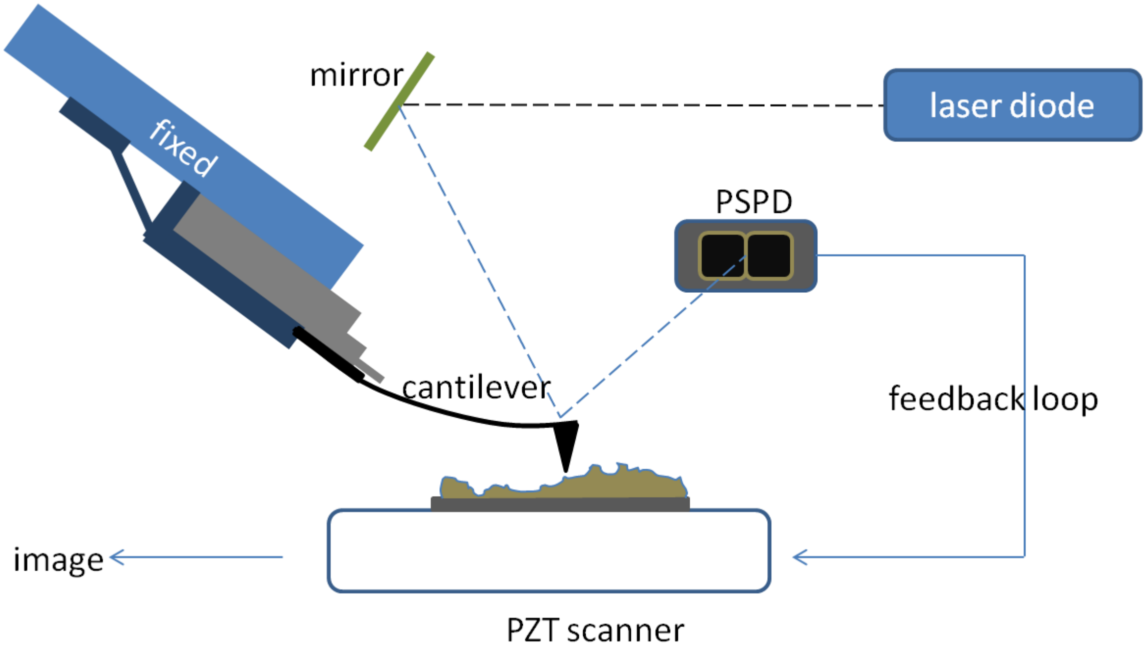

Figure 2.3: Schematic representation of AFM operation.

AFM can be used in numerous modes, according to the application. In common, possible imaging modes are divided into static (contact) modes and dynamic modes (non-contact or "tapping") where the cantilever is vibrated. In contact mode, the tip is swept across the surface of the sample and thereby measures the topography. The image is produced by either using the deflection of the cantilever directly or by the feedback signal necessary to maintain the cantilever at a constant distance. In the first case, during contact with the sample, the probe predominately experiences repulsive ionic or Pauli-repulsion forces. In non-contact mode, the sample surface has no contact with the tip of the cantilever. The cantilever is alternatively oscillated at its resonant frequency or slightly above. The typical amplitude of oscillation ranges between a few nanometers (less than 10 nm) and a few picometers. The attractive van der Waals forces, which are dominant from 1 nm to 10 nm above the surface, decrease the resonance frequency of the cantilever. By combining the decrease in resonant frequency with a feedback loop system a constant oscillation frequency is maintained by adjusting the tip-to-sample distance. The topographical image of the surface is generated measuring the tip-to-sample distance for each (x,y) data point. The attractive van-der-Waals forces and the Pauli repulsion, according to overlapping electron orbitals, can be described by the Lennard-Jones potential shown in Figure 2.4.

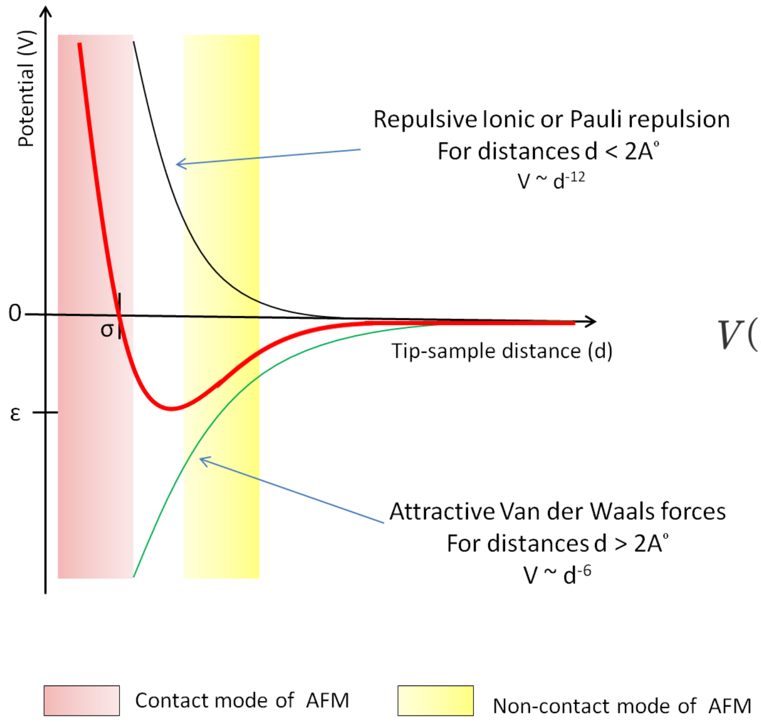

$$V(d)=4\varepsilon\left[\left(\frac{\sigma}{d}\right)^{12}-\left(\frac{\sigma}{d}\right)^{6}\right]$$

Figure 2.4: Lennard-Jones potential. In contact mode there is repulsive forces in between AFM tip and sample surface, in non-contact mode there are attractive forces in between AFM tip and sample surface.

In tapping mode the cantilever is oscillating up and down close to its resonance frequency driven by a piezoelectric element placed in the AFM tip holder like in non-contact mode. In contrast to non-contact mode the amplitude of the oscillation is more than 10 nm, most commonly in the range of 100 nm to 200 nm. The amplitude of the oscillation decrease when the tip comes closer to the sample as a result of interaction forces influencing the cantilever.

In AFM technique it is possible to encounter several image artifacts reasoned by unsuitable tip, a poor operating environment or as well the sample itself (represented in Figure 2.5). These image artifacts are inescapable, however, their presence and effect on the results can be decreased by several methods.

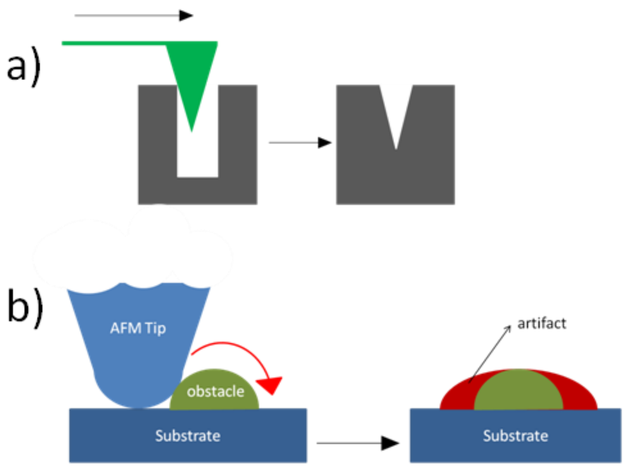

Figure 2.5: Ideally a probe (tip) with a high aspect ratio will give the best resolution. a) AFM artifact caused by steep sample topography. b) AFM artifact arising from a tip with a high radius of curvature with respect to the feature that is to be visualized. This does not often influence the height of a feature but the lateral resolution.

2.4 X-ray photoelectron spectroscopy (XPS)

X-ray photoelectron spectroscopy, also named electron spectroscopy for chemical analysis (ESCA), is one of the most powerful surface analysis technique due to its excellent chemical state determination capabilities, its applicability to a broad range of materials and its non-destructive nature. The common applications of XPS can be listed as: elemental identification and quantification, depth profiling and chemical state identification. XPS`s weak points are its lack of ability to detect hydrogen and its poor spatial resolution (70 µm) [99].

2.4.1 Principles

XPS analysis based on the detection of the kinetic energy of an ejected free electron when a highly energetic photon of sufficiently short wavelength ionizes an atom. In neutral atoms the number of electrons is equal to the number of protons in the nucleus. Electrons are located in orbitals where they are bound to nucleus by electrostatic interaction. The energy level of a certain core orbital (or eigenvalue ε) is discrete and it is characteristic for each element due to different electrostatic interaction according to different number of protons in nuclei. The binding energy (E_b) of an electron is equal to the ε value and it can be defined experimentally by measuring the kinetic energy of the photoelectron. The kinetic energy of the ejected electron (E_k) is subject to the energy of the X-ray, hv, and it is given by Einstein´s photoelectric law:

E_k = hv –E_b-W_f *(equation 2.3)*

where W_f is the work function of the material (which is the minimum energy to lift one electron from an atom in a solid to vacuum level as shown in Figure 2.6).

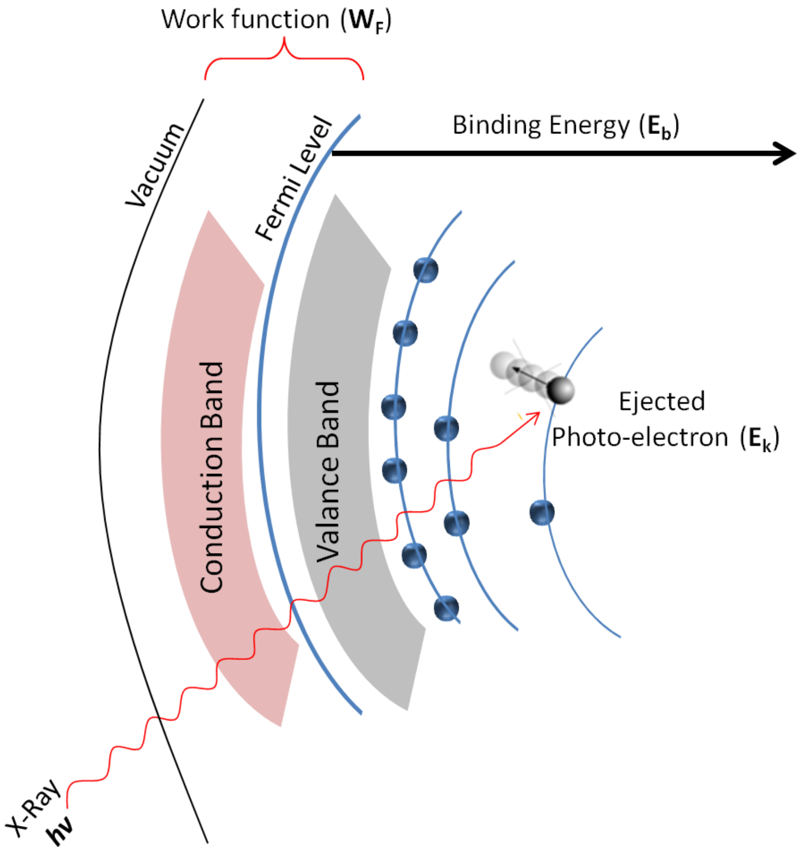

Figure 2.6: Schematic diagram of the energy levels.

Due to the possible different chemical environments of atoms, they may show chemical shifts in XPS analysis. This is, because the binding energy is directly related by the oxidation state, ligand electronegativity or the element that the atom makes bonds with. Therefore, it is possible to provide some significant structural information in addition to elemental analysis by considering the chemical shifts. In Figure 2.7 the carbon 1s spectrum of the ethyl trifluoroacetat molecule is given. In the spectrum there are four peaks and they refer to four different carbon atoms having different chemical environment.

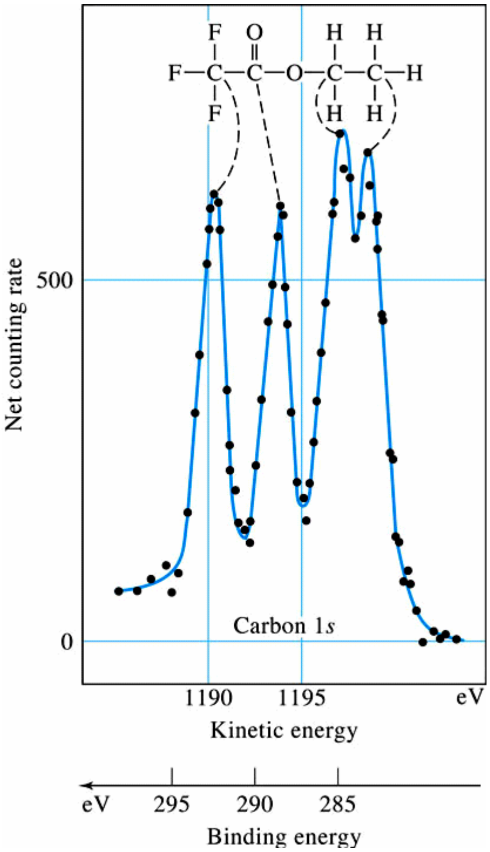

Figure 2.7: Carbon 1s signal in the XPS spectrum shoving chemical shifts for carbon atoms having different chemical environment.

XPS is only able to provide information about a couple of outer atomic layers of the surface. Even though X-rays can penetrate into the sample more than micrometers, the ejected photoelectrons can travel only short distances through the solid sample due to inelastic collisions with atoms. Therefore only the electrons generated within a surface layer of approximately 10 nm depth are capable to leave the solid surface. By considering the X-ray source and surface sensitivity of the sample more accurate numbers can be provided. The depth range from which electrons are ejected for a particular sample defines the surface sensitivity. The inelastic free mean path (λ), which is the average distance that a particle of a given energy travels through the sample in between inelastic collisions, can be used to characterize the surface sensitivity of a sample. The following equation is stating that there is exponential relation between I_0, the flux of electrons generated at a depth d from the surface, and I_d, the flux of electrons escaping from the material. Here, Θ is the angle of electron emission.

$I_d = I_0\ ^{-d/\lambda \sin\Theta}$ *(equation 2.4)*

2.4.2 Instrumentation

XPS systems are very sophisticated and expensive systems. They mainly consist of an ultra-high vacuum (UHV) stainless steel chamber with UHV pumps, a source of X-rays, an electron collection lens, an electron energy analyzer, Mu-metal magnetic field shielding, an electron detector system, a moderate vacuum sample transfer chamber, a sample stage and a set of manipulators. A schematic sketch can be seen in Figure 2.8.

Generally a Mg- or Al-coated anode is used as the X-ray source which is struck by electrons accelerated by high voltage (10-15 kV). The electrons produce Al-Kα or Mg-Kα radiation lines at energies of 1486.6 eV and 1256.6 eV. The spot size of the X-ray beam can be reduced down to 100 μm diameter by focusing the electron beam onto the anode. Then the X-rays aligned to pass through from a X-ray monochromator. After the focused X-ray beam ionizes the sample, the emitted electrons are slowed down by electron lenses to improve energy resolution before they enter the hemispherical analyzer, which consists of two concentric hemispheres with a voltage applied between them. By altering the voltages on the lenses and the analyzer, the trajectories of electrons ejected from the sample at different energies can be focused at the analyzer exit slit. A channeltron type electron multiplier amplifies individual electrons by a factor of 10^5 to 10^6. Each pulse is counted with a conventional pulse counter and sent to a computer, where electron pulses counted are plotted versus analyzer-lens voltage to provide the photoelectron spectrum.

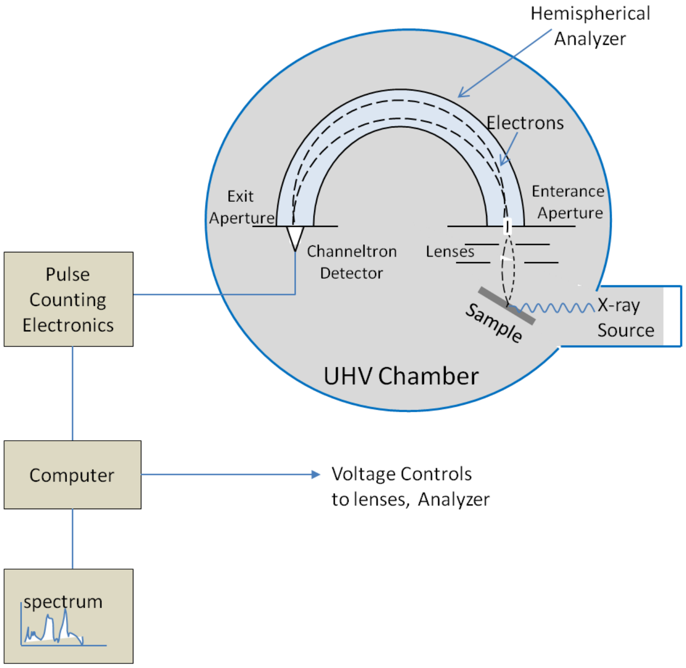

Figure 2.8: A schematic sketch of a XPS spectrometer.

2.5 Ellipsometry

Ellipsometry is an optical technique for investigating the dielectric properties of thin films such as complex refractive index or dielectric function. It is used to analyze composition, roughness, and thickness. Ellipsometry is a non-destructive and contactless technique which has found applications in a wide range of fields from microelectronics to biology and from basic research to industrial applications[94].

2.5.1 Principles and instrumentation

Ellipsometry investigates the change of light polarization upon reflection from a surface or transmission through a sample and compares it to a model. The sample's properties (thickness, complex refractive index or dielectric function tensor) are determined by measuring the change in the polarization.

A schematic sketch of ellipsometer is shown in Figure 2.9. The electromagnetic radiation is emitted by a light source and linearly polarized afterwards. Then the beam passes through an optional compensator (retarder, quarter wave plate) and interacts with the sample. After being reflected from the sample the radiation passes through a compensator and a second polarizer (analyzer), and reaches the detector.

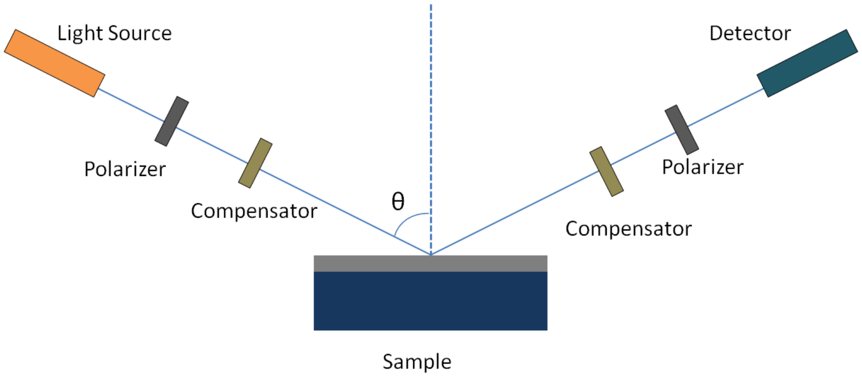

Figure 2.9: Schematic sketch of an ellipsometry

When ellipsometric measurements are carried out on a three component optical system, composed of ambient, film and substrate, and the refractive indices for the three media are known, it is feasible to determine the thickness of the film. Such a three component optical system is represented in Figure 2.10.

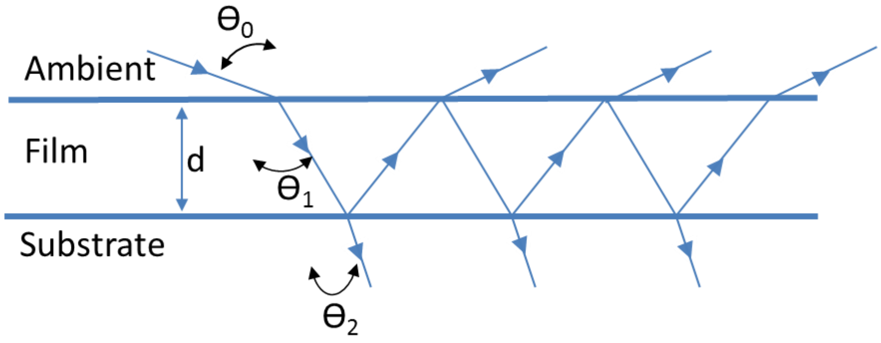

Figure 2.10: Illustration of an optical system composed of ambient, film and substrate.

The complex reflection ratio P for the system is given in equation 2.5, where Ψ is the amplitude component, Δ is the phase difference, and P_σ and P_Π are the reflection coefficients (*equation 2.5a, 2.5b*).

$$P=\frac{P_\pi}{P_\sigma}=\tan(\psi)e^{j\Delta}$$

(equation 2.5)

$$P_{\pi} = \frac{\rho_{01,\pi} + \rho_{12,\pi} e^{-j2\beta}}{1 + \rho_{01,\pi}\rho_{12,\pi} e^{-j2\beta}}$$

(equation 2.5a)

$$P_{\sigma} = \frac{\rho_{01,\sigma} + \rho_{12,\sigma} e^{-j2\beta}}{1 + \rho_{01,\sigma}\rho_{12,\sigma} e^{-j2\beta}}$$

(equation 2.5b)

The phase change parameter, ß, in equations 2.5a and 2.5b is defined in equation 2.6 where $\tilde{n}_1$ is the complex refractive index of film, $\tilde{n}_2$ is the complex refractive index of the ambient, and θ_0 is the angle of incidence:

$$\text{ß} = 2\pi \frac{d}{\lambda} \sqrt{\tilde{n}_1^2 - \tilde{n}_0^2 \sin^2(\theta_0)}$$

(equation 2.6)

When the equations 2.5a, 2.5b and 2.6 are put in equation 2.5 and the resulting polynomial equation is solved for thickness, d, the following equation is obtained, where λ is wavelength of the incident light.

$$d = \frac{j \ln(X) \lambda}{4\pi \tilde{n}_1 \cos(\theta_1)}$$

(equation 2.7)

The ln(X) in equation 2.7 is defined as follows:

$$\ln(X) = -j4\pi \frac{d}{\lambda} \tilde{n}_1 \cos(\theta_1)$$

(equation 2.8)

3 EXPERIMENTAL

3.1 Materials

Triton X-100, sodiumdodecyl sulphate (SDS, 99+%), hydrogen tetrachloroaurate(III) trihydrate (99.9+%), trisodium citrate dihydrate (99+%), sodium chloride (≥99 %), poly(allylamine hydrochloride) (PAH, MW ≈ 15,000 g/mol), sulfonated polystyrene (SPS, MW ≈ 70,000) hydroxylamine hydrochloride (99.9+%), phosphate-buffered saline (PBS) tablets, O-(2-mercaptoethyl)-O′-(2 carboxyethy)heptaethylene glycol (EG7-SH), (95%), potassium chloride (≥99 %), hydrochloric acid (37%), methanol (99%), poly(ethylene glycol) methacrylate (Mn≈360), copper(I) bromide (95%), 2,2'-bipyridyl (99%), (3-aminopropyl)triethoxylsilane (98%), ethanol abs. (99.9%), 2,2'-azinodi(3-ethylbenzothiazoline)-6-sulfonic acid (99.9%), dichlormethane (99.8%), glacial acetic acid (96%) and *N*-(3-dimethylaminopropyl)-*N'*-ethylcarbodiimide hydrochloride (98%)**,** N-hydroxysuccinimide (NHS), (98%), monobasic potassium phosphate (99%), N-(3-dimethylaminopropyl)-N′-ethylcarbodiimid hydrochloride (EDC), (99%), were purchased from Sigma-Aldrich GmbH (Germany). Dimethylformamide (99%), sodium hydroxide (99%), hydrogen peroxide (30%) were purchased from Baker (Netherlands) and 2-[methoxy(polyethylenoxy)propyl]-trichlorosilane (90%) from ABCR, (Germany).

One-side optically polished silicon (100) and double-side optically polished silicon (111) wafers were purchased from Silicon Materials (Landsberg am Lech, Germany), Deionized water was purified with a Milli-Q plus system by Millipore (Eschborn, Germany). All chemicals were used without further purification. A variety of nanoparticles and proteins used in experiments are listed below in table 3.1 and 3.2.

Nanoparticle Type	Size	Concentration	Producer
Silica	100 nm Polydispersity index: < 0.2	25 mg/ml	Micromod Partikeltechnologie GmbH, Rostock, Germany
Silica	200 nm Polydispersity index: < 0.2	50 mg/ml	Micromod Partikeltechnologie GmbH, Rostock, Germany
Silica	500 nm Polydispersity index: < 0.2	50 mg/ml	Micromod Partikeltechnologie GmbH, Rostock, Germany
Silica	50 nm	5.69%	Polysciences Inc., Warrington, USA
Silica	10 nm	5.60%	Polysciences Inc. Warrington, USA
Polystyrene	51 nm	2.60%	Polysciences Inc. Warrington, USA
Polystyrene	81 nm	2.61%	Polysciences Inc. Warrington, USA
Polystyrene	194 nm	2.65%	Polysciences Inc. Warrington, USA

Table 3.1: List of nanoparticles used as colloidal masks or as bullet particles.

Protein type	Concentration/Purity	Producer
Glucose oxidase, Typ X-S	Lyophilisate 65-85% protein (100-250, kU/g)	Sigma-Aldrich, Steinheim, Germany
Bovine serum albumin	>98%	Sigma-Aldrich, Steinheim, Germany
Rabbit anti-*Aspergillus niger* glucose oxidase IgG?	Lyophilisate (0.8 mg/ml reconstructed)	Thermo Scientific, Rockford, UK
Goat horeseradisch peroxidase-tagged anti-rabbit IgG?	Lyophilisate (0.8 mg/ml reconstructed)	Jackson Immuno Research, West Grove, USA
Horseradisch peroxidase, Type II	Lyophilisate, salt-free	Roche, Mannheim, Germany

Table 3.2: **List of proteins used in ELISA and protein adsorption experiments.**

3.1.1 Stock solution preparation

Tri-sodiumcitrate-dihydrate solution (TSC):

2 grams of tri-sodiumcitate-dihydrate ($Na_3C_6H_5O_7$-H_2O) is dissolved in 200 ml of Milli-Q water to obtain a final concentration of 1% (w/v) and stored in a fridge. It was warmed up to room temperature (RT) before use.

Phosphate buffered saline solution (PBS)

PBS solution was prepared by dissolving one PBS tablet in 200 ml Milli-Q water (pH 7.4) and stored in fridge. It was warmed up to room temperature before use.

Acetate buffered saline (AcBS): By using a magnetic stirrer, 0.584 g NaCl (10 mmol) was dissolved in 30 mL water. Then 0.574 mL glacial acetic acid was added to the solution and the total volume of 100 ml is achieved by adding Milli-Q water. By adding 1 M sodium hydroxide and using a pH-meter, pH was adjusted to 5.5. The solution was stored in fridge and it was warmed up to room temperature before use.

2,2'-Azinodi(3-ethylbenzothiazoline)-6-sulfonic acid (ABTS) solution:

35.8 mg 2,2'-azinodi(3-ethylbenzothiazoline)-6-sulfonic acid were dissolved in 30 mL AcBS solution. The stock solution was light protected and stored in a fridge. It was warmed up to room temperature before use.

Bovine serum albumin solution (BSA):

500 mg of Bovine serum albumin was dissolved in 50 ml of PBS solution to obtain a final concentration of 1% (w/v) and stored in fridge. It was warmed up to room temperature before use.

Glucose oxidase solution (GOx):

20 mg of glucose oxidase was dissolved in 20 ml of AcBS solution to obtain a final concentration of 1% (w/v) and stored in fridge. It was warmed up to room temperature before use.

Hydrogen tetrachloroaurate(III) trihydrate solution:

20 mg of hydrogen tetrachloroaurate(III) trihydrate was dissolved in 10mL Milli-Q water to obtain a final concentration of 2% (w/v). The stock solution was light

protected and stored in a fridge. It was warmed up to room temperature before use.

3.2 Substrate preparation

Prior to sample preparation silicon wafers were cut into pieces of about 1 x 1 cm^2, rinsed with water, blown dry with nitrogen, and exposed to ozone for 1 h in order to remove any adsorbed organic compounds. Substrates were always handled with polypropylene tweezers to avoid scratching of the surface. Ozone was generated by irradiation of air with a mercury vapor lamp (NIQ 40/18, Heraeus, Hanau, Germany) at λ = 254 nm and 10 W, and the samples were positioned at approximately 4 cm distance from the lamp.

3.3 Synthesis

3.3.1 Synthesis of gold nanoparticles:

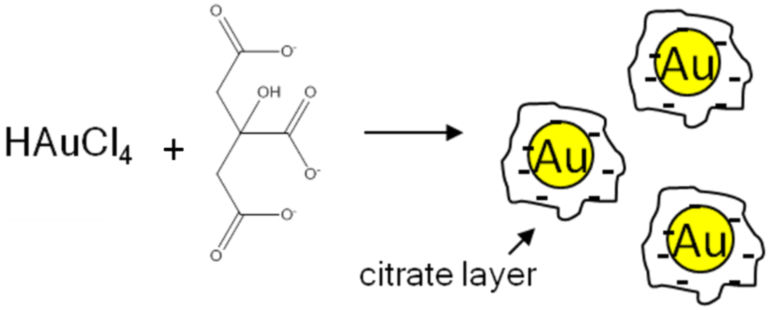

Figure 3.1: Showing formation of citrate anion capped goldnanoparticles in presence of hydrogen tetrachloroaurate(III) and trisodium citrate dehydrate.

0.01 % $HAuCl_4$ solution was prepared by adding 0.5 ml of 2% $HAuCl_4$ stock solution in 99.5 ml of Milli-Q water in an Erlenmeyer flask. The solution was brought to boiling temperature by moderately stirring on a hot plate. The flask was covered with an aluminum foil to avoid excess evaporation. As soon as the solution begins boiling, 1% TSC solution was added while keeping the solution boiling. After 10 minutes the color of the solution changed to bright red indicating the formation of citrate capped, negatively charged spherical gold nanoparticles [59, 60, 100]. Then the flask was removed from the hot plate and chilled. The amount of TSC added determines the average diameter of the gold nanoparticles. The amount of citrate ion concentration versus the average gold nanoparticle diameter is shown in table 3.3. The average diameter of gold nanoparticles was determined by SEM using the open source image analysis software “image J.” The nanoparticle solution was stored in a fridge and was stable for more than a month.

Citrate ion concentration (w/v)	0.010 % (w/v)	0.015 % (w/v)	0.020 % (w/v)	0.025 % (w/v)	0.030 % (w/v)	0.035 % (w/v)	0.040 % (w/v)	0.050 % (w/v)	0.060 % (w/v)
Average gold nanoparticle diameter (nm)	52 ± 6	37 ± 4	25 ± 3	20 ± 2	18 ± 2	15 ± 2	12 ± 1	11 ± 1	10 ± 1

Table 3.3: The average diameter of gold nanoparticles versus citrate ion concentration.

3.3.2 Synthesis of PAA-PEG 2000 copolymer

0.11g K-PO_4 was dissolved in 8 ml of water then 14 mg (8 µmol) of PAA was added and stirred at pH 6.0 at room temperature. 192 mg (1 mmol) of EDC and 24 mg (200 µmol) of NHS were dissolved in 2.0 ml of K-PO_4 [86, 101]. The two solutions were then mixed and the carboxyl group of the poly(acrylic acid) was activated, and this was observed by pale turbidity in the solution. After 20 min 200 mg (100 µmol) of PEG2000 in 8 ml of K-PO_4 was added to the reaction mixture by moderate stirring at room temperature. Then the pH was set to about approximately 8.2 by titrating the reaction mixture with 1 M NaOH solution. The pH was controlled for the next 30 minutes. If needed additional NaOH solution was added to keep the pH constant. The reaction mixture was moderately stirred for the following 10 hours. For the purification the final mixture were dialyzed in deionized water for at least 8 hours by a cellulose membrane (MWCO 12400).

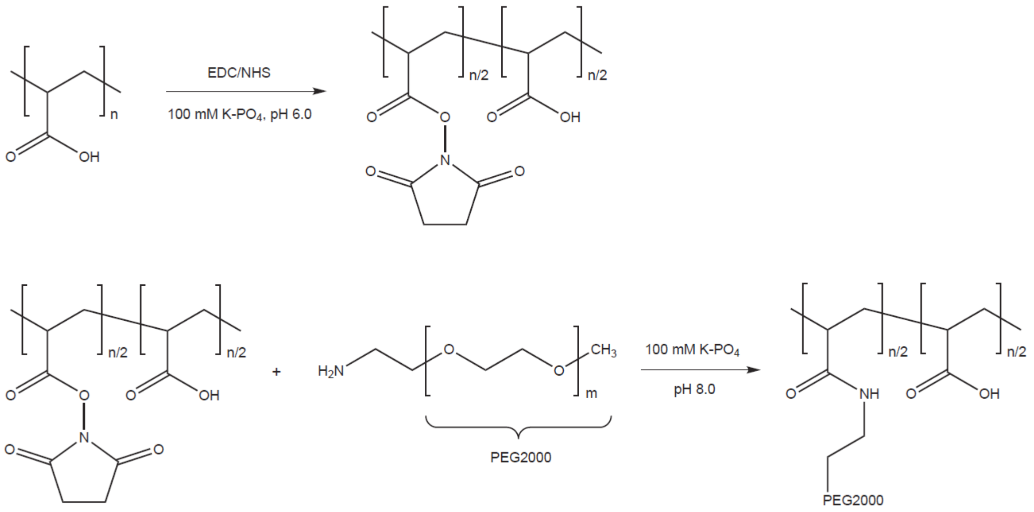

Figure 3.2: Reaction mechanism of PAA-PEG2000 copolymer synthesis

3.4 Preparation of surface coatings

3.4.1 Silane coating on silicon wafer

Silanization by (3-Aminopropyl)triethoxysilane (APTES):

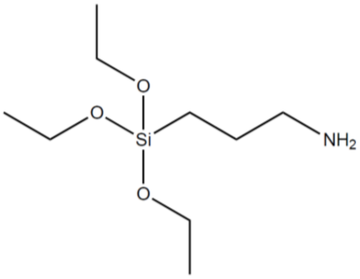

Figure 3.3: Molecular structure of 3-aminopropyl triethoxysilane

By using a magnetic stirrer, 0.5 ml of APTES is dissolved in 100 ml of methanol to obtain a final concentration of 0.5% (v/v). Cleaned silicon wafers were immersed into the APTES solution and incubated for one hour at room temperature. The wafers were then washed in excess of methanol twice for 10 minutes each. Then the wafers were placed in an ultrasonic cleaner for ten minutes to remove possibly physisorbed silane layers.

Silanization by 2-[methoxy(polyethylenoxy)propyl] trichlorosilane (MTCS) in gas phase

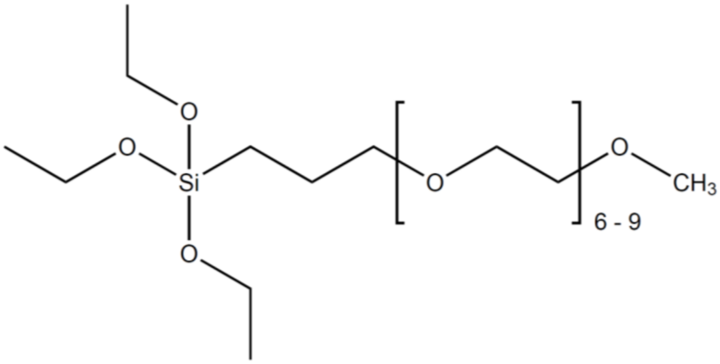

Figure 3.4: Chemical structure of 2-[methoxy(polyethylenoxy)propyl]trichlorosilane.

The setup for the chemical vapor deposition of MTCS on silicon wafers is shown in Figure 3.5. The setup consists of a vacuum compatible round bottom flask with a two neck lid and perforated porcelain plate with a manometer, a rotary pump, a hot plate with temperature controller, oil bath, connection pipes and several turncocks. 20 µl of MTCS (90%) was dripped into the round bottom flask, cleaned wafers were put onto the porcelain plate, placed into the flask, and the lid was closed. The rotary pump was turned on and the system pressure reduced to roughly 10 mbars (limit of the pump). The system was kept at this pressure for 30 minutes to remove water moieties before initiating temperature induced evaporation of MTCS. On a hot plate an oil bath was placed and the temperature was brought to 90^0C and kept constant by a temperature controller. The round bottom flask under vacuum was carefully placed into the 90^0C oil bath and covered with an aluminum foil for heat isolation. After pumping the system for one hour, the rotary pump was turned off and the vapor pressure of the MTCS was observed by the manometer. When the system pressure exceeded 50 mbars, the pump was turned on and system pressure brought to 10 mbars. This cycle is repeated for 6 hours. After venting the system, samples were taken out of the flask and were chilled to room temperature. Then the wafers were placed in an ultrasonic cleaner for ten minutes to remove possibly physisorbed silane layers.

Wafers were dried in a nitrogen stream and they were stored in a fridge under argon atmosphere until further use.

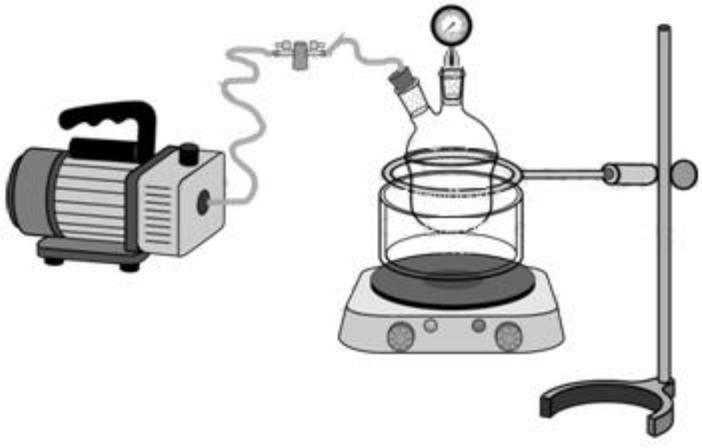

Figure 3.5: Sketch of the gas phase silanization setup.

Silanization by 2-[Methoxy(polyethylenoxy)propyl] trichlorosilane (MTCS) in liquid phase.

80 µl of 2-[methoxy(polyethyleneoxy)]propyl] trichlorsilane were dissolved in 12 ml dichloromethane (DCM) in a glass petri dish. Cleaned silicon wafers were immersed into the mixture. To avoid evaporation of DCM, the petri dish was sealed by a paraffin film. The petri dish was then placed on a platform shaker and shaken very gently for 16 hours. Then the wafers were taken out and washed in excess DCM twice for 10 minutes each. Next, the wafers were placed in an ultrasonic cleaner for ten minutes to remove possibly physisorbed silane layers. Wafers were dried in a nitrogen stream and they were stored in a fridge under argon atmosphere until further use.

3.4.2 Polyelectrolyte coating on silicon wafers

Poly(allylaminehydrochloride) (PAH) coating:

500 mg of poly(allylaminehydrochloride) were dissolved in 500 ml of Milli Q water by using a vortex mixer for one minute. Then 500 ml of potassium phthalate Ph 4.0 buffer solution was added to obtain a final concentration of 0.5% (w/v).

Cleaned silicon wafers were immersed into the solution and incubated for two hours at room temperature. Next the wafers were then placed in an ultrasonic cleaner for ten minutes to remove possibly physisorbed PAH layers. Wafers were then rinsed with Milli-Q water, dried in a nitrogen stream and stored in a fridge under argon atmosphere until further use.

Poly(styrenesulfonate) (PSS) coating:

500 mg of poly(styrenesulfonate) was dissolved in 500 ml of Milli-Q water by using a vortex mixer for one minute to obtain a final concentration of 1% (w/v). Cleaned silicon wafers were immersed into the solution and incubated for two hours at room temperature. Next, the wafers were placed in an ultrasonic cleaner for ten minutes to remove possibly physisorbed PSS layers. Wafers were then rinsed with Milli-Q water and dried in a nitrogen stream. They were stored in a fridge under argon atmosphere until further use.

PAA-PEG2000 Coating:

500 mg of PAA-PEG2000 was dissolved in 500 ml of Milli-Q water by using a vortex mixer for one minute to obtain a final concentration of 1% (w/v). Cleaned silicon wafers were immersed into the solution and incubated for two hours at room temperature. Next, the wafers were taken out and placed in an ultrasonic cleaner for ten minutes to remove possibly physisorbed copolymer layers. Wafers were then rinsed with Milli-Q water and dried in a nitrogen stream.

3.4.3 Poly(ethyleneglycol)methacrylate (PEGMA) film coating on silicon wafers

Prior to PEGMA graft polymerization, the silicon wafer surface must be coated with the initiator molecule bromoisobutrylbromide. To achieve this goal, 600µl of triethylamine (Et_3N) (dried over KOH) were dissolved in 30 ml of dichloromethane. APTES coated silicon wafers were immersed into the solution and temperature was lowered to 0 ^{0}C by placing the mixture into an ice bath. Very gently 150 µl of bromoisobutrylbromide (BIBB) was added and the reaction mixture was kept at 0 ^{0}C for 1 hour and then at room temperature for 4 hours. Next, the silicon wafers were taken out and washed with ethylacetate and ethanol, respectively, for ten minutes each. Wafers were dried in a nitrogen stream and stored in a fridge under argon atmosphere until further use if they were not directly undergoing PEGMA polymerization.

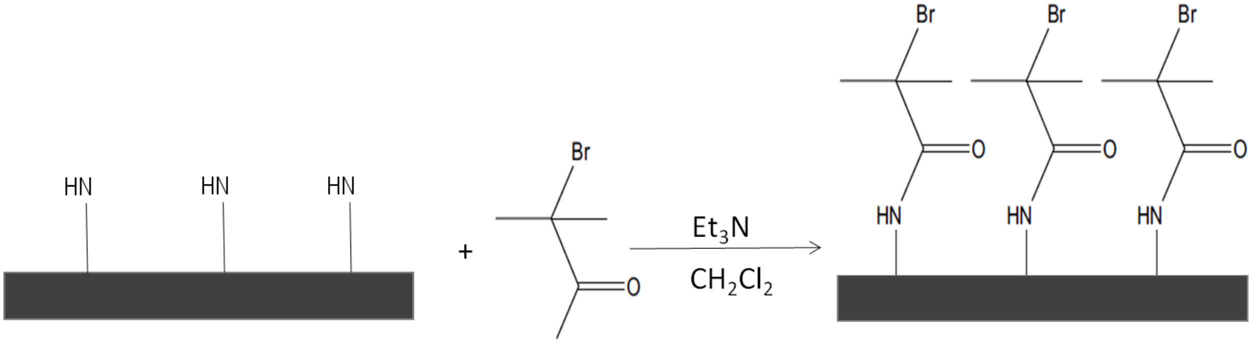

Figure 3.6: Reaction scheme for BIBB coating.

In a vacuum compatible round bottom flask (with two neck lid) 141 mg 2,2'-bipyridyl (bipy, 0.90 mmol) was dissolved in 10 ml water/methanol (1:1) mixture. Then 5 ml of PEGMA and 64 mg of copper(I) bromide (0.45 mmol) were added to the mixture and the brown reaction mixture was degassed three times and sonicated for 3 min under nitrogen atmosphere. Then the flask was placed on a platform shaker and moderately shaken for approximately one hour to dissolve all CuBr. A glass Petri dish was placed in a desiccator and the BIBB functionalized silicon wafers were put into it. Very quickly the reaction mixture was discarded onto the substrates and the desiccator evacuated and aerated with nitrogen three times. Polymerization was allowed to take place for 20 hours. Oxygen in the Petri dish or in the desiccator must be avoided. Both, the concentration of the monomer and the polymerization time affect the resulting PEGMA film thickness. After polymerization, wafers were flushed extensively with water inside the Petri dish until all residues of the polymerization solution were rinsed out. Next the wafers were incubated 15 min in water and then 15 min in DMF inside the Petri dish. Finally, the wafers were washed two times with methanol for 2 min each, and they were dried in a nitrogen stream.

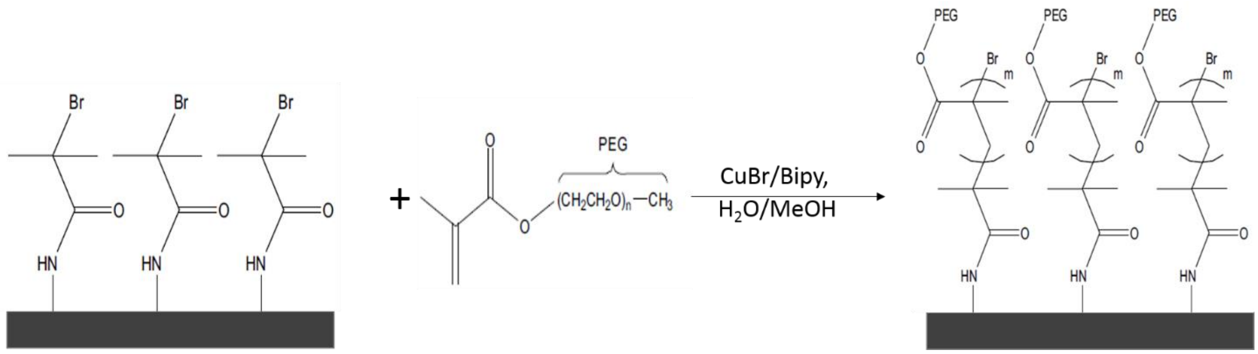

Figure 3.7: Reaction scheme of PEGMA growth on silicon wafer.

3.4.4 O-(2-mercaptoethyl)-O′-(2-carboxyethy)heptaethylene glycol (EG7-SH) coating

8 µl of EG7-SH was dissolved in 10 ml of EtOH in a glass Petri dish, then the silicon wafer substrates with metal coating or metal nanoparticles were immersed into the solution. After overnight process, samples were washed five times for 2 min each with EtOH, and 2 times for 2 min each with water. Afterwards samples were dried by nitrogen stream and kept under inert atmosphere in fridge if they were not going to be used directly.

3.5 Nanoparticle adsorption

Nanoparticle deposition by self-assembly floating

The commercially available silica nanoparticle solution (25-50 mg/ml, from *Micromod* Partikeltechnologie GmbH) was sonicated 10 minutes prior to use. 100 µl of the solution was applied to the surface of a glass slide cleaned in piranha solution. Afterwards, the glass slide was slowly dipped into a vessel, which was filled with approximately 250 ml of Milli-Q water, so that particles started to form monolayers at the air-water interface. To consolidate the particle film, the water surface tension was reduced by adding 10 µl of 2 wt% aqueous SDS solution and 10 µl of Triton-X (1:400 in methanol). In this way a quasi-hexagonal, densely packed monolayer of particles was obtained at large lateral scales. Finally, the nanoparticle layer was transferred to a silicon substrate –

either coated with a homogeneous polyelectrolyte film or not – by immersion of the substrate into the liquid at a shallow angle and subsequent slow withdrawal.

Electrostatic deposition of nanoparticles

Homogeneously PAH or APTES coated or charge heterogeneous PAH/PSS nanopatterned substrates undergo AuNP adsorption when immersing the wafers into a solution of negatively charged gold nanoparticles. Wafers were incubated for 8 hours to obtain maximum gold nanoparticle coverage. The gold nanoparticle coverage can be tuned by varying the incubation time. Gold nanoparticles with bigger average diameter need longer time to reach maximum coverage. Table 3.4 shows the variation of gold nanoparticle density for particles with an average diameter of 15 nm on PAH coated silicon wafers as a function of incubation time.

Incubation time (Min.)	0,5	1	2	3	5	10	30	60	120
Coverage %	1.1 %	2.0 %	2.9 %	4.5 %	5.7 %	7.2 %	17.2 %	20.5 %	20.5 %
# of AuNPs per μm^2	56	102	149	225	287	362	862	1025	1032

Table 3.4: density of gold nanoparticles deposited on PAH coated silicon wafers as a function of incubation time. The average diameter of the gold nanoparticles is 15 nm.

3.6 Metal thin film decoration of substrates

Sputter coating

Au and Ti thin films were sputter-coated on silicon wafers by using a MED 020 Modular High Vacuum System (Bal-Tec AG (Leica Microsystems), Wetzlar/Germany). The wafers were put onto the sample holders and the system was evacuated to less than 9x10^{-5} mbar. For Au coating, argon pressure was set to 5x10^{-2} mbar and, depending on the intended film thickness, current and exposure time parameters chosen according to Table 3.5. For Ti coating argon pressure was set to 1.3x10^{-2} mbar and, depending on the intended film thickness, current and exposure time were chosen according to Table 3.6. To remove the oxide layer on Ti source surface, a blank process was made for five seconds prior to substrate coating process.

Au Film Thickness (nm)	5	10	15	20	25	30
Current (mA)	30	30	30	30	60	60
Time (s)	18	35	50	67	30	35

Table 3.5: Au metal film sputter coating parameters

Ti Film Thickness (nm)	1	2	3	4	5	10
Current (mA)	60	60	60	60	60	120
Time (s)	12	24	36	48	60	58

Table 3.6: Ti metal film sputter coating parameters

Electroless gold plating

Aqueous solutions of 0.1 wt% hydrogen tetrachloroaurate(III) trihydrate ($AuCl_4.3H_2O$) and 0.04 M hydroxylamine hydrochloride (NH_2OH) were prepared separately. These two solutions were then mixed in a ratio of 7:3 and applied to the substrate surface immediately. Depending on the intended size and form, different incubation times were chosen ranging from 10 sec to 600 sec. To terminate the reaction, the substrates were flushed with excess water. Then they were rinsed with water and dried in a nitrogen stream.

3.7 Colloidal mask cleaning techniques

Ultrasonic cleaning

An ultrasonic bath (Sonomatic 1800, Longford Ultrasonics, Coventry, United Kingdom), operated at 33 kHz with a heater, was used to remove colloidal mask particles. The container of the ultrasonic bath was filled with deionized water to an adequate level. Substrates were then separately placed in 20 ml glass snap-cap bottles and filled with 1 M NaCl solution, Milli-Q water, DMF or bullet particle solution (the preparation of bullet particle solutions is explained in detail in the

"Nanoparticle blasting cleaning" section) and put into the ultrasonic cleaner. The cleaning solution type, duration of the ultrasonic cleaning, and process temperature were chosen according to the surface properties of the substrate and the type of mask particles intended to be removed. Table 3.7 shows the cleaning parameters for the different types of nanoparticle masks. Processes longer than 10 minutes gave rise to extensive temperature increase due to acoustic cavitation. If the substrate needed to be protected from extensive heating, the temperature of the deionized water in the container was controlled regularly during the process by an external thermometer. To keep the temperature around room temperature, small ice cubes were put into the container at certain time intervals. After the ultrasonic cleaning process, samples were taken out of the snap-cap bottles and rinsed with water and placed again in the ultrasonic bath in a snap-cap bottle which is filled with Milli-Q water for 30 sec. Then the samples were rinsed with water and dried in a nitrogen stream.

Colloidal Mask Type	**Cleaning Solution**	**Duration**	**Temperature**
PS particles Ø>100nm	Milli-Q water	2 minutes	Room Temperature
PS particles 70nm<Ø<100nm	DMF	30 minutes	50 ^{0}C
Silica particles Ø>100nm	Milli-Q water	2 minutes	Room Temperature
Silica particles Ø<90nm	Bullet Particle Solution	1-40 minutes	Room Temperature
Au particles Ø>90nm	1M NaCl solution	5 minutes	Room Temperature
Au particles Ø<90nm	Bullet Particle Solution	1-40 minutes	Room Temperature

Table 3.7: Ultrasonic cleaning parameters for different types of colloidal mask particles.

Nanoparticle blasting cleaning

Standard acoustic cleaning techniques in the ultrasonic regime are not capable to remove mask nanoparticles having diameters less than 100 nm (this number can change ± 20% depending on particle type, solvent type, ultrasound frequency, process temperature and duration). To reduce this size limit, a new technique named “nanoparticle blasting cleaning” was developed. The technique is based on adding commercially available nanoparticles to the cleaning solution and generating bullet particles via implosion of cavitation bubbles produced by ultrasound waves. Samples intended to be cleaned from mask particles were put into 20 ml glass snap-cap bottles and filled with Milli-Q water. Then depending on the mask particle and substrate, bullet nanoparticle type and concentration were chosen according to Table 3.8. Process period is between 1 to 40 minutes.

Bullet Particle Type	Average Diameter	Concentration
Polystyrene	80	0.07 % (w/v)
Polystyrene	190	0.07 % (w/v)
Polystyrene	1500	1.1 % (w/v)
Silica	500	0.25 % (w/v)
Gold	60	0.01 % (w/v)

Table 3.8: Bullet particle solution parameters for different types of colloidal mask particles.

After the nanoparticle blasting cleaning process, samples were taken out of the snap-cap bottles, and rinsed with water. Afterwards, they were placed again in the ultrasonic bath in a snap-cap bottle which is filled with Milli-Q water for 30 sec. Then the samples were rinsed with water and dried in a nitrogen stream.

3.8 Layer by Layer Deposition

For the preparation of *honeycomb-like structures*, PAH- or PAH/PSS-coated silicon wafers with adsorbed nanoparticle mask were used as substrates. The substrates were successively immersed in solutions of the oppositely charged polyelectrolyte (PAH or PSS) for 10 min and washed twice with 3 M NaCl solution for 1 min after each deposition step. This cycle was repeated until the desired number of layers was adsorbed. Afterwards, the films were washed with deionized water. For the generation of *donut-like structures*, uncoated silicon substrates with adsorbed nanoparticle mask were successively immersed in a solution of PAH and PSS to deposit one PAH/PSS bilayer. Washing procedures were applied as described above. Finally, the nanoparticle mask was removed by sonication in aqueous solution for two minutes in an ultrasonic bath operated at 33 kHz.

3.9 Protein Quantification Experiments (ELISA)

The area of the substrates was determined by weighing them and using their thickness and density (ρ_{Si} = 2.336 g/cm^3) to calculate for the area (at least six replicates are essential). Adequate portions of PBS, AcBS, ABTS, BSA and GO_x stock solutions were taken out of the fridge and warmed up to room temperature. Horseradish peroxidase-tagged antibody solution (HRPO) was prepared freshly, 2.5 µL horseradish peroxidase-tagged goat anti-rabbit antibody (0.8 mg/mL) was diluted to 2 mL with AcBS to obtain a final concentration of 1 µg/mL. Half of the replicate samples were incubated in 3 mL GOx for 1 hour at ambient temperature with moderate shaking. They were then washed thrice with 3 mL PBS for 10 minutes each (the substrates were never allowed to dry out while changing solutions). All replicate samples were incubated in 3 mL BSA (10mg/ml) for 1 hour at ambient temperature with moderate shaking. This was followed by the addition of 5 µL primary antibody (rabbit anti-*Aspergillus niger* glucose oxidase), overnight incubation, and washing thrice with PBS as previously done. The samples were incubated again in 3 mL BSA 10mg/ml) for 1 hour followed by the addition of 5 µL secondary antibody (goat HRPO-tagged anti-rabbit), overnight incubation and washing with PBS.

Each of the samples was glued to the frosted side of a 10 × 10 × 40 mm polystyrene cuvette equipped with a stir bar, and 2.25 mL ABTS and 750 µL AcBS, both preheated to 37 °C, were added. While the temperature was kept at 37 °C and the solution stirred, 2 µL 30% hydrogen peroxide was added and the absorbance at 405 nm was monitored every 15 seconds for 3 minutes. For the calibration curve, 2.25 mL ABTS was pipetted into a 10 × 10 × 40 mm cuvette equipped with a stir bar. Afterwards, varying amounts of HRPO (1 µg/mL) were added and the solution was diluted to 3 mL with AcBS (refer to the Table 4.9 for the amounts of HRPO and AcBS) to obtain a final concentration of 3 to 120 ng/mL HRPO. Next, 2 µL 30% hydrogen peroxide was added and the absorbance at 405 nm was also monitored every 15 seconds for 3 minutes while the temperature was kept at 37 °C and the solution stirred.

Final HRPO concentration (ng/mL)	Stock HRPO (µL)	AcBS (µL)
3	9	741
5	15	735
10	30	720
20	60	690
30	90	660
40	120	630
50	150	600
60	180	570
70	210	540
80	240	510
90	270	480
100	300	450
110	330	420
120	360	390

Table 3.9: Amounts of HRPO and AcBS added to 2.25 ml of ABTS solution to generate the calibration curve.

The reaction rates for the 14 HRPO runs were obtained by plotting the absorbance against time and the method of least squares (linear regression) was used to determine the slope, which resembles the reaction rate. The reaction rates for each run were then plotted against the HRPO concentration and linear regression was used to find the correlation between reaction rate (rate of change in absorbance) and HRPO concentration. The reaction rates for the replicate samples were obtained in the same manner and compared to the calibration curve in order to quantify the concentration of the bound horse radish peroxidase-tagged antibody (HRPO-AB). The amount of GOx adsorbed (in terms of mass per area [ng/cm^2]) was calculated based on the ratio of the molecular weights of GOx and HRPO-AB(M_{GOx} = 131 kDa, $M_{HRPO-AB}$ = 181 kDa) and the assumption that on average one HRPO-AB binds to one glucose oxidase molecule this assumption was discussed extensively in references [86, 102].

3.10 Enzyme activity tests

Enzymatic conversion of ß-D-glucose to D-gluconolacton by GOx is not directly detectable by spectroscopic techniques. Enzymatic activity of the GOx is indirectly determined by employing the dye molecule ABTS and the enzyme HRPO. The indirect detection of GOx activity was done based on the following chemical reactions.

$$\text{GOx} + \text{O}_2 + \beta\text{-D-Glucose} \underset{k_{-1}}{\overset{k_1}{\rightleftharpoons}} [\text{GOx} + \beta\text{-D-Glucose}]^* + \text{O}_2 \xrightarrow{k_2} \text{GOx} + \text{D-Gluconolacton} + \text{H}_2\text{O}_2$$

$$\text{HRPO} + 2\ \text{ABTS} + \text{H}_2\text{O}_2 \underset{k_{-3}}{\overset{k_3}{\rightleftharpoons}} [\text{HRPO} + \text{ABTS}]^* + \text{H}_2\text{O}_2 \xrightarrow{k_4} \text{HRPO} + 2\ \text{ABTS}^+ + 2\ \text{OH}^-$$

In the activity measurement experiments, the concentration of HRPO was selected excessively higher than the concentration of GOx (c(HRPO) >> c(GOx)) to ensure that GOx was determining the reaction rate.

1.74 mM ABTS (in acetate buffer), 10 mg/ml HRPO (in acetate buffer) and 2.5M ß-D-glucose (aqueous) solution was prepared freshly and warmed up to 37 ^{0}C in a water bath. Samples were prepared analogous to the ELISA experiment and glued to disposable cuvettes. After 5 – 10 min they stuck properly to the cuvettes so that the experiments could be continued. To avoid loss of activity, high attention was paid that the samples did not dry. Then the cuvettes were filled with the appropriate amount of ABTS and HRPO solution according to Table 3.10. Afterwards samples were put into a temperature controlled cuvette holder and it was waited for about 20 min until temperature equilibrated at 37 °C). Then the GOx solution was added under moderate stirring and the measurement was started. UV-Vis spectra was recorded in every 15 sec for an overall period of 3 min. This measurement was done for 15 different substrate concentrations ranging from 1 mM to 500 mM.

Reactant	**Amount added in 3 ml cuvette**
ABTS	2670 µl @ c(Glucose) ≤ 250 mM 2370 µl @ c(Glucose) > 250 mM
HRPO	30 µl
β-D-Glucose	300 µl @ c ≤ 250 mM 600 µl @ c > 250 mM

Table 3.10: Amounts of reactant solutions used in the GOx activity test.

For every GOx concentration, the extinction at λ = 405 nm was plotted against time. Data points were linearly fitted and the slope, corresponding reaction rate (V), was calculated. Then the slope versus GOx concentration was plotted. The resulting hyperbolic curve was fitted according to following mathematical relation (equation 3.1) where "y" refers to reaction rate, "x" refers to substrate concentration, P1 and P2 refers to numerical constants:

$$y = \frac{P1\,.\,x}{P2+x} \qquad \textit{(equation 3.1)}$$

According to Michalis-Menten kinetic theory, the velocity of the color reaction as a function of substrate concentration follows equation 3.2. V_{max} is the maximum reaction rate, [S] is the substrate concentration (GOx) and K_M (Michaelis-Menten constant) is the substrate concentration at ½ V_{max} (defines the substrate affinity of the enzyme).

$$v = \frac{v_{max} \cdot [S]}{K_M + [S]} \qquad \textit{(equation 3.2)}$$

The specific enzyme activity of GOx, A, was defined in equation 4.3 by employing Lambert-Beer´s law.

$$A = \frac{v_{max}}{2 \cdot \varepsilon_{405}\left(ABTS^{+}\right) \cdot d \cdot [GOx]_0} \qquad \textit{(equation 3.3)}$$

$\varepsilon_{405}(ABTS+) = 36800\ l\ mol^{-1}\ cm^{-1}$ (molar extinction coefficient of the dye)

d = 1 cm (path length of the cuvette)

$[GOx]_0$ = initial concentration of enzyme on the sample surface

3.11 Measuring techniques

3.11.1 X-ray photoelectron spectroscopy (XPS)

XPS measurements were performed on a MAX200 spectrometer (Leybold-Heraeus, Hanau/Germany) equipped with a Specs EA200 multichanneltron detector, AlKα (1486.6 eV) and MgKα (1253.6 eV) X-ray sources. All measurements were carried out with MgKα radiation using the parameters shown in Table 3.11. All XPS spectra were later on normalized with the device specific transmission function because the sensitivity of the detector depends on the energy regime. For analysis, Shirley background subtraction was employed. The corresponding signals were fitted and the area under the signals was determined with XPSPEAK software version 4.1.

Orbitals	Start energy [eV]	End energy [eV]	Step Width [eV]	Dwell time [ms]	Pass energy [eV]	# Scans of
Overview	1000	-4.0	0.4	10	96	3
Au4f	91	72	0.2	40	48	10
C1s	291	270	0.2	100	48	20
N1s	411	390	0.2	250	48	24
O1s	561	520	0.2	40	48	16
Si2s	166	140	0.2	100	48	16

Table 3.11: Standard XPS measurement parameters

3.11.2 Scanning electron microscopy

Images were recorded with a scanning electron microscope (SEM; Leo 1530, Zeiss, Jena, Germany) at an accelerating voltage of 2 kV. The microscope is equipped with two different detectors: an Everhart-Thornly and an in-Lense detector. Samples were mounted on the sample holder with an electrically conductive carbon tape. The image analysis were done by using the software ImageJ (open source image processing program developed at the National Institutes of Health).

3.11.3 Atomic force microscopy

Images were recorded with an atomic force microscopy (AFM; Solver Next, NT-MDT, Eindhoven, Netherlands) in the non-contact mode. Images were analyzed with the software Gwyddion (version 2.31). The properties of the cantilevers (NT-MDT Co., Moscow, Russia) that were used in the measurements are listed in Table 3.12.

Cantilever Type	HA_NC Type A	HA_NC Type B	NSG10-A	DP18/GP
Length (µm)	87	117	95	225
Width (µm)	32	32	30	100
Thickness, h, (µm)	1.75	1.75	2.0	-
Force constant, (N/m)	3.5	12.0	11.8	3.5
Resonant Frequency (kHz)	140	235	240	-

Table 3.12: Properties of non-contact mode cantilevers used in the analysis.

3.11.4 Ellipsometry

Ellipsometric film thickness determination was done with an ellipsometer from J.A. Woollam Co. Inc., Typ M44. The instrument is equipped with a xenonarc lamp as a light source with a spectrum ranging from 400-800 nm. The angle of incidence is set to a fixed value of 75°. The instrument was calibrated using a thermally oxidized silicon substrate with a SiO_2 layer of approximately 25 nm on top. The intensity of the reflected elliptical polarized light is measured with a 60 Hz rotating polarizer (analyzer). The organic film was modeled as a single Cauchy layer with n0 = 1.45 and A = 0.01 μm^2 as Cauchy parameters. A single ellipsometric scan was acquired at three different points for each sample, and the average of those three values was taken to determine the layer thickness.

4 RESULTS AND DISCUSSION

In this thesis, we have investigated the impact of surface nanostructures on the molecular activity of adsorbed proteins. The underlying idea was to restrict surface-bound proteins to adsorption sites of well-defined size and chemical functionality in order to prevent unfolding and loss of their biological function. By varying the geometrical properties of the adsorption sites, we have tried to deliberately tune the activity of the immobilized biomolecules.

In order to characterize the samples by spectroscopic methods, the surfaces have to be nanostructured in macroscopic dimensions corresponding to the beam diameter of the respective analytical technique. As the formation of nanostructures on such a large scale was not achievable by top-down lithographic methods with reasonable expenditure of time and cost, self-assembly processes based on colloidal lithography were used instead.

In the first part of the results and discussion chapter, we present bottom-up and generally applicable nanopatterning methods which facilitate the preparation of long-range ordered 2D and 3D polymeric or metallic patterns with various geometries. Colloidal lithography and five different surface derivatization methods were employed to generate nanopatterned surfaces for specific protein adsorption. In the second part we present protein quantification and enzyme activity measurements on some of these nanopatterned surfaces.

4.1 Generating Nanopatterned Surfaces by Colloidal Lithography

To produce long-range ordered nanopatterned structures for site-specific protein adsorption, several methods can be employed. On the other hand if it is intended to confine single proteins in each adsorption site, one is facing complex challenges which have to be put into account beforehand. Producing chemically contrasted, long-range ordered and large-scale (centimeter regime) nanopatterned structures with feature sizes between 10 and 100 nm is the main challenge. Other challenges are directing proteins to the proposed adsorption sites and finding feasible ways to detect the adsorbed proteins both qualitatively and quantitatively. In the first part of this chapter, we present five different ways to generate these nanopatterned structures. All these different techniques were developed to fulfill different types of requirements. Adsorption sites in different size regimes with different surface chemistry and geometries were fabricated by employing adequate technique. The common basis of all these fabrication techniques was colloidal lithography. In this thesis we used colloidal nanoparticles for two different purposes: they are used as masking agent or as adsorption site itself. To use the nanoparticles as masking agents, monodisperse nanoparticles are deposited as hexagonally or randomly closed packed monolayers on silicon substrates. The nanoparticle monolayer acts as a mask in chemical derivatization of the surface by blocking nanometer size surface areas by particle/surface contact. After removal of the particles, the uncoated surface regimes were used as adsorption sites. Monodisperse spherical gold and silica particles with a wide range of diameters were used to synthesize structures with large diversity in size.

4.1.1 Synthesis of metal-semiconductor nanopatterns by colloidal lithography for site specific protein adsorption.

The approach presented in this section is based on colloidal lithography. Randomly closed packed monolayers of monodisperse gold nanoparticles were adsorbed onto polyelectrolyte coated silicon substrates as shown in Figure 4.1. Then the substrate was coated with a thin gold or titanium layer by sputter coating. By removal of the particles in an ultrasonic bath, adsorption sites were obtained, which size was determined by the projection of the nanoparticles on surface. Afterwards, the surface was rendered protein resistant, e.g. by the use of EG-terminated thiols. By selecting nanoparticles of different diameter or employing the electroless gold plating technique the lateral dimensions of the adsorption sites were varied.

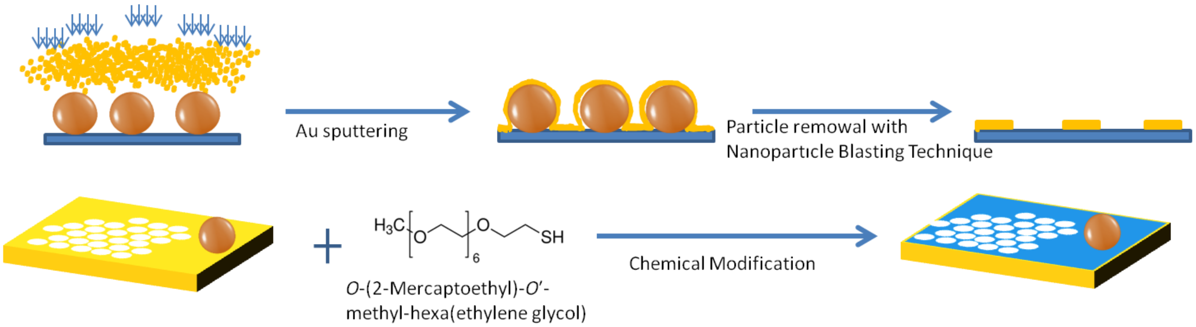

Figure 4.1: Preparation of nanostructured surfaces by colloidal lithography.

The gold nanoparticles were synthesized with the intended diameter by a well-known procedure mentioned in section 3.3.1. In this section monodisperse gold nanoparticles with diameters ranging from 10 to 60 nm were used. Nanoparticle monolayers were prepared by charge-induced particle adsorption as explained in section 3.5. Silicon was chosen as the substrate material, because of its transparency for IR radiation in the required wavelength regime and its low roughness. Titanium and gold metal coatings with thicknesses ranging from 1 to 10 nm were used. For the particle removal, a new mask cleaning technique based on ultrasonic cleaning, the so-called “nanoparticle blasting technique” was developed.

In this section the focus will be on the synthesis of protein resistant metal-semiconductor nanopatterned structures with tunable parameters. The protein adsorption experiments on these structures will be discussed in section 4.2. The synthesis will be discussed here in four subchapters: gold nanoparticle adsorption, sputter coating, mask particle removal, and tuning the dimensions and density of the adsorption sites.

4.1.1.1 Gold nanoparticle adsorption on silicon substrates

Gold metal nanoparticles were synthesized according to the procedure described in section 3.3.1. Au nanoparticles were successfully decorated on silicon substrates which were coated with the positively charged polyelectrolyte PAH. Since the gold nanoparticles are citrate capped, they are negatively charged and adsorb to the surface via electrostatic interactions between the negatively charged nanoparticles and the positively charged polyelectrolyte. The density of the gold nanoparticles on substrate was regulated by changing the incubation time of the substrates in the gold nanoparticle solution. As depicted in Figures 4.2 and 4.3, particle density increases with increasing incubation time and then reaches a saturation point. The coverage of the gold nanoparticles was calculated with respect to incubation time by analyzing them with SEM and the software Image J (Table 3.1).

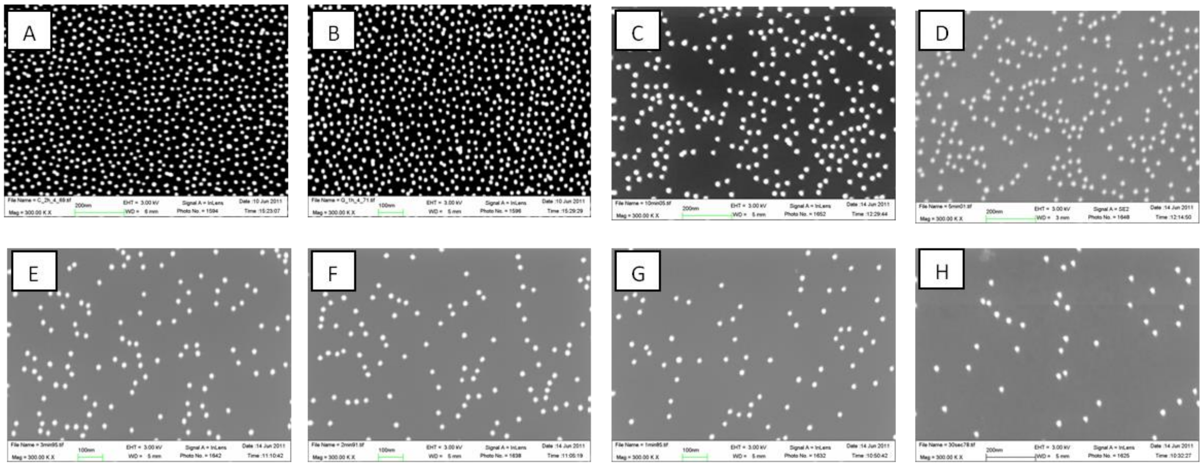

Figure 4.2: SEM images showing the relation between gold nanoparticle density and incubation time. 15 nm gold nanoparticles were adsorbed on PAH coated silicon substrates by changing incubation time: a) 120, b) 60, c) 30, d) 10, e) 5, f) 3, g) 2, and h)1 min.

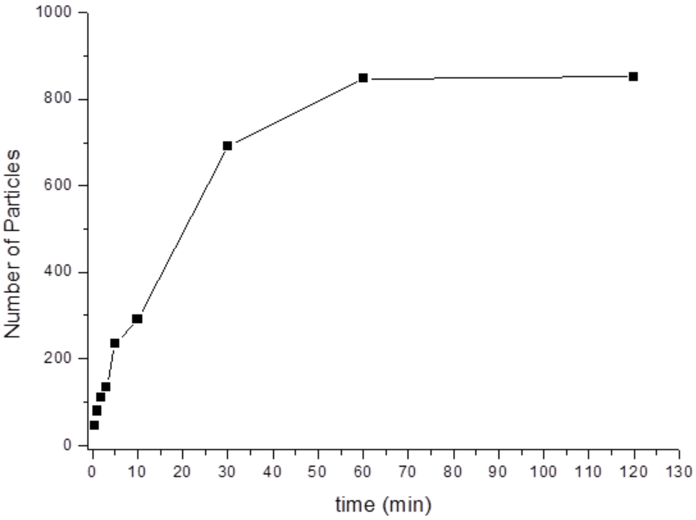

Figure 4.3: Number of gold nanoparticles (15 nm diameter) in 0.8 μm^2 surface area counted by image analysis software, image J, and plotted against incubation time. In the first 30 minutes, the density of the particles shows a linear increase with increasing incubation time. Saturation starts after this point and maximum coverage is reached 60 min. after incubation started.

Incubation time (min.)	0.5	1	2	3	5	10	30	60	120
Coverage (%)	1.1	2.0	2.9	4.5	5.7	7.2	17.2	20.5	20.5

Table 4.1: Coverage of PAH coated silicon substrates with gold nanoparticles (15 nm diameter) as a function of incubation time. The analysis was performed with the software Image J.

4.1.1.2 Sputter Coating

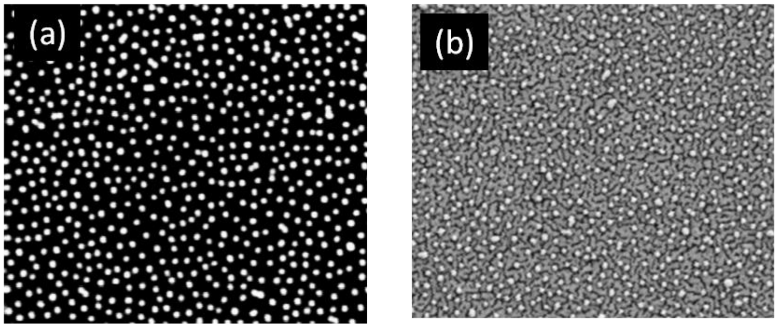

Figure 4.4: SEM images of gold nanoparticles (15 nm diameter) deposited silicon substrates taken before (a) and after (b) 5 nm gold sputtering.

It has been possible to prepare different thicknesses of the Au and Ti metal coatings by changing the time of sputter coating process. In order to find the optimum metal coating thickness and type, 1 and 2 nm of Ti and 5, 8 and 10 nm of Au were sputter coated on silicon substrates. In several cases, for Au sputtering, 1 or 2 nm of Ti layer was used as an adhesion promoting layer. SEM images of randomly closed gold nanoparticles on silicon substrates taken before and after the sputter coating process are shown in Figure 4.4. 5 nm Au film thickness on 1 nm Ti coating was determined as optimum with respect to the efficiency for particle removal and structure rigidity.

4.1.1.3 Mask particle removal

The adsorbed particles are bound to the surface through van der Waals forces, electrostatic forces, capillary forces, and chemical bonds. Among these, van der Waals forces dominate the interaction between the particle and the surface [63, 64]. Van der Waals forces decrease linearly with decreasing particle size. However, forces based on drag effects are proportional to cross-sectional area of the particle. Therefore, the removal of the particles becomes more and more difficult as the particle size decreases [63].

In this study we employed two different approaches for mask particle removal concept by ultrasonic cleaning. The first approach was to simply tune the parameters of the ultrasonic cleaning technique in order to lower the size limit for removal to some extent. The parameters were solvent type, process temperature, ultrasound frequency, pH of the solution and addition of surfactant molecules. By selecting optimum parameters, the size limit was brought down by 10-20%. However, when it is intended to remove gold nanoparticles having size down to 10 nm with ordinary ultrasonic cleaner, we had to approach the problem with an innovative idea. The solution was mixing additional nanoparticles to the cleaning solvent, where the particles (named as bullet particles) were accelerated close to supersonic velocities by the implosion of cavitation bubbles, thus generating high speed, one-to-one collisions with mask particles. This technique was named "nanoparticle blasting cleaning". By varying the bullet particle type and concentration, sensitivity and effectivity of the cleaning process could be deliberately tuned.

Nanoparticle blasting cleaning

Under this title, we have developed a new, cheap, simple and fast cleaning technique to remove sub 60 nm mask nanoparticles from metal film coated silicon substrates. After developing the technique, the main effort was put on matching the optimum cleaning parameters (particle type, particle concentration, process duration) specifically for each sample according to surface parameters (metal film type, metal film thickness, mask particle diameter). A cross-over study was done to understand the relation between these two sets of parameters by doing controlled experimental series and characterizing the cleaning efficiency and structure durableness for each case. More than 400 samples were fabricated and analyzed by SEM and the software Image J after the cleaning process. After analysis of each sample a rating was given to each sample considering the metal film quality and the removal efficiency of mask particles.

Ultrasonic cleaners work by two principle mechanisms: cavitation and acoustic streaming. The cavitation bubbles are formed when the ultrasonic waves constructively combine leading to a pressure minimum below the vapor pressure of the fluid medium [63]. Then they subsequently collapse when the ultrasonic wave passes through the pressure maximum. The bubble implosion creates a void, which is quickly filled with surrounding fluid creating a microjet liquid flow. This fluid flow causes generation of shock waves which rip the mask particles off.

Acoustic streaming is time-independent liquid flow generated by sound field. The flow generates drag forces to remove mask particles. In general, cavitation and acoustic streaming, work together and their relative strength is a function of ultrasound frequency. For removal of sub micrometer mask particles at low frequencies such as 35-40 kHz (most common commercial range) the cavitation mechanism provides dislodging the particles from the substrate and acoustic streaming carries the already detached mask particles away to prevent re-attaching. On the other hand, when particle diameter decreases, the fluid drag forces caused from cavitation implosions cannot overcome van der Waals and electrostatic forces which bind the particle to surface. At low frequencies (35-40 kHz), the boundary layer thickness (thickness of motionless fluid layer surrounding surface) for acoustic streaming is in the order of microns so that small particles can hide easily.

The technique presented here is based on addition of nanoparticles to the cleaning solvent of the ultrasonic cleaner. Polystyrene particles with 80, 190, 1500 nm, silica particles with 500 nm and gold nanoparticles with 60 nm diameter were used in different concentrations as additives to the cleaning solvent. Our speculation about the cleaning mechanism with this technique has been depicted in Figure 4.5. The additional nanoparticles are accelerated in ultrasonic cleaner tanks by the implosions of cavitation bubbles at low frequencies (35-40 kHz). When these microscopic bubbles implode (due to the passage of the rarefaction energy, the moving sound wave), they produce microscopic jets of liquid that can accelerate bullet particles in the media and results in high-speed, one-to one collisions with mask particles. Studies about ultrasonic cavitation mention that the pressure created by implosion is about 35-70 MPa and the velocity of micro-streaming around 400 km/h [63]. Cumulative effect of millions of continuous tiny implosions in the liquid medium is what provides the necessary mechanical energy to accelerate nanoparticles and results in millions of collisions to remove physically bound mask particles from substrate surface.

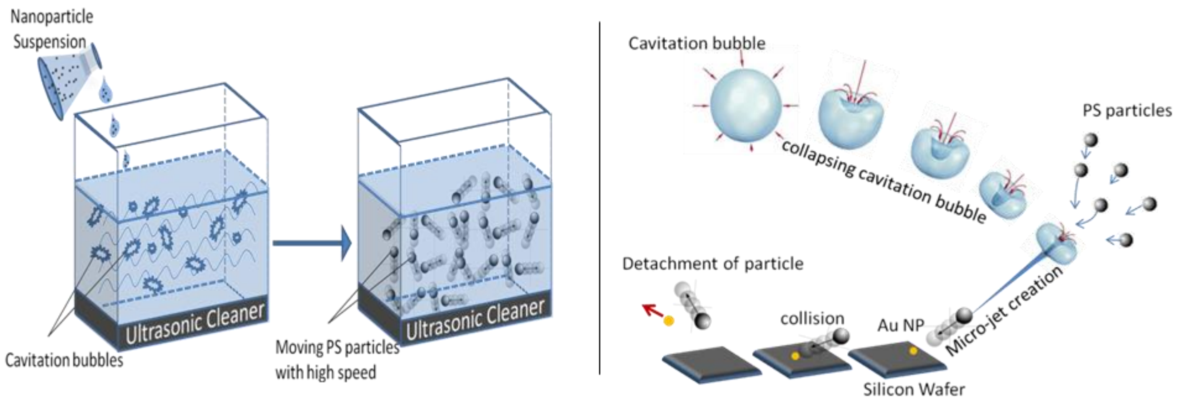

Figure 4.5: Schematic representation of nanoparticle blasting technique.

It was found that size, type and concentration of the bullet particles in the cleaning solvent directly affect the cleaning efficiency. As shown in the following, the nanoparticle blasting technique is capable of removing mask particles with sizes down to 10 nm with an ordinary ultrasonic cleaner. The preliminary tests of this technique were done by using gold nanoparticles deposited on PAH coated silicon substrates. Later the technique was optimized to remove mask particles which are embedded into thin metal films without damaging the metal coating.

In Figure 4.6 SEM images of gold nanoparticles deposited on silicon substrates are shown before and after treating them in an ultrasonic cleaner in the presence of 90 nm PS particles, 1500 nm PS particles and water only. The drastic contribution of bullet particles to the cleaning process can be easily seen in the SEM images. They were taken exactly from the same area of the substrates before and after the cleaning process. Gold nanoparticles with 15 nm diameter deposited on PAH coated silicon substrates were efficiently removed in the presence of 80 nm PS particles. Presence of 1500 nm PS particles were also positively contributed to the process but their efficiency is lower than that of the smaller particles. As expected, removal of 15 nm mask particles only in the presence of water did not work.

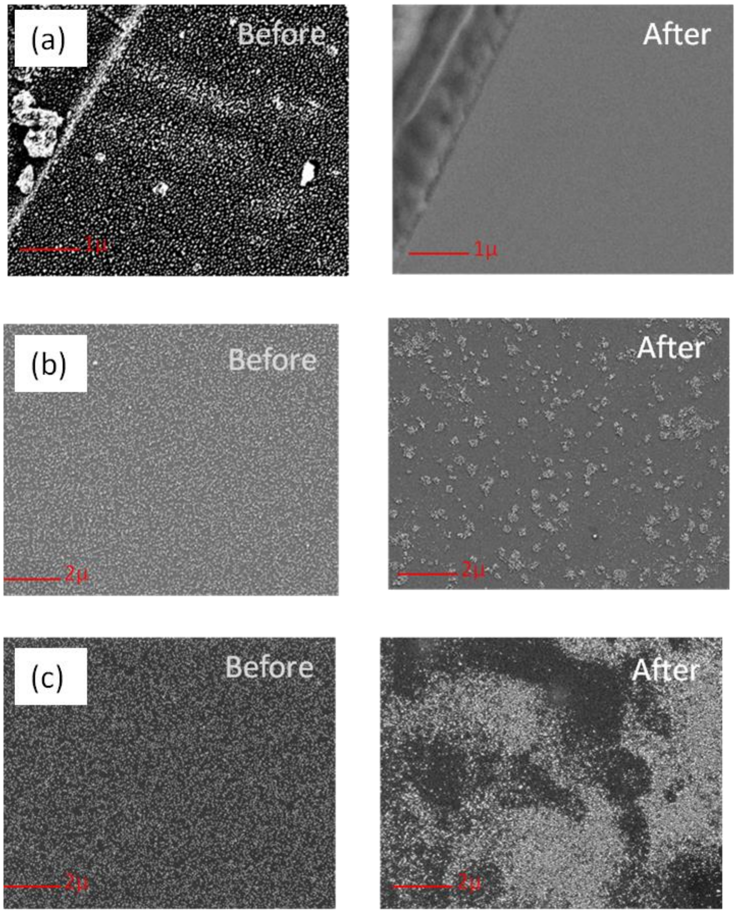

Figure 4.6: SEM images of gold nanoparticles (15 nm in diameter) deposited on silicon substrates before and after the cleaning process. a) addition of 80 nm PS particles (0.07 % (w/v)), 10 min. process time, b) addition of 1500 nm PS particles (1.1 % (w/v)), 10 min. process time, c) only water as cleaning solvent, 60 min. process time. The experiments took place at RT.

Optimization of nanoparticle blasting technique for synthesis of high yielded nanopatterns

Two sets of parameters were optimized by designing controlled experimental series. The first set of parameters was related to the surface nanopatterns which were intended to be generated by colloidal mask particles. These parameters were: mask particle diameter and metal coating type. The second set of parameters was defining the nanoparticle blasting process conditions. These were: process time, particle type, particle diameter and particle concentration. In the first run, the mask particle diameter and process time were kept constant at 25 nm 10 min., respectively, and the other parameters were changed according the Table 4.2. The samples were analyzed by SEM and the software Image J.

An efficiency rating was given to each sample and by iterating the parameters this rating was tried to be improved in the next rounds. Efficiency rating contains letter "F" or letter "P" with a number as shown in the table. "F" refers to fail; this rating was given to a sample if the loss of metal coating layer was more than 10% after nanoparticle blasting cleaning. To analyze the metal coating loss percentage, 5 random areas with dimensions of 20x20 μm were chosen under SEM, the coverage of metal coating layer was analyzed by Image J, and their average was taken. If the metal coating loss is less than 10% the letter "P" was given (referring the word passed). The number next to letter "P" defines the particle removal efficiency by comparing the number of removed mask particles before and after cleaning process. This efficiency calculation was done by choosing 3 random 10 μm^2 areas under SEM and analyzing them by the software Image J. Then the percentage of particle removal was rounded to multiples of 10%.

Metal Coating	**Bullet Particle Type**	**Bullet Particle Concentration**	**Cleaning Efficiency Rating**
1 nm Ti + 5 nm Au	81 nm PS	0.02 % (w/v)	P40
1 nm Ti + 5 nm Au	81 nm PS	0.07 % (w/v)	P100
1 nm Ti + 5 nm Au	81 nm PS	0.20 % (w/v)	F
1nm Ti	81 nm PS	0.02 % (w/v)	F
1nm Ti	81 nm PS	0.07 % (w/v)	F
1nm Ti	81 nm PS	0.20 % (w/v)	F
2nm Ti	81 nm PS	0.02 % (w/v)	P10
2nm Ti	81 nm PS	0.07 % (w/v)	F
2nm Ti	81 nm PS	0.20 % (w/v)	F
2nm Au	81 nm PS	0.02 % (w/v)	F
2nm Au	81 nm PS	0.07 % (w/v)	F
2nm Au	81 nm PS	0.20 % (w/v)	F
5nm Au	81 nm PS	0.02 % (w/v)	P30
5nm Au	81 nm PS	0.07 % (w/v)	P90
5nm Au	81 nm PS	0.20 % (w/v)	F

2 nm Ti + 8 nm Au	81 nm PS	0.02 % (w/v)	P10
2 nm Ti + 8 nm Au	81 nm PS	0.07 % (w/v)	P70
2 nm Ti + 8 nm Au	81 nm PS	0.20 % (w/v)	P100
1 nm Ti + 5 nm Au	194 nm PS	0.02 % (w/v)	P50
1 nm Ti + 5 nm Au	194 nm PS	0.07 % (w/v)	P90
1 nm Ti + 5 nm Au	194 nm PS	0.20 % (w/v)	F
1nm Ti	194 nm PS	0.02 % (w/v)	F
1nm Ti	194 nm PS	0.07 % (w/v)	F
1nm Ti	194 nm PS	0.20 % (w/v)	F
2nm Ti	194 nm PS	0.02 % (w/v)	F
2nm Ti	194 nm PS	0.07 % (w/v)	F
2nm Ti	194 nm PS	0.20 % (w/v)	F
2nm Au	194 nm PS	0.02 % (w/v)	P10
2nm Au	194 nm PS	0.07 % (w/v)	F
2nm Au	194 nm PS	0.20 % (w/v)	F
5nm Au	194 nm PS	0.02 % (w/v)	P10
5nm Au	194 nm PS	0.07 % (w/v)	P90
5nm Au	194 nm PS	0.20 % (w/v)	F
2 nm Ti + 8 nm Au	194 nm PS	0.02 % (w/v)	P0
2 nm Ti + 8 nm Au	194 nm PS	0.07 % (w/v)	P80
2 nm Ti + 8 nm Au	194 nm PS	0.20 % (w/v)	P100
1 nm Ti + 5 nm Au	1500 nm PS	0.35 % (w/v)	P40
1 nm Ti + 5 nm Au	1500 nm PS	1.1 % (w/v)	P80
1 nm Ti + 5 nm Au	1500 nm PS	3.3 % (w/v)	P90
1nm Ti	1500 nm PS	0.35 % (w/v)	F
1nm Ti	1500 nm PS	1.1 % (w/v)	F
1nm Ti	1500 nm PS	3.3 % (w/v)	F
2nm Ti	1500 nm PS	0.35 % (w/v)	P0
2nm Ti	1500 nm PS	1.1 % (w/v)	P30
2nm Ti	1500 nm PS	3.3 % (w/v)	F
2nm Au	1500 nm PS	0.35 % (w/v)	P20
2nm Au	1500 nm PS	1.1 % (w/v)	P40
2nm Au	1500 nm PS	3.3 % (w/v)	F
5nm Au	1500 nm PS	0.35 % (w/v)	P30
5nm Au	1500 nm PS	1.1 % (w/v)	P70
5nm Au	1500 nm PS	3.3 % (w/v)	F
2 nm Ti + 8 nm Au	1500 nm PS	0.35 % (w/v)	P20
2 nm Ti + 8 nm Au	1500 nm PS	1.1 % (w/v)	P70
2 nm Ti + 8 nm Au	1500 nm PS	3.3 % (w/v)	P100
1 nm Ti + 5 nm Au	500 nm Silica	0.08 % (w/v)	P10
1 nm Ti + 5 nm Au	500 nm Silica	0.25 % (w/v)	P60
1 nm Ti + 5 nm Au	500 nm Silica	0.75 % (w/v)	P60
1nm Ti	500 nm Silica	0.08 % (w/v)	P10
1nm Ti	500 nm Silica	0.25 % (w/v)	P10
1nm Ti	500 nm Silica	0.75 % (w/v)	F
2nm Ti	500 nm Silica	0.08 % (w/v)	P0
2nm Ti	500 nm Silica	0.25 % (w/v)	P0
2nm Ti	500 nm Silica	0.75 % (w/v)	F

2nm Au	500 nm Silica	0.08 % (w/v)	P10
2nm Au	500 nm Silica	0.25 % (w/v)	P80
2nm Au	500 nm Silica	0.75 % (w/v)	F
5nm Au	500 nm Silica	0.08 % (w/v)	P0
5nm Au	500 nm Silica	0.25 % (w/v)	P70
5nm Au	500 nm Silica	0.75 % (w/v)	P70
2 nm Ti + 8 nm Au	500 nm Silica	0.08 % (w/v)	P10
2 nm Ti + 8 nm Au	500 nm Silica	0.25 % (w/v)	P20
2 nm Ti + 8 nm Au	500 nm Silica	0.75 % (w/v)	P50
1 nm Ti + 5 nm Au	60 nm Au	0.003 % (w/v)	P50
1 nm Ti + 5 nm Au	60 nm Au	0.01 % (w/v)	P50
1 nm Ti + 5 nm Au	60 nm Au	0.03 % (w/v)	F
1nm Ti	60 nm Au	0.003 % (w/v)	P30
1nm Ti	60 nm Au	0.01 % (w/v)	F
1nm Ti	60 nm Au	0.03 % (w/v)	F
2nm Ti	60 nm Au	0.003 % (w/v)	P10
2nm Ti	60 nm Au	0.01 % (w/v)	P10
2nm Ti	60 nm Au	0.03 % (w/v)	F
2nm Au	60 nm Au	0.003 % (w/v)	F
2nm Au	60 nm Au	0.01 % (w/v)	F
2nm Au	60 nm Au	0.03 % (w/v)	F
5nm Au	60 nm Au	0.003 % (w/v)	P0
5nm Au	60 nm Au	0.01 % (w/v)	P10
5nm Au	60 nm Au	0.03 % (w/v)	F
2 nm Ti + 8 nm Au	60 nm Au	0.003 % (w/v)	P0
2 nm Ti + 8 nm Au	60 nm Au	0.01 % (w/v)	P0
2 nm Ti + 8 nm Au	60 nm Au	0.03 % (w/v)	50

Table 4.2: Ratings of samples after nanoparticle blasting cleaning with respect to changing experimental parameters. Samples were prepared by deposition of gold nanoparticles with 25 nm diameter on PAH coated silicon substrates and successive coating with six different types of metal film. The duration of nanoparticle blasting cleaning was 10 minutes and the experiments were performed at RT.

To illustrate the evaluation process, SEM images of several samples with different ratings are shown in Figure 4.7.

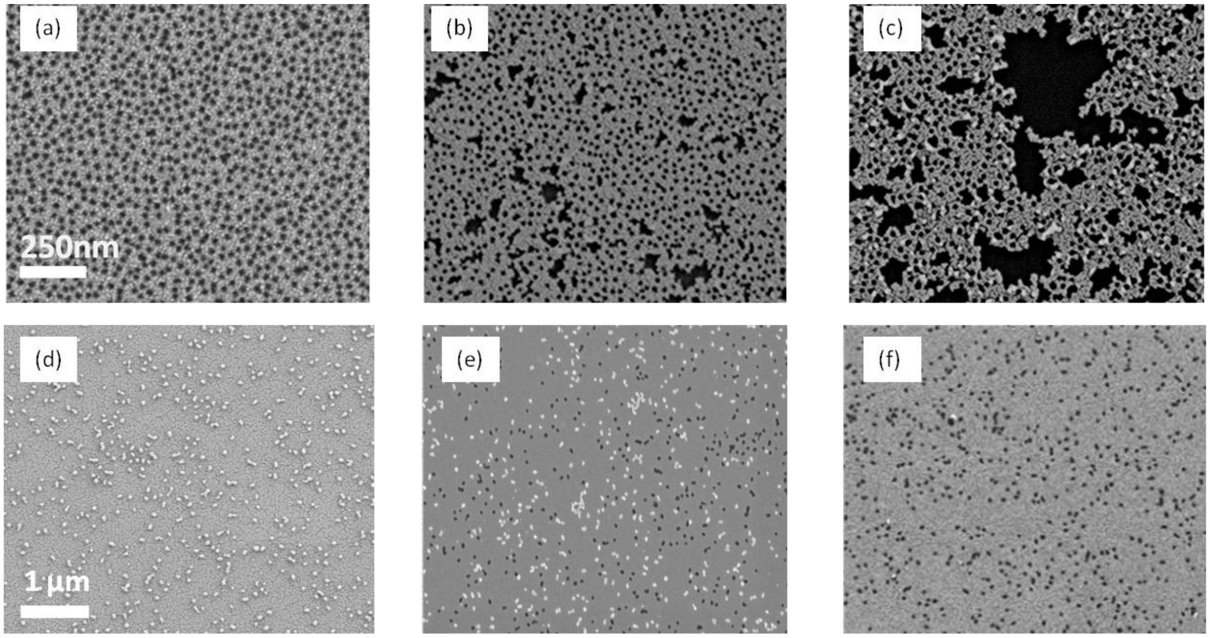

Figure 4.7: SEM images of samples after nanoparticle blasting cleaning. Ratings of the samples are a) P100, b) P100, c) F, d) P0, e) P40, and f) P100.

From Table 4.2 it is concluded that bullet particle type, size and concentration have a strong effect on mask particle removal efficiency. As a general trend, bullet particles in high concentrations has showed better removal efficiency. However, high concentrations also caused more significant damage of the metal coating layer. Au coatings thicker than 5 nm with 1 or 2 nm Ti as an adhesion promoter seemed to be the ideal to protect the robustness of the samples. In general, PS nanoparticles with 80 and 190 nm diameter showed better performance as bullet particles than the others.

With the insights from the first controlled experimental series, process time was also optimized to increase the removal efficiency for the samples with rating “P”. The efficiency was improved to some extend by increasing the process time. On the other hand, by decreasing the process time, the loss of metal coating layer was reduced.

By fine tuning within the optimized ranges, mask particles having 15 and 60 nm diameter were also removed from substrate surfaces very efficiently without damaging the metal coating layer. With this new technique and proper tuning of the process and surface parameters, the desired nanopatterns for protein adsorption have been obtained. In Figure 4.8, 4.9 and 4.10, SEM images of porous metal films with different pore diameters fabricated by efficient removal of mask particles are shown. The success of the nanoparticle blasting cleaning technique under different conditions can be seen in these SEM images.

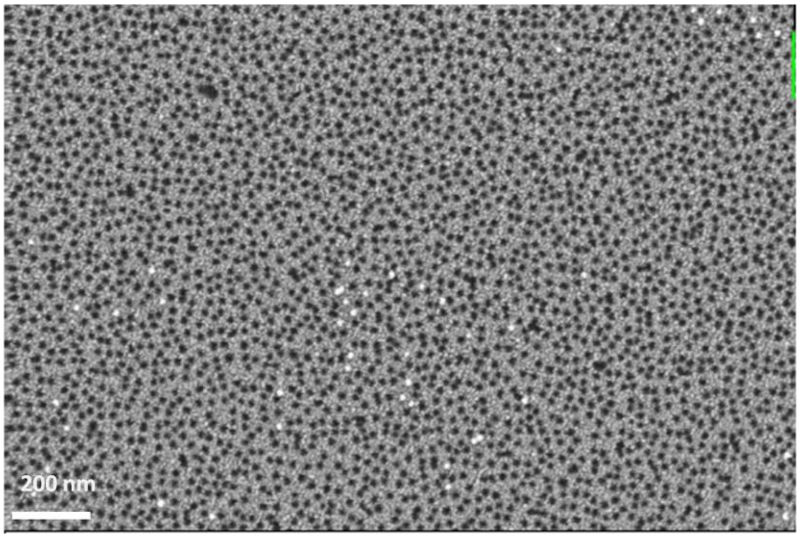

Figure 4.8: SEM image of a porous metal film produced by removal of 15 nm mask particles from 6 nm thick (1nm Ti + 5 nm Au) metal film by the use of 80 nm PS bullet particles (0.07 % (w/v)). Process time 15 min.

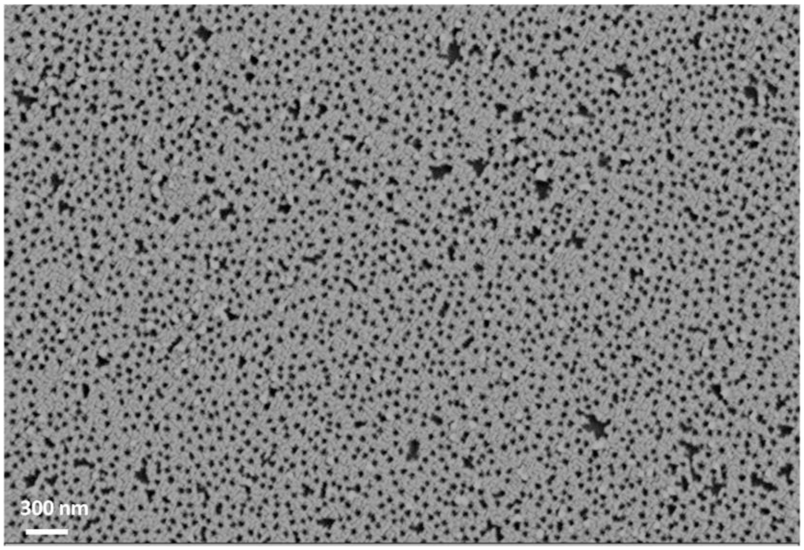

Figure 4.9: SEM image of a porous metal film produced by removal of 25 nm mask particles from 6 nm thick (1nm Ti + 5nm Au) metal film by the use of 80 nm PS bullet particles (0.07 % (w/v)). Process time 10 min.

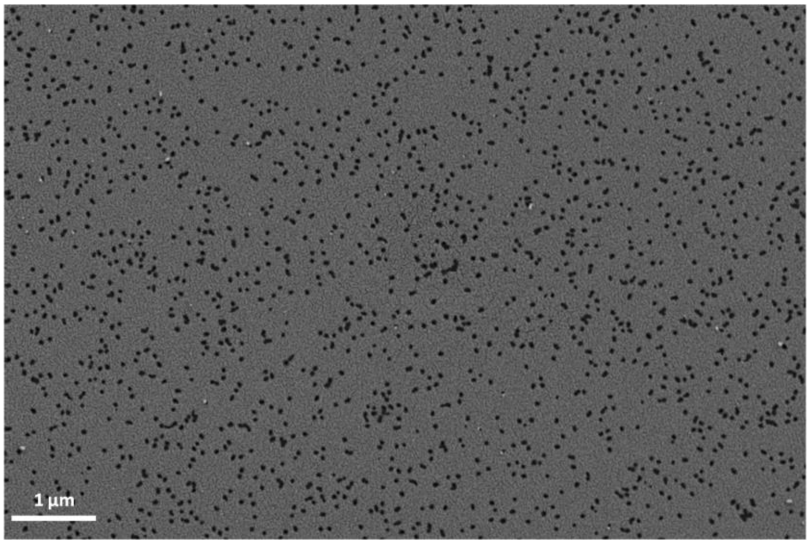

Figure 4.10: SEM image of porous metal film produced by removal of 60 nm mask particles from a 10 nm thick (2 nm Ti + 8 nm Au) metal film by the use of 190 nm PS bullet particles (0.20 % (w/v)). Process time 15 min.

In Figure 4.11, AFM images of the substrates before and after nanoparticle blasting cleaning has shown. Height profiles indicates that the metal coating was very well protected and has a uniform thickness. The depth of the pores correlates with the sputter coating parameters. According to the AFM analysis, mask particle diameter was almost same as the pore diameter.

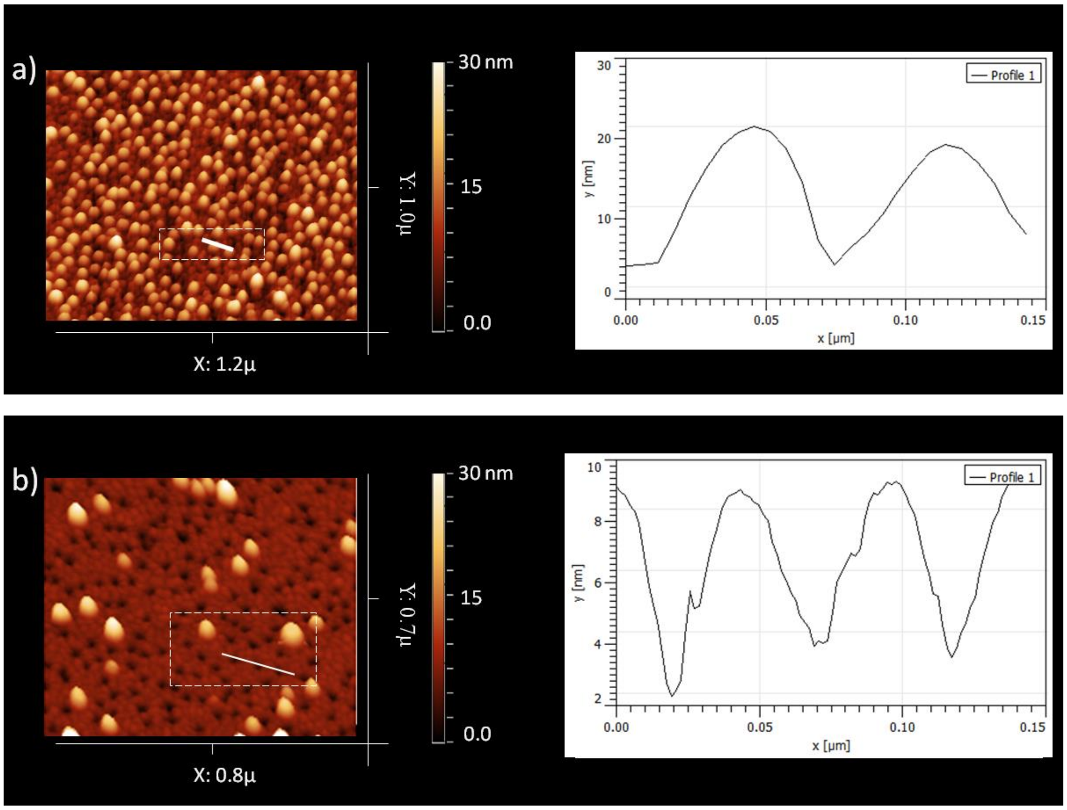

Figure 4.11: AFM images showing the surface topography a) before, b) after nanoparticle blasting technique. Samples were fabricated by deposition of 15 nm mask particles and 6 nm thick (1 nm Ti + 5 nm Au) metal film coating. The cleaning process was performed in the presence of 80 nm PS bullet particles (0.07 % (w/v)). Process time was 15 min.

4.1.1.4 Tuning the dimensions and density of the adsorption sites

After developing an efficient and sensitive mask particle removal technique, dimensions and density of the adsorption sites can be tuned with the tools of colloidal lithography. The AFM and SEM analysis has shown that the cross section of the nanoparticles directly determines the adsorption site area. By synthesizing the gold particles of intended size, using them as mask particles and removing them with the nanoparticle blasting technique, the diameter of the adsorption sizes were deliberately tuned. In Figure 4.12, SEM images of porous metal films with different pore diameters are shown.

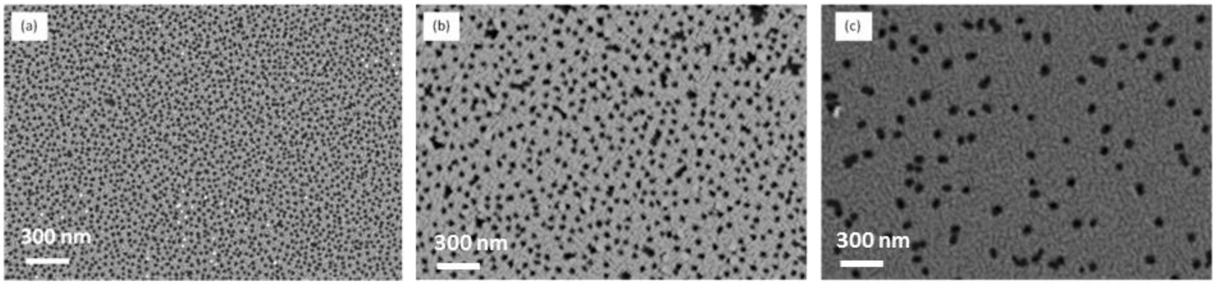

Figure 4.12: SEM images showing metal films with different pore diameter a) 15 nm, b) 25 nm and c) 60 nm.

The density of the adsorption sites was tuned by changing the density of gold nanoparticles on the substrates by changing the incubation time of the substrates in gold nanoparticle solution. In Figure 4.13, SEM images of samples having same sized adsorption sites with varying density are shown. The number of adsorption sites can be varied from 0 to 1000 per 1 μm^2 (0-60 min incubation time for 15nm mask particle) for selected experimental conditions.

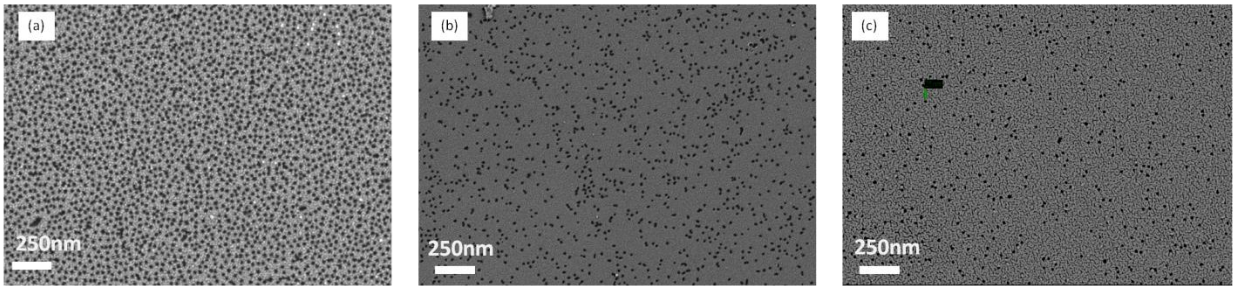

Figure 4.13: SEM images showing samples with different adsorption site densities due to to different incubation times in 15 nm gold nanoparticle solutions, a) 60, b) 10, and c) 1 min.

The depth of the pores were tuned by two mechanisms. The first approach was to change the metal film thickness deposited on the nanoparticle-coated substrate, the second one to use electroless gold plating after removal of the mask particles. Electroless plating was not only changing the depth but also the 3D geometry of the adsorption sites. In Figure 4.14 the change in the pore geometry after electroless plating has been sketched and the SEM images of the samples before and after plating has shown in Figure 4.15.

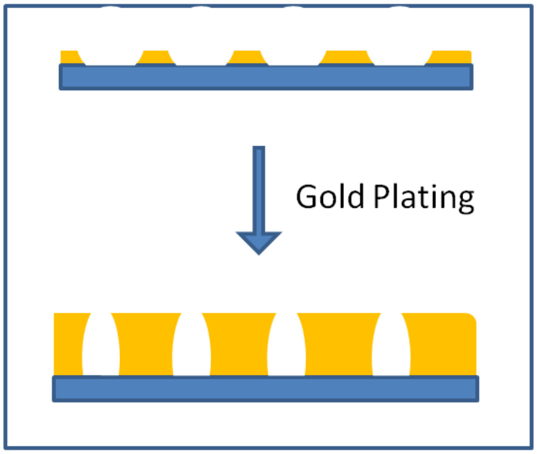

Figure 4.14: Sketch of pore geometry before and after after electroless gold plating process.

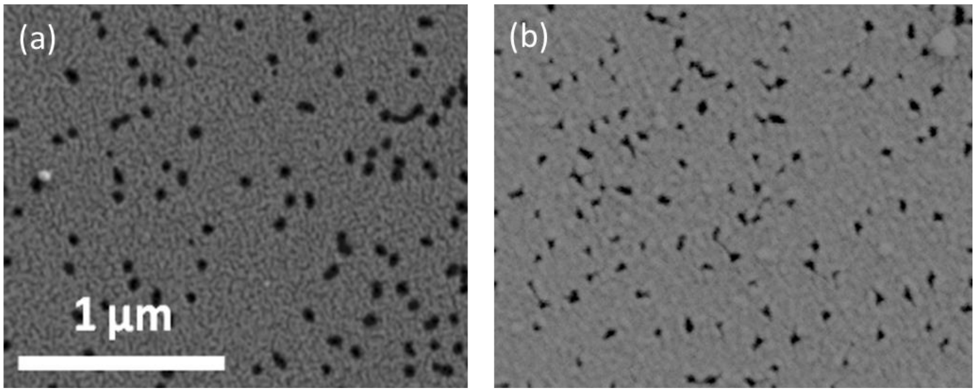

Figure 4.15: SEM images showing nanopatterned matal film a) before b) after electroless gold plating.

Electroless plating was performed in the presence of $AuCl^{4-}$ and NH_2OH for different plating times. In this way, the thin gold coating deposited on the substrate was grown in 3 dimensions, and the pores – representing the adsorption sites – became deeper and narrower.

4.1.1.5 Rendering the metal coating layer protein resistant

After fabricating adsorption sites with intended parameters, metal surfaces were rendered protein resistant by incubating the samples in EG_7-SH solution as described in the section 3.4.4. The thiol head group of the molecule enables the molecule to bind to the gold layer of the porous matrix and the ethylene glycol tail group provides the protein resistance.

4.1.2 Synthesis of charge heterogeneous 2D and 3D patterned polyelectrolyte templates via layer by layer deposition for specific protein adsorption

In this section we demonstrate a new, bottom up and generally applicable technique to fabricate nanopatterned structures for site specific protein adsorption by employing layer by layer deposition of polyelectrolytes and colloidal lithography. Positively charged PAH and negatively charged PSS were used as polyelectrolytes and amine terminated dielectric silica particles were used as colloidal mask particles to construct the nano-patterned structures. The positively charged PAA-PEG 2000 polymer was used to render specific parts of the synthesized patterns the protein repelling.

With this new fabrication technique honeycomb and donut-like polyelectrolyte nano-patterns with tunable dimensions and charge designs were fabricated (Figure 4.16). By coating specific surface areas with a protein resistant, charged copolymer (PAA-PEG 2000), intended adsorption sites for protein confinement were generated.

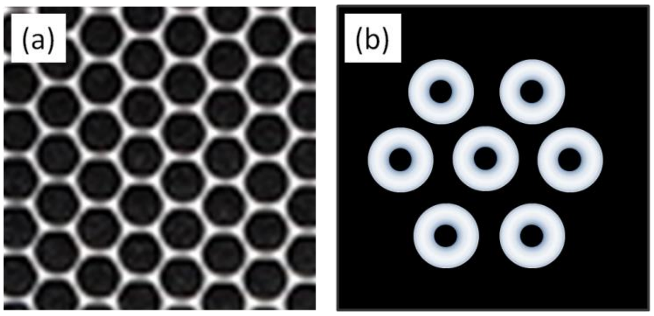

Figure 4.16: Schematic representation of a) honeycomb-like and b) donut-like polyelectrolyte nanopatterns.

Selective deposition of negatively charged gold clusters on these heterogeneously charged polyelectrolyte nanopatterns resulted in the fabrication of several 2D and 3D metal nanoparticle arrays, such as with dot, grid, ring, out-of-ring, and circular patch geometries. These different types of metal arrays generated by selective gold deposition is shown in Figure 4.16 as an overview. The details of the preparation procedures and further discussions will be given in the section 4.1.3 extensively.

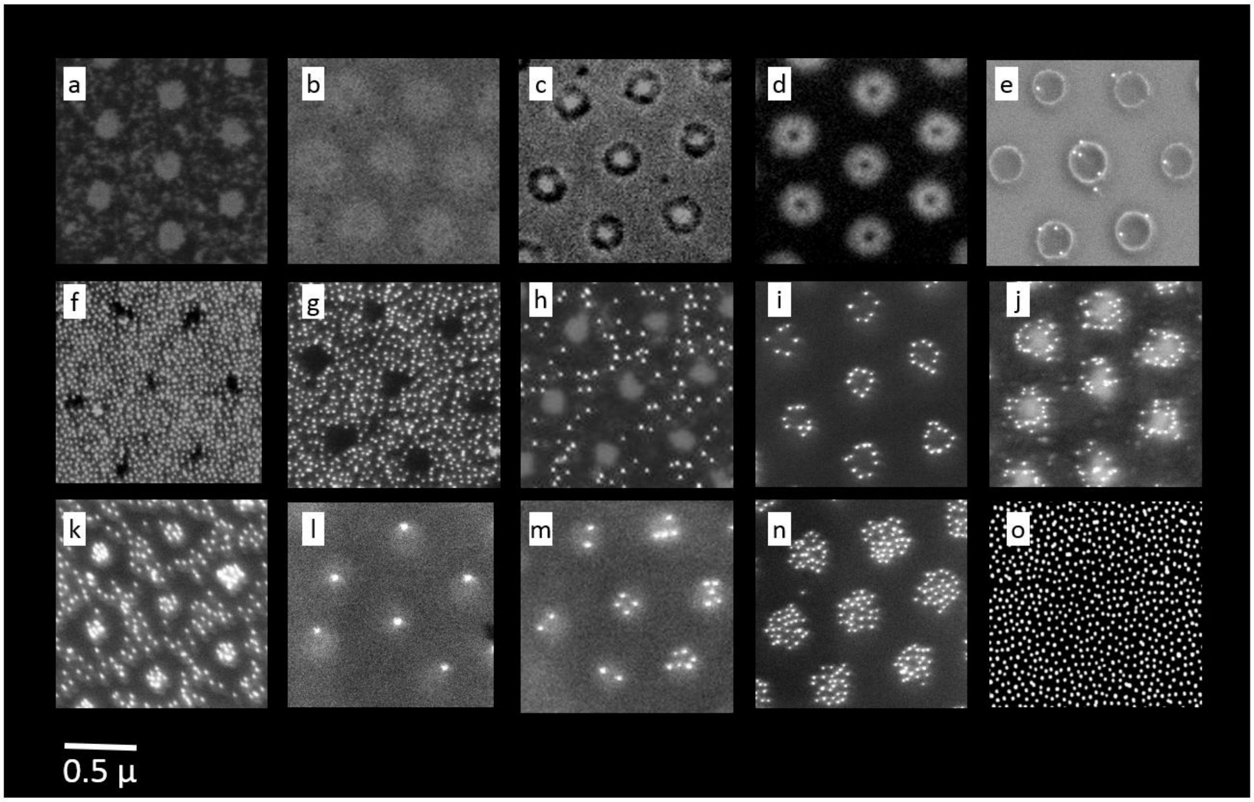

Figure 4.17: Overview on SEM images of nanopatterned structures fabricated by layer by layer assembly. Dielectric polyelectrolyte films were fabricated with a), b) honeycomb, and c), d), e) donut-like morphologies. Selective deposition of 15 nm AuNPs on heterogeneously charged polyelectrolyte templates lead to formation of metal particle nano-arrays with f), g), h) grid, i) ring, j) multi-ring k) out-of-ring, l) single-dot, m), n) circular patch, and o) tray geometries.

In this part of the thesis, we will focus on the synthesis of heterogeneously charged nanopatterns. Protein adsorption studies on these patterns will be presented in section 4.2.

4.1.2.1 Deposition of dielectric particles on substrates

There are several ways to deposit silica nanoparticles as a monolayer on the desired substrates, such as incubation, spin-coating and self-assembly floating. In this chapter, the amine terminated silica particles were deposited on substrates as hexagonally closed packed monolayer by the self-assembly floating technique. After deposition, nanoparticle density and homogeneity of the particle film was analyzed by SEM. Film homogeneity is expected to be a crucial prerequisite to fabricate long range ordered and high yield nanopatterned structures.

In literature self-assembly floating technique is generally applied to latex and polystyrene particles [52, 54]. Within the scope of this thesis it was successfully applied to amine terminated silica particles. Amine terminated silica particles were dispersed in EtOH resulting a blurry solution, and the particles were transferred to the air/water interface by using a transfer glass slide. When the vessel is illuminated by a light source, it is possible to directly watch the transfer of nanoparticles as the glass slide is immersed into the water. After transferring enough particles to the vessel (the area covered by the nanoparticle film in the vessel should be in the regime of 20-40 cm^2) SDS and Triton-X solutions were added to change the surface tension of water and obtain a densely packed nanoparticle monolayer at the air/water interface. Then the particle film can be transferred onto flat silicon wafers, glass slides, or gold-coated or polyelectrolyte terminated flat surfaces. Nanoparticle films fabricated by self-assembly floating proved to be very stable. They can undergo preparation processes in liquid phase even long periods of time without showing any deterioration.

Silica nanoparticle films with centimeter dimensions and very few defects can reproducibly be produced by self-assembly floating. The technique is also cheap and efficient: it is possible to completely cover a silicon wafer with a diameter of 10 cm consuming only 0.02 g of nanoparticles. Figure 4.18 shows a typical high-densely packed monolayer of silica nanoparticles at different magnifications deposited by self-assembly floating.

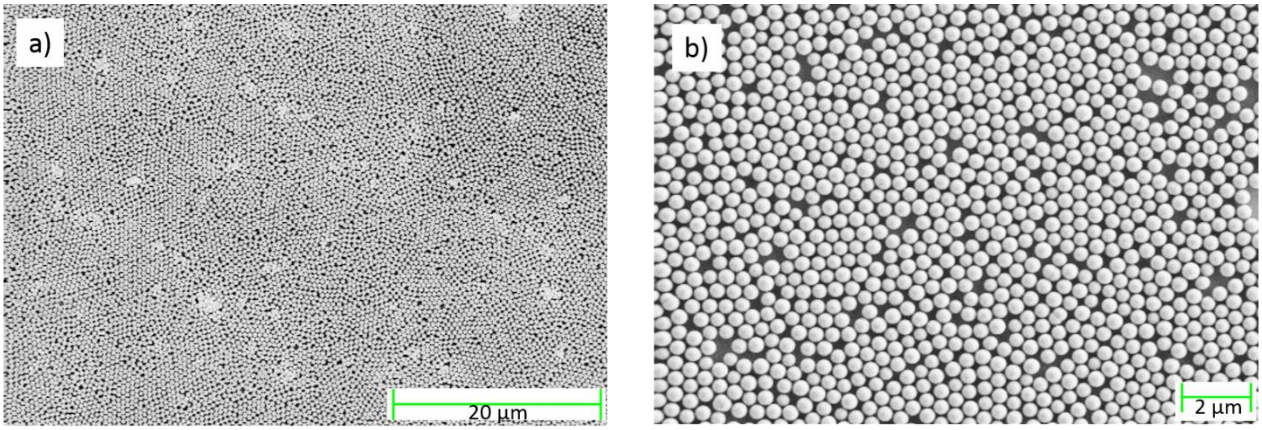

Figure 4.18: a) and b) SEM images of a monolayer of silica nanoparticles on a flat Au film deposited by self-assembly floating.

The particle diameter has a crucial effect on the homogeneity and packing density of the nanoparticle films. Particles having average diameters bigger than 500 nm show outstanding performance to form homogeneous and densely packed films. On the other hand fabricating nanoparticle films with smaller particles results in decreasing homogeneity and lower packing density together with partial multilayer formation. However, by individual optimization of the experimental parameters, the self-assembly-floating method can be used successfully for particles down to 70 nm in diameter. In Figure 4.19 nanoparticle monolayers produced with nanoparticles of different diameter are presented. Monodispersity of the nanoparticles is another important factor in the fabrication of high quality nanoparticle monolayers. Quasi-hexagonal packing of the nanoparticles can only be achieved using nanoparticles which have very small size distribution. A large size-distribution leads to the formation of point defects in the nanoparticle monolayer.

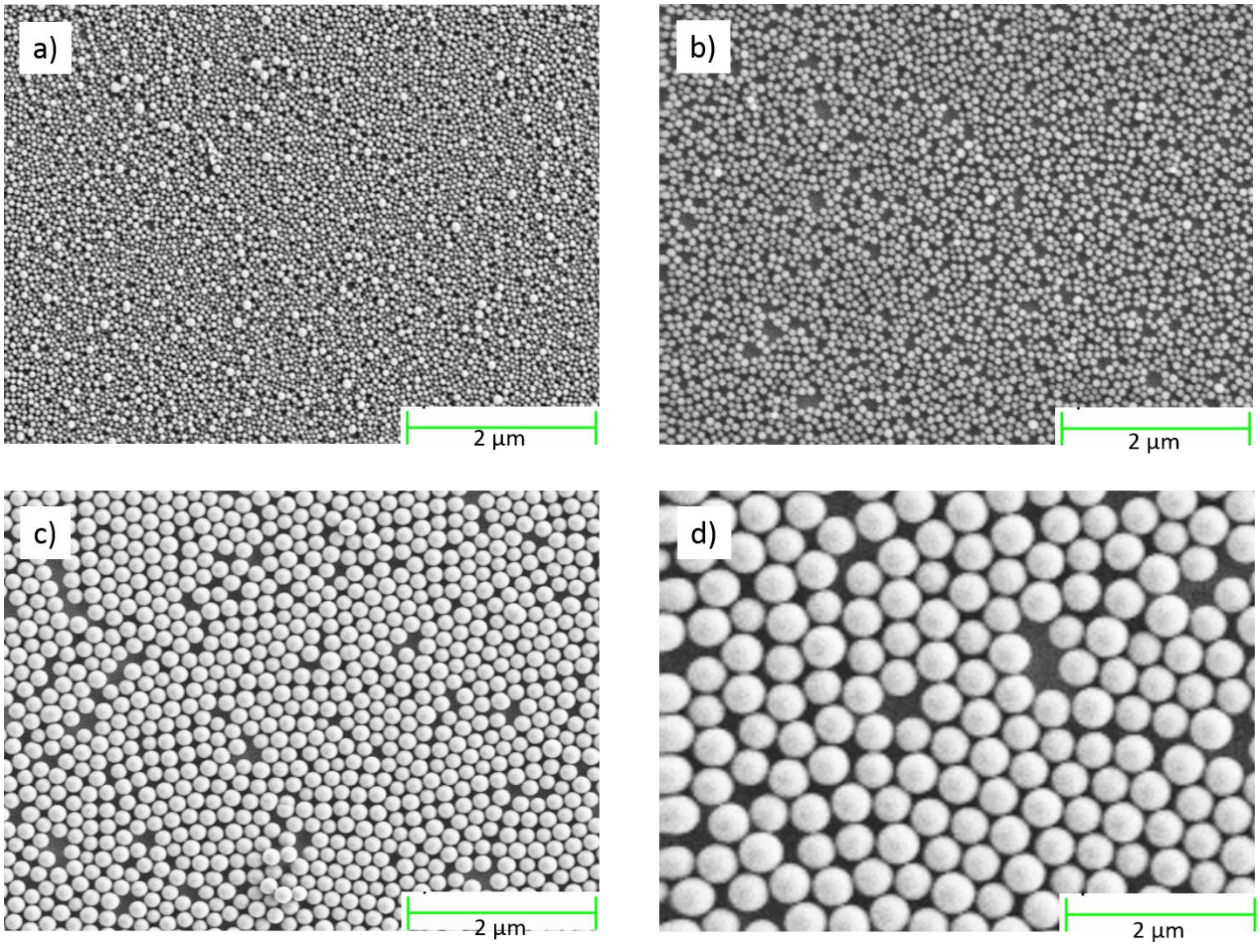

Figure 4.19: SEM images of amine-terminated silica particle monolayers on silicon substrates. The particles have average diameters of a) 70, b) 100, c) 200, and d) 500 nm.

4.1.2.2 Layer by Layer Deposition of Polyelectrolytes

We used PAH as polycation and PSS as polyanion to form thin films on substrates coated with silica nanoparticles. By ellipsometric measurements the relationship between the number of polyelectrolyte layers and the film thickness was established. As shown in Table 4.3, the average bilayer thickness is around 2.3 nm. Figure 4.20 indicates that a plot of film thickness versus the number of bilayers shows quite good linearity. In the scope of this chapter 1 to 10 single layers of polyelectrolytes were deposited onto substrates as described in the sections 3.4.2 and 3.8.

Number of polyelectrolyte layers	Thickness (nm)
+	1.8
+-	3.1
+-+	4.1
+-+-	5.3
+-+-+	6.4
+-+-+-	7.7
+-+-+-+	8.7
+-+-+-+-	10.1
+-+-+-+-+	11.2
+-+-+-+-+-	12.6

Table 4.3: Film thickness versus polyelectrolyte layers deposited on silicon substrates.

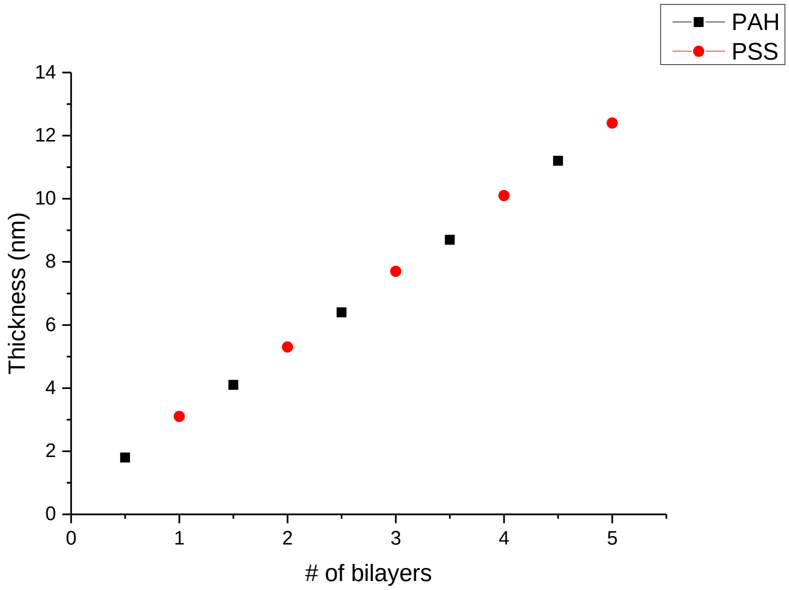

Figure 4.20: Graph showing the linear relation between the number of bilayers and the final film thickness on a silicon substrate.

4.1.2.3 Fabrication of Nanopatterned Dielectric Thin Films

We used oppositely charged polyelectrolytes to create patterned "plus/minus" polymer surfaces with numerous geometries by the combination of layer-by-layer assembly and colloidal lithography. By this combination of techniques honeycomb and donut-like patterned polyelectrolyte films with adjustable dimensions and charge designs have been obtained.

Synthesis of Honeycomb Polyelectrolyte Thin Films

Main strategies to synthesize honeycomb polyelectrolyte films with several charge designs are shown in Figure 4.21. Silicon substrates were positively or negatively charged prior to silica nanoparticle adsorption according to the intended charge design. To positively charge the surface, a single layer of PAH is deposited on the silicon wafer surface. To negatively charge the surface, the surface is coated with a PAH+PSS bilayer. After deposition of silica nanoparticles on charged surfaces by self-assembly floating, the LbL coating process was initiated by immersing the substrate into the corresponding polyelectrolyte solution for 10 min. After each layer deposition, the substrates were washed twice in water for 1 min. and immersed in the oppositely charged polyelectrolyte solution. This cycle is repeated until the desired film thicknesses is achieved. After removal of mask particles, polyelectrolyte thin films with honeycomb structure have been obtained with several charge designs.

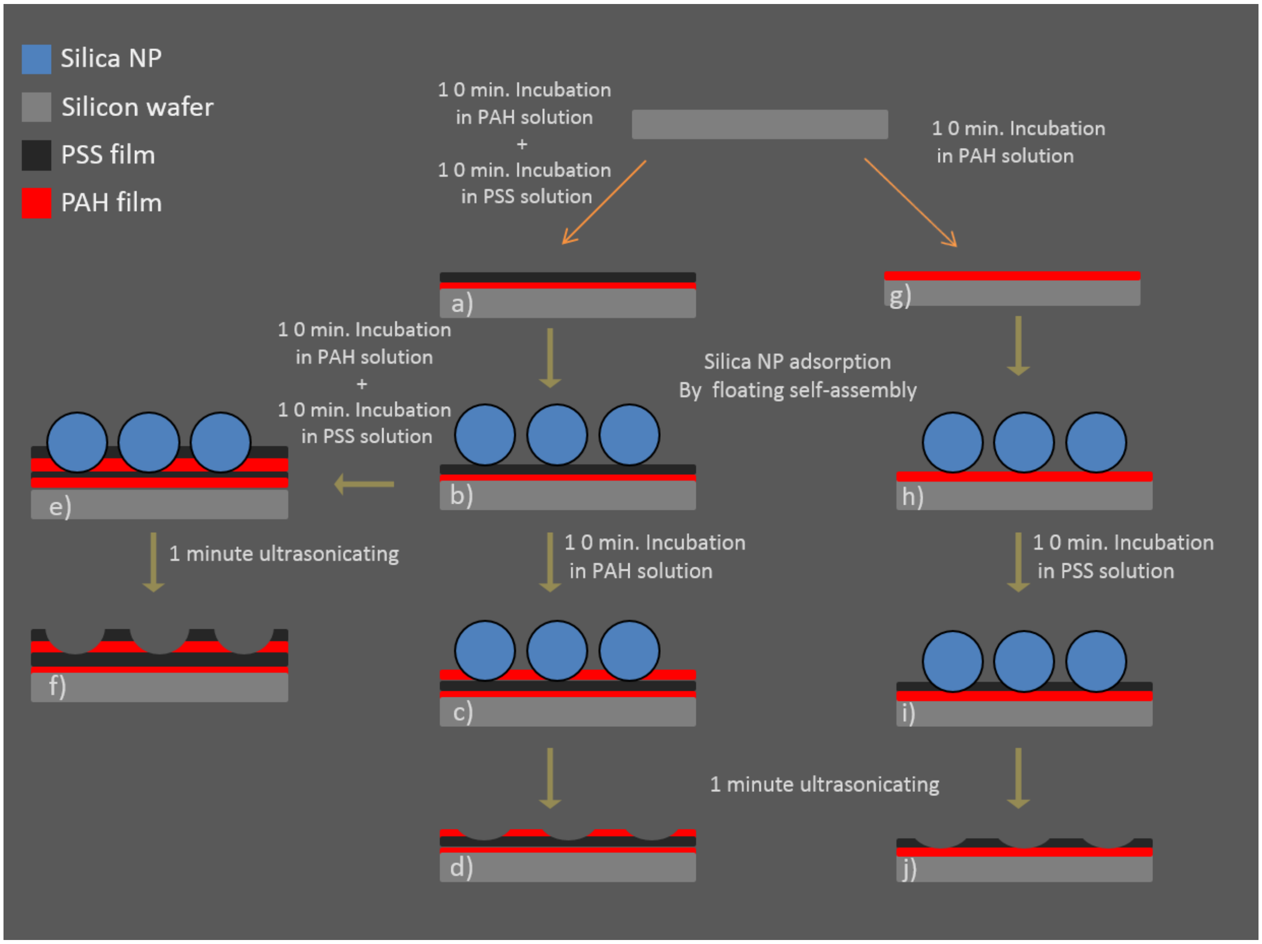

Figure 4.21: Schematic representation of synthesis routes for honeycomb patterned polyelectrolyte thin films with different charge designs.

In Figure 4.22 some of the possible charge designs of honeycomb structures are shown in top view. By altering initial surface charge, number of deposited layers and final surface charge, a variety of charge designs has been fabricated. To identify these charge designs under SEM and AFM, negatively charged gold nanoparticles were used. Site selective deposition of gold nanoparticles resulting in particle arrays with different geometries directly indicate the charge designs of the polyelectrolyte films. This technique will be discussed in detail later under the title of “directed self-assembly of gold nanoparticles”.

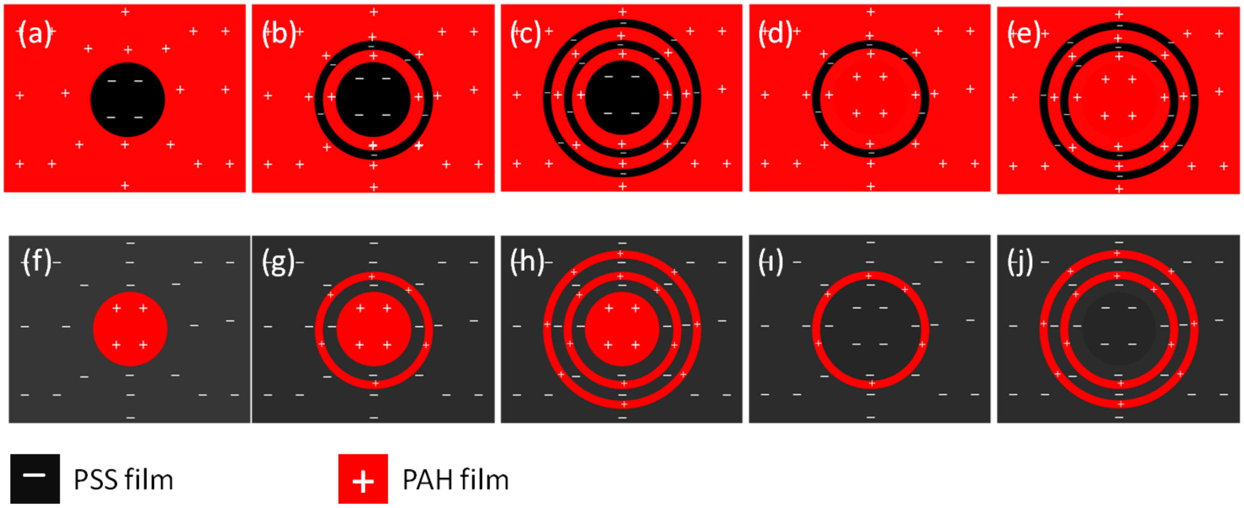

Figure 4.22: Schematic representation showing possible charge designs of honeycomb patterned polyelectrolyte thin films in top view.

It is also possible to change the depth and diameter of the honeycomb pores by changing the number of deposited polyelectrolyte layers. To comprehend the geometry of honeycomb pores the bottom and the top diameter should be considered. Bottom diameter (d_1) is a function of the radius of the silica nanoparticle (R) and the single layer thickness (h). The top diameter (d_n) is a function of R, h and the number layers (n). In the scope of this thesis h is considered same for both PAH and PSS layer according to ellipsometry measurements. Figure 4.23 shows the relationship between R, h, n and d_n. Equation 4.1 provides the diameter of the pore at a certain polyelectrolyte layer. Equation 4.2 is derived from equation 4.1 by dividing d_1 by d_n and simplifying it by using the assumption of h<<R, which is giving the ratio of top and bottom diameters of the honeycomb pore. This ratio is providing a 3 dimensional understanding of the pore structure. Equation 4.3 was obtained by dividing dn to depth of the pore (nh) and simplifying it by using again the assumption of h<<R, which is giving the ratio of top diameter (dn) to depth of the pore (nh). The conversion of narrow and deep pore structures to shallow and wide pore structures can be designed under the light of this equation. To fabricate narrower and deeper designs, smaller mask particles with thicker polyelectrolyte types should be chosen and for the wider and shallower designs bigger mask particles and thinner polyelectrolyte types should be chosen.

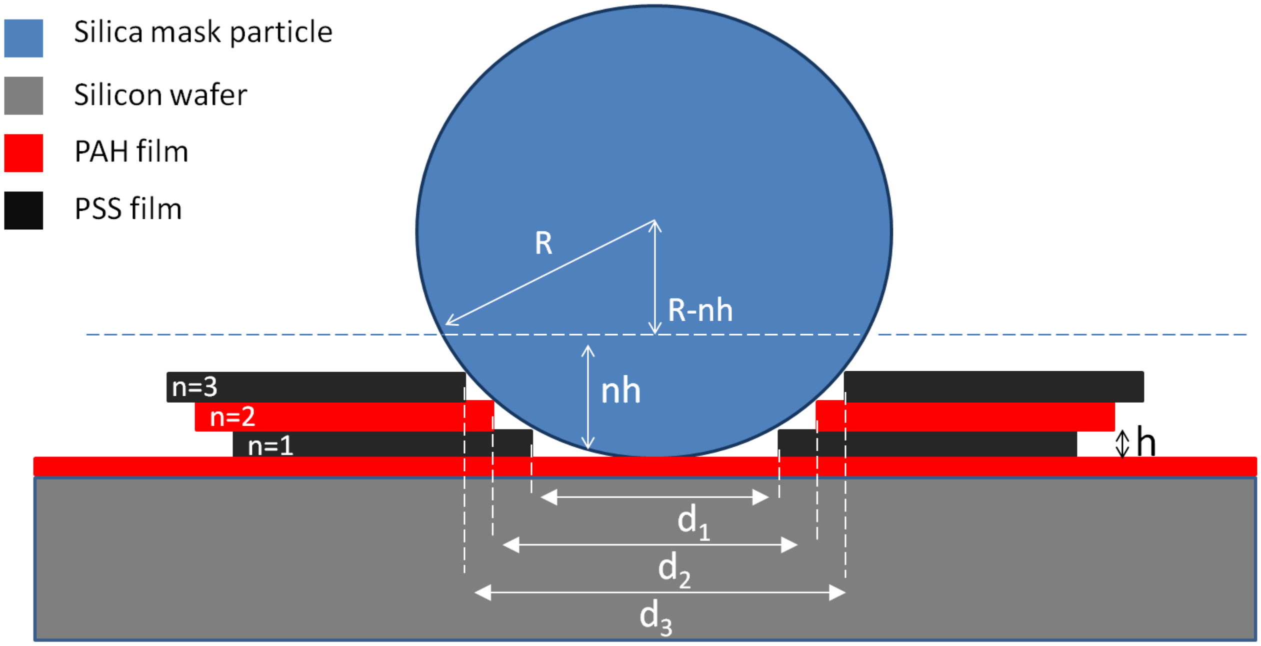

Figure 4.23: Schematic representation showing the relation between pore diameters of the honeycomb patterns with respect to mask particle diameter, thickness of the single polyelectrolyte layer and the number of polyelectrolyte layers.

$$d_n = \sqrt{R^2 - (R - nh)^2} \times 2 \qquad \textit{(equation 4.1)}$$

$$\frac{d_n}{d_1} = \sqrt{n - \frac{n^2 h}{2R}} \qquad \textit{(equation 4.2)}$$

$$\frac{d_n}{h_n} = \sqrt{\frac{8R}{nh} - 4} \qquad \textit{(equation 4.3)}$$

In Figure 4.24, the SEM image of a polyelectrolyte thin film with honeycomb-like structure is shown. The sample was produced by LBL deposition of 4 polyelectrolyte bilayers. After removal of the 500 nm silica mask particles very well ordered large scale honeycomb structures were produced. In this study we have successfully fabricated honeycomb structures having numbers of polyelectrolyte layers varying from 4 to 10.

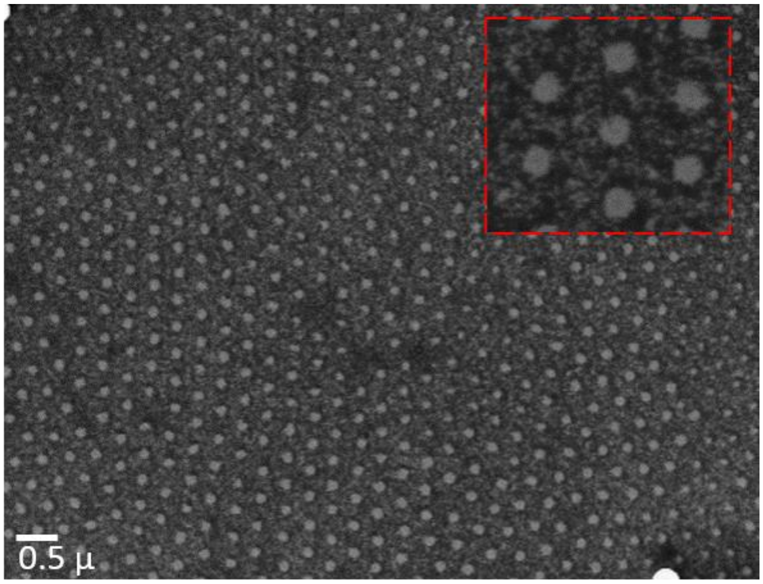

Figure 4.24: SEM image of a honeycomb patterned polyelectrolyte thin film produced by using 500 nm silica mask particles and deposition of 4 bilayers of polyelectrolyte.

The AFM analysis of the same sample is shown in Figure 4.25. The height profile of the pore indicates that the depth of the pore is around 8 nm which means each polyelectrolyte layer has thickness of approximately 1 nm. The height profile measurements by AFM correlates very well with ellipsometric measurements.

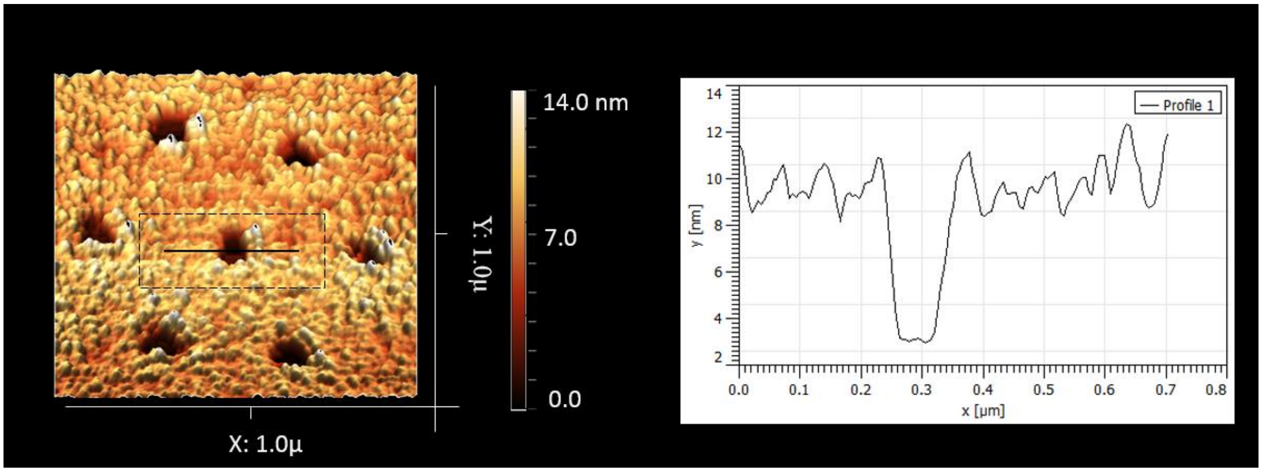

Figure 4.25: AFM image of a honeycomb patterned polyelectrolyte thin film produced by using 500 nm silica mask particles and deposition of 4 bilayers of polyelectrolyte.

In addition to electrostatic interactions, capillary forces play a significant role in the process of polyelectrolyte thin film construction. Together with the number of polyelectrolyte layers, capillary forces are determining the morphology. Due to the capillary forces, a water meniscus is forming in between the mask particle and the substrate. If the total thickness of the polyelectrolyte film is less than the height of the meniscus, honeycomb patterns do not form. In practical speaking, it can be concluded that to fabricate honeycomb patterns, at least three polyelectrolyte layers should be deposited on the substrate before removing the mask particles.

Synthesis of donut-like polyelectrolyte thin films

The main strategy to synthesize donut-like structures is shown in Figure 4.26. Silica particles were densely packed on silicon wafer substrates by the self-assembly floating technique. Depending on the intended final charge design the surface of the substrate was positively or negatively charged prior to particle adsorption. After silica particle adsorption, substrates were coated with one or two polyelectrolyte layers by LBL. After deposition of each polyelectrolyte layer, samples were washed twice for one minute. After removal of mask particles using ultrasonication, the donut like nano-patterns were obtained.

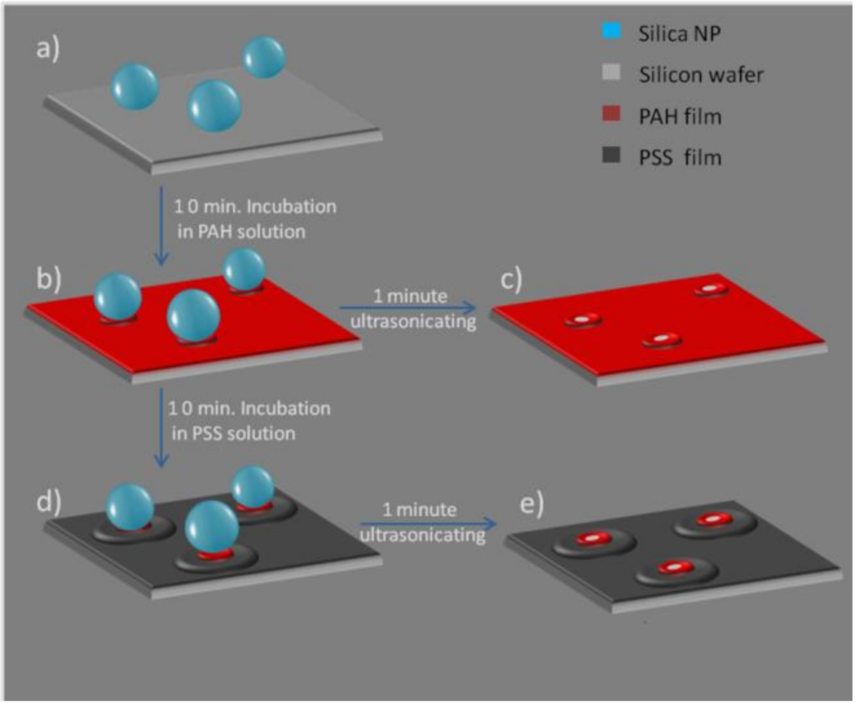

Figure 4.26: Schematic representation of general synthesis route for donut-like patterned polyelectrolyte thin films with different charge designs.

The most crucial parameter to synthesize donut-like patterns is the number of polyelectrolyte layers that are involved in the layer by layer deposition progress. Donut-like patterns can only form in case of deposition of less than 3 polyelectrolyte layers. The occurrence of donut-like pattern can be explained by meniscus formation in between the mask particle and the substrate. This phenomenon is sketched in Figure 4.27.

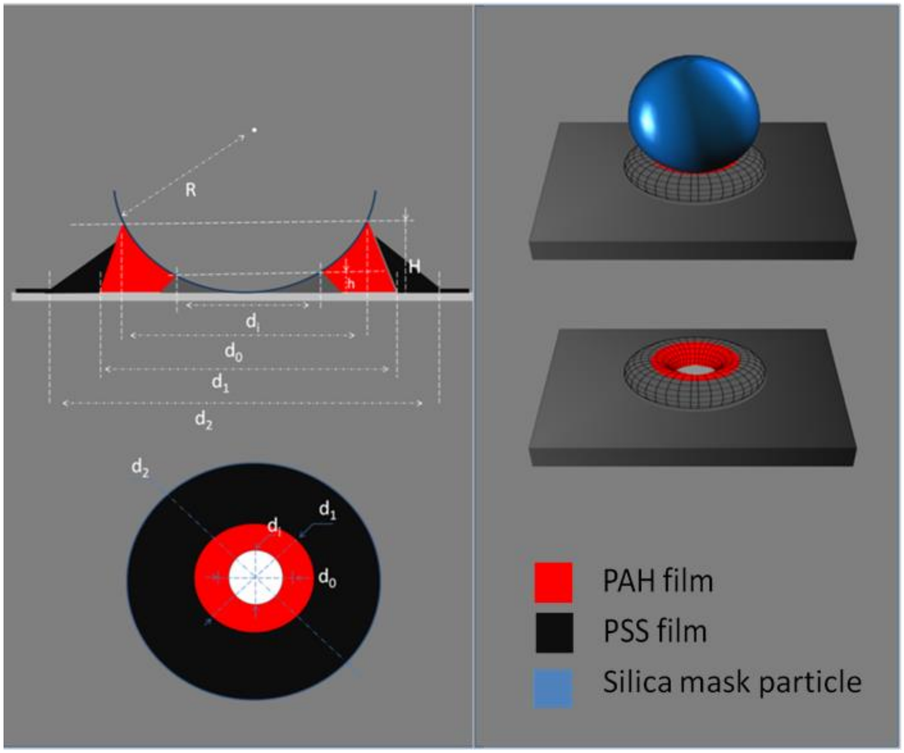

Figure 4.27: a) Schematic representation showing the relationship between the dimensions of donut-like patterns and mask particle diameter, thickness of the polyelectrolyte layer in the particle substrate interface (meniscus size) and the number of polyelectrolyte layers. b) 3D view of a donut like-pattern before and after mask particle removal.

It can be speculated that the polyelectrolyte solution in the meniscus yields thicker layers while it is drying. The height difference of the polyelectrolyte layer between the particle-substrate interface and the substrate surface causes donut-like patterns to be formed. By altering the order of the polyelectrolyte layers, the charge design of donut patterns can be reversed effectively. In Figure 4.28 an SEM image of a donut-like pattern is shown. In this sample the donut pattern was synthesized by adsorbing mask particles on a negatively charged silicon wafer, coating it with a PAH+PSS bilayer and removing the mask particles. In SEM image it can be seen that the donut patterns are uniform and well ordered.

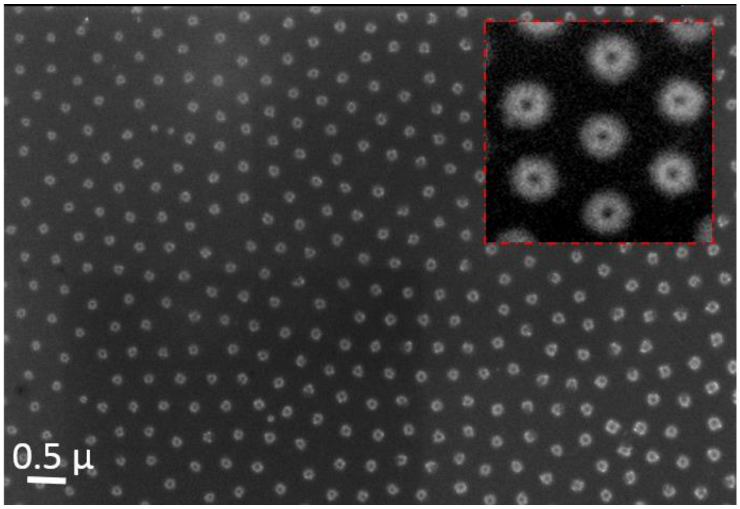

Figure 4.28: SEM image of donut-like patterned polyelectrolyte thin film produced by using 500 nm silica mask particles and deposition of 1 bilayer of polyelectrolyte.

In Figure 4.29 the AFM image of the donut-like pattern is shown. The height profile indicates that the approximate thickness of the donut-like pattern is around 2 nm and that the lateral parameters, d_0 and d_i, are 100 nm and 30 nm respectively. It has to be considered that the AFM tip used in the analysis has curve radius of 15 nm, which is in the same size regime as the center pore of the donut-like structure. This limits the accuracy of lateral size measurement of the center pore. The phenomenon is described in detail in **Figure 3.5**.

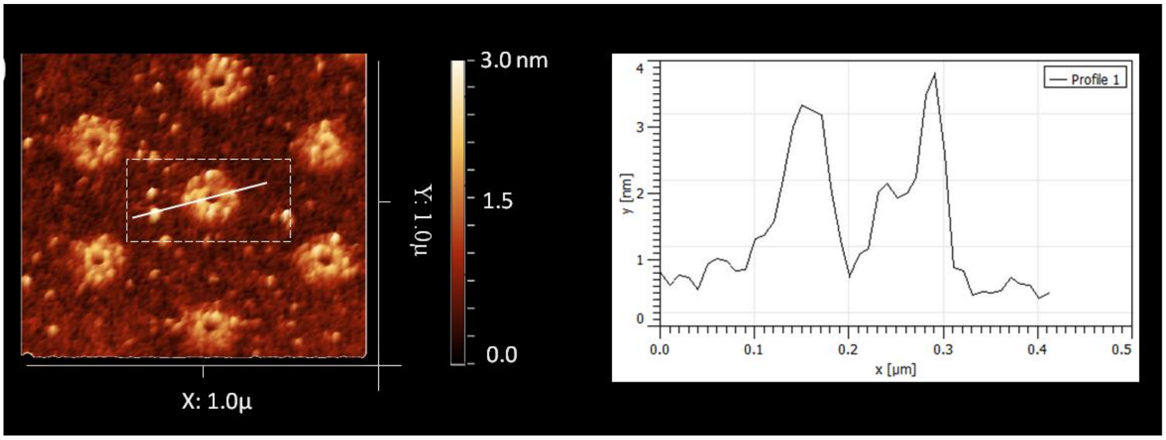

Figure 4.29: AFM image of donut-like patterned polyelectrolyte thin film produced by using 500 nm silica mask particles and deposition of 1 bilayer of polyelectrolyte.

4.1.3 Directed self-assembly of gold nanoparticles on charge heterogene-ous PE films

In this section we demonstrate a new and simple technique for the fabrication of several 2D and 3D metal nanoparticle arrays, such as with dot, grid, ring, out-of-ring, and circular patch geometries by using heterogeneously charged polyelectrolyte nanopatterns as templates which were discussed extensively in the previous section (4.1.2) of the thesis. By coating inter-metal nanoparticle areas with protein resistant polymers (e.g. PAA-PEG 2000) protein adsorption sites with complex geometries can be generated for specific protein adsorption. In this part of the thesis, we will focus on the synthesis of 2D and 3D metal nanoparticle arrays and their geometrical and dimensional variation.

Directed self-assembly of gold nanoparticles on nanopatterned polyelectrolyte templates is done by incubating honeycomb and donut-like patterned thin films with different charge designs in gold nanoparticle solution. Citrate capped, negatively charged gold nanoparticles were used as electrostatic interactions are assumed to be the driving force for their site selective deposition on the charged substrate. Thus, gold nanoparticles should be addressed to the PAH-derivatized areas of the film. In contrast, adsorption of gold nanoparticles on PSS-derivatized areas should be prevented by electrostatic repulsion. Site selective deposition of gold nanoparticles is investigated separately for honeycomb and donut-like patterns.

Site specific deposition of gold nanoparticles on honeycomb patterns

As discussed in section 4.1.2.3 and presented in Figures 4.21 4.22, a variety of different charge designs on honeycomb patterns has been obtained by altering the order and the number of deposited polyelectrolyte layers. Three main strategies were used to generate different gold nanoparticle arrays with honeycomb patterns. These strategies are shown in Figure 4.30.

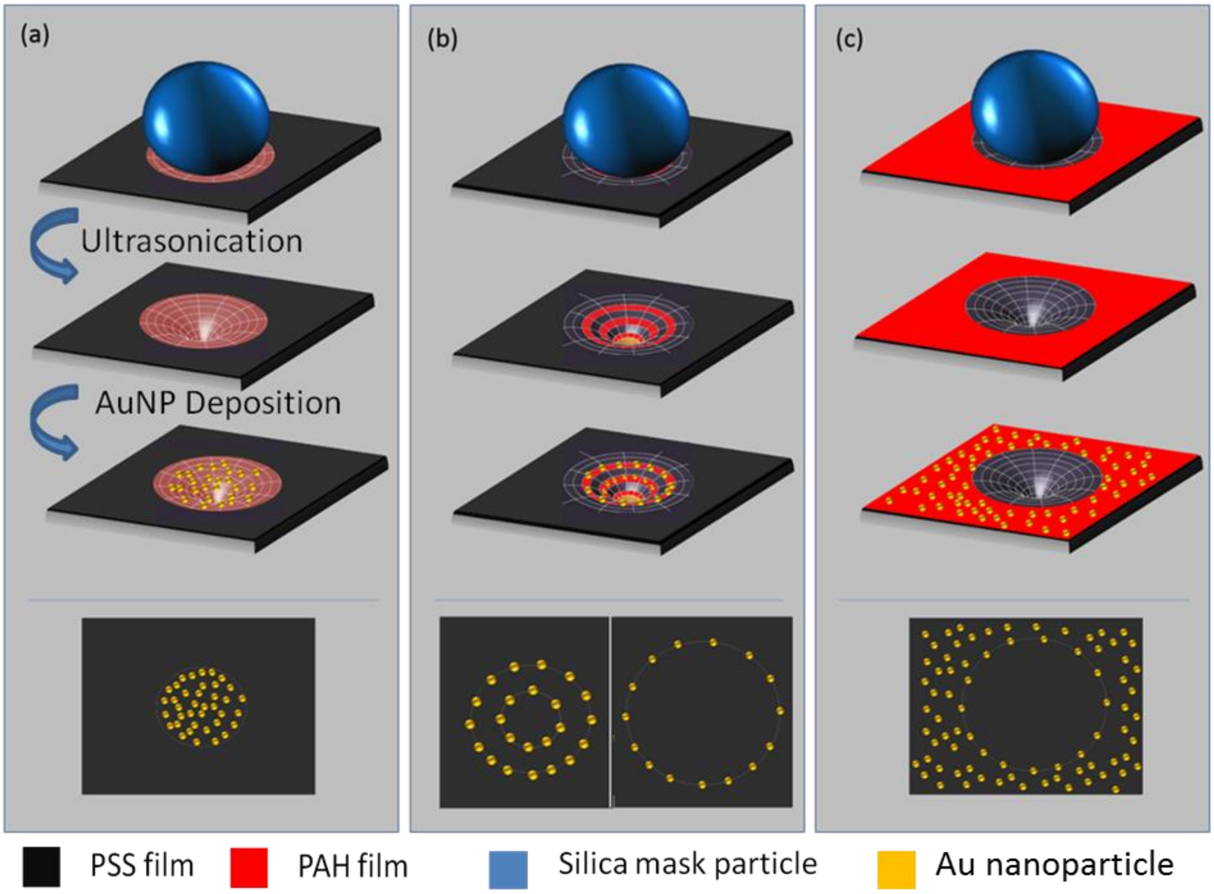

Figure 4.30: Schematic representation of 3 different strategies to fabricate, different metal arrays: a) circular patch, b) ring and multi-ring, and c) grid.

The first strategy was, addressing the gold nanoparticles into the pores by using a charge design where the base of the pore is positively charged and the rest of the thin film matrix was negatively charged. This strategy resulted in the formation of circular-patch particle geometries. The second strategy was to addressing gold nanoparticles to the side walls of the pores by using a charge design where the base of the pore and the thin film matrix in between the pores are negatively charged. This strategy resulted in ring or multi-ring particle array formation depending on the number of layers used in the LBL progress to construct the pattern. The third strategy was to address the gold nanoparticles only to the thin film matrix in between the pores by choosing a charge design where only the pore base is negatively charged. This strategy resulted in grid particle array formation.

Figure 4.31 shows SEM images of the four possible nanoparticle array geometries on honeycomb patterns.

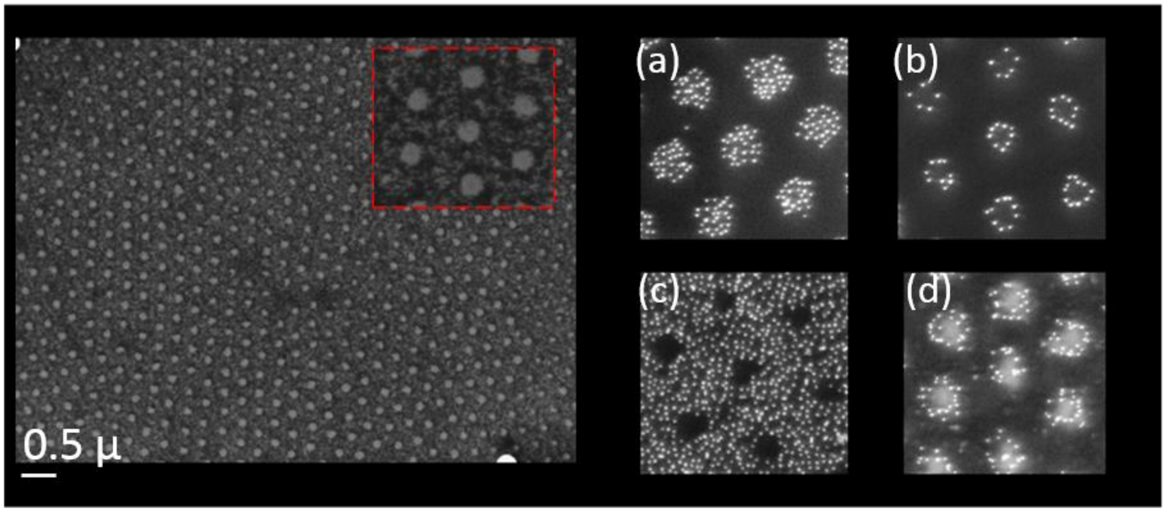

Figure 4.31: SEM images of honeycomb patterns with different metal arrays a) circular patch, b) ring, c) grid and d) multi-ring.

The density of the gold nanoparticles on PAH layers was changed by changing the incubation time of the patterned polyelectrolyte films in gold nanoparticle solution. SEM image of grid nanoparticle arrays with changing density of gold nanoparticles is shown in Figure 4.32.

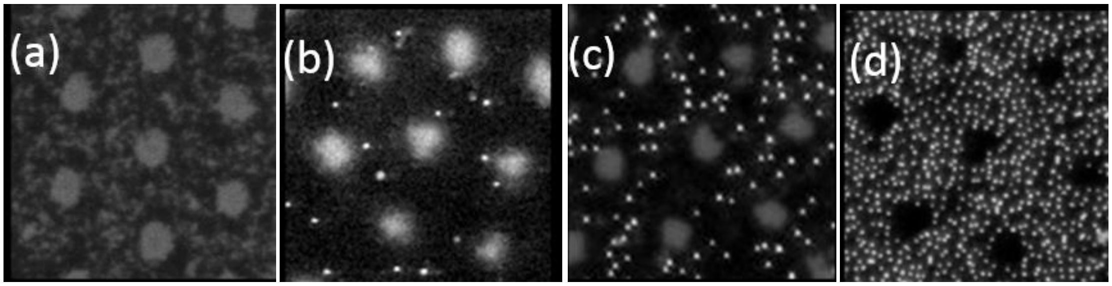

Figure 4.32: SEM pictures of honeycomb polyelectrolyte patterns prepared for grid structure incubated in 15nm gold nanoparticle solution for different times: a) 0, b) 5, c) 20, and d) 120 min.

Gold nanoparticles can be selectively adsorbed onto the structured surface before or after silica mask particle removal. By altering the number of deposited polyelectrolyte layers and the sequence of mask particle removal and gold nanoparticle adsorption steps it is possible to change the dimensions of the grid nanoparticle arrays. In Figure 4.33, corresponding SEM images are shown.

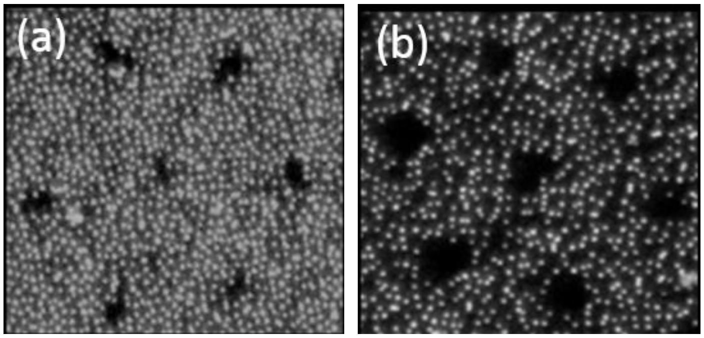

Figure 4.33: SEM image of a honeycomb patterned polyelectrolyte thin film produced by using 500 nm silica mask particles and deposition of a) 2 bilayers of polyelectrolyte (gold nanoparticles were adsorbed after mask particle removal) and b) 4 bilayers of polyelectrolyte (gold nanoparticles were adsorbed before mask particle removal).

Site specific deposition of gold nanoparticles on donut-like patterns

By choosing the appropriate charge design for donut-like patterns, the two possible types of gold nanoparticle arrays have been fabricated. These are the ring and out-of-ring patterns, which are the negative structures of each other. Moreover, tuning the density of the gold nanoparticles in these arrays, hexagonal single dot nanoparticle orientations were also obtained. In Figure 4.34 the two routes for generating ring and out-of ring structures are presented.

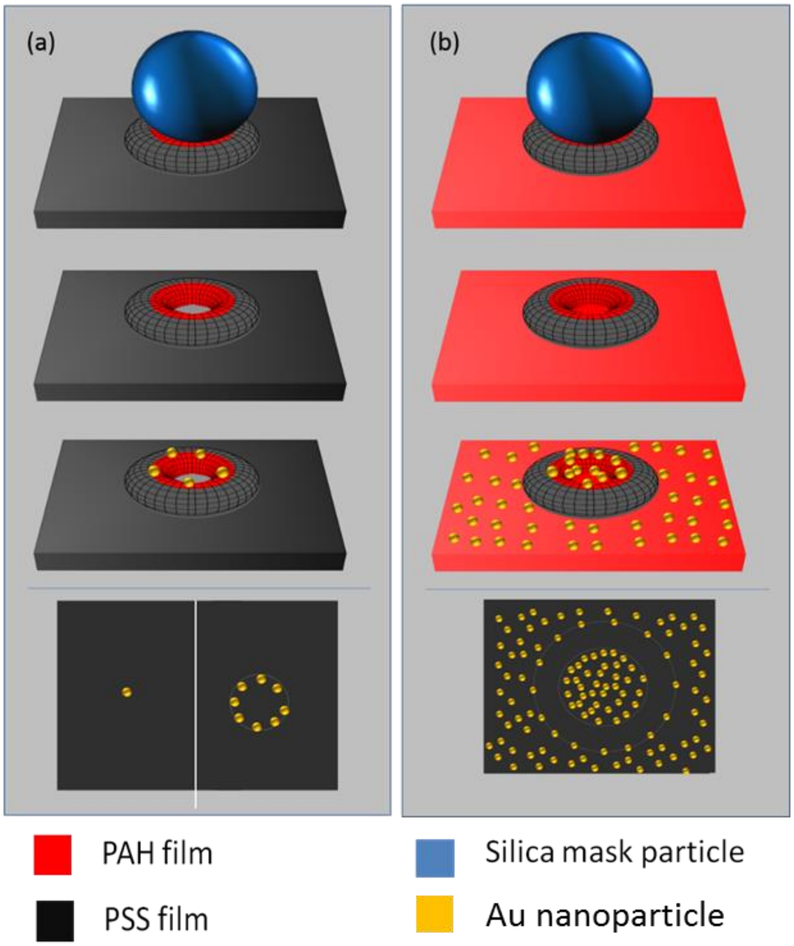

Figure 4.34: Schematic representation of 2 different strategies to fabricate different metal arrays: a) single dot and ring, and b) out-of-ring structures.

SEM images of ring, out-of-ring, and single dot gold nanoparticle arrays are shown in Figure 4.35. The same charge patterns were used to fabricate the samples in Figure (a), (b) and (d). Changing the incubation time in the gold nanoparticle solution converted the structures from single dot to ring array. In Figure (c) an out-of-ring particle array is shown. It is the negative image of Figure (d) and obtained by reversing the charge design of the patterns by changing the order of polyelectrolytes in LBL deposition process.

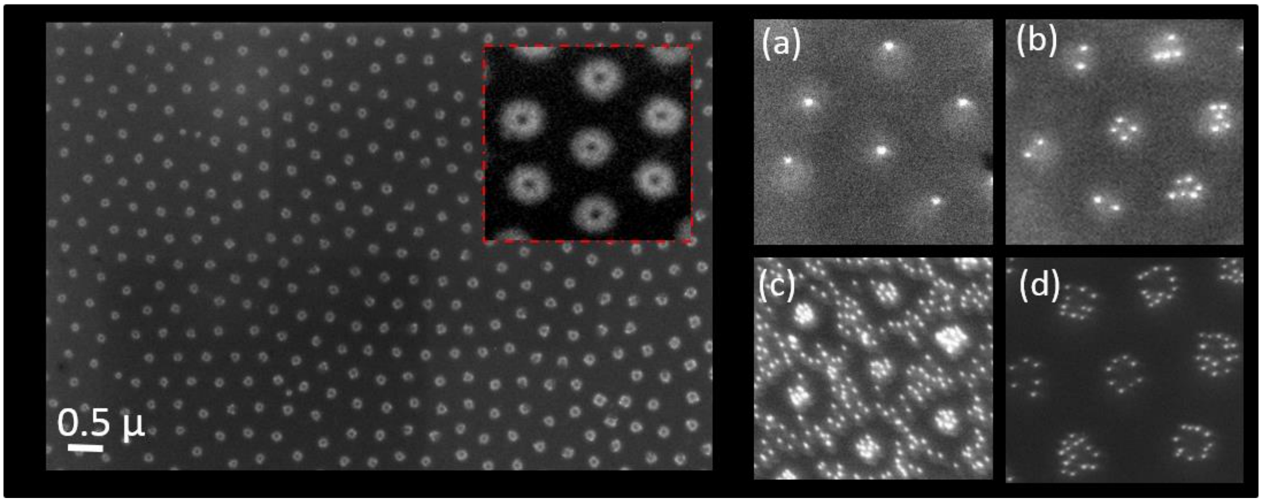

Figure 4.35: SEM images of donut-like patterns with different metal arrays a) single-dot, b) multi-dot, c) out-of-ring, and d) ring.

In Figure 4.36, AFM images of gold nanoparticles site selectively deposited on donut like patterns are shown. The image with higher magnification, (a), clearly shows the donut pattern and the orientation of the gold nanoparticles. In this sample, particles were only deposited on the torus structure of donut-like patterns. The image with lower magnification, (b), shows that there is no unspecific adsorption of gold nanoparticles in between the donut-like patterns. This image also proves the well-ordered hexagonal structure of ring arrays. The height profile analysis shows that the thickness of the donut pattern is only about 1-2 nm. However, this ultrathin film is able to create enough electrostatic force to selectively attract 15 nm gold nanoparticles.

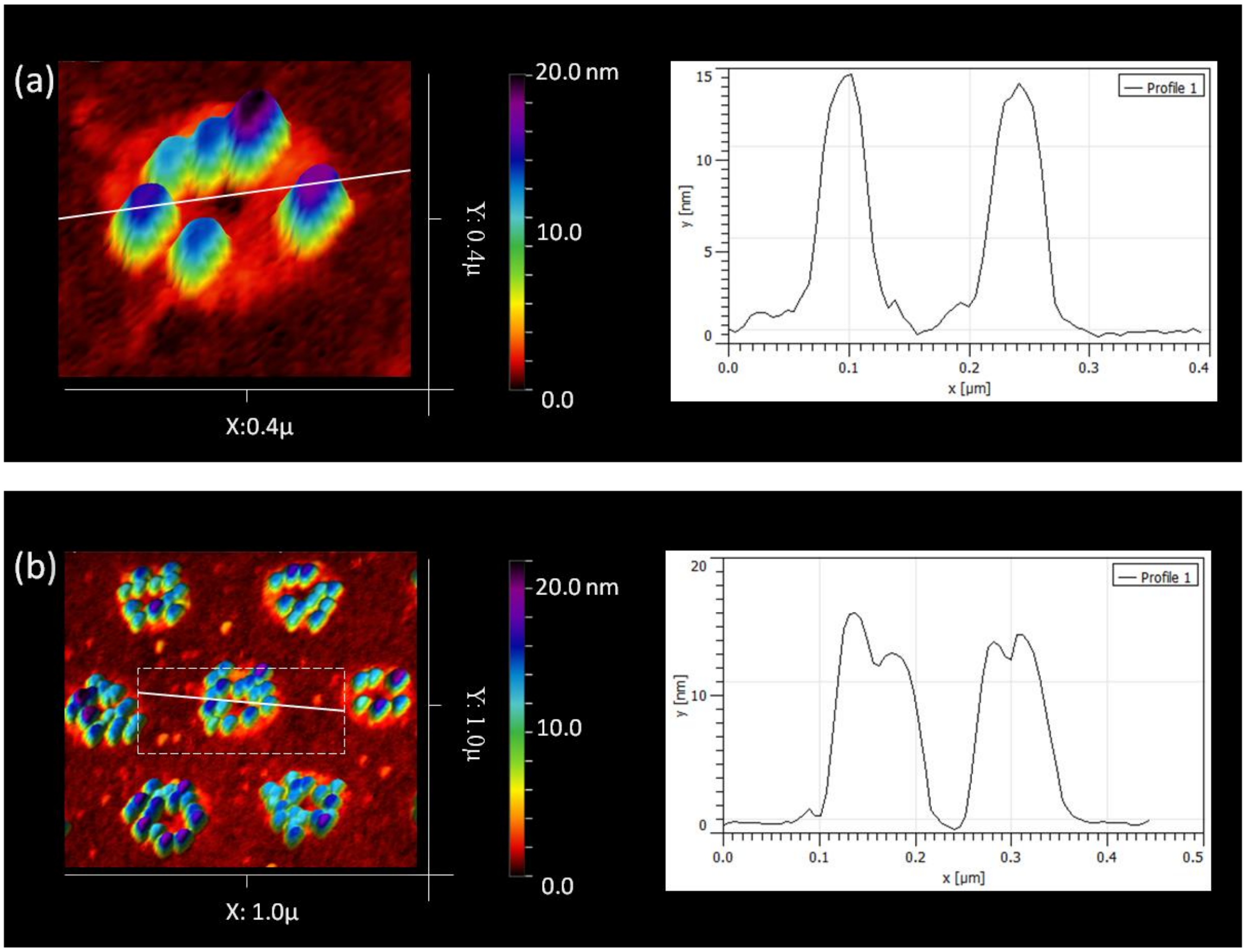

Figure 4.36: AFM image showing selective deposition of gold nanoparticles on donut-like patterned polyelectrolyte thin films produced by using 500 nm silica mask particles and deposition of 1 bilayer of polyelectrolyte.

4.1.4 Synthesis of metal-dielectric hybrid nanopatterns for site specific protein adsorption

In literature, studies have shown that the topography of adsorptions sites may have a strong influence on conformation of proteins [86, 101, 102]. If the topography of an adsorption site is not suitable for the particular protein, the protein will unfold and denature. Previous studies in our research group on GOx adsorption on 11-40 nm spherical gold nanoparticles proved that the curved surface of gold nanoparticles causes GOx to unfold and lose its activity. Considering this fact, we have tried to find a solution to decrease the curvature of the particles without enlarging the adsorption site dimensions. To do this we decided to use the upper spherical sector of a gold nanoparticle as an adsorption site. We assumed that if the angle of the sector is small enough, the surface will behave as if it is flat and prevent our model enzyme GOx from denaturation (Figure 4.37).

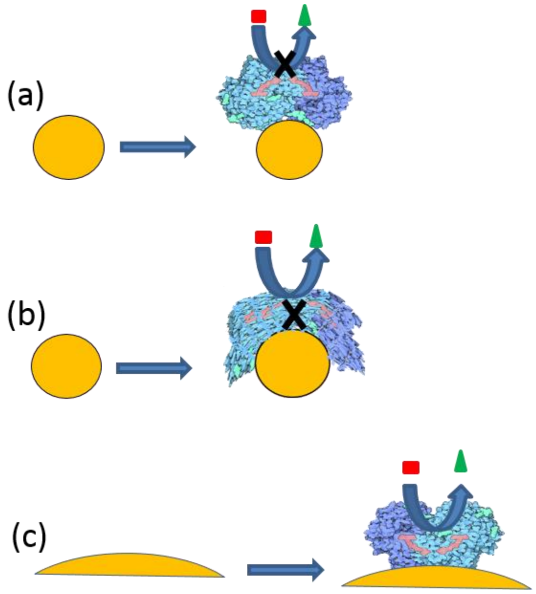

Figure 4.37: Schematic representation showing the model enzyme GOx on a) and b) a spherical gold nanoparticle with loss of enzymatic activity, and c) an almost flat sector of a sphere without loss of activity.

The approach presented in this section is based on partially embedding randomly closed packed monolayers of monodisperse gold nanoparticles into a protein resistant polymer matrix by controlled PEGMA graft polymerization to generate nano-domains for site specific protein adsorption (Figure 4.38).

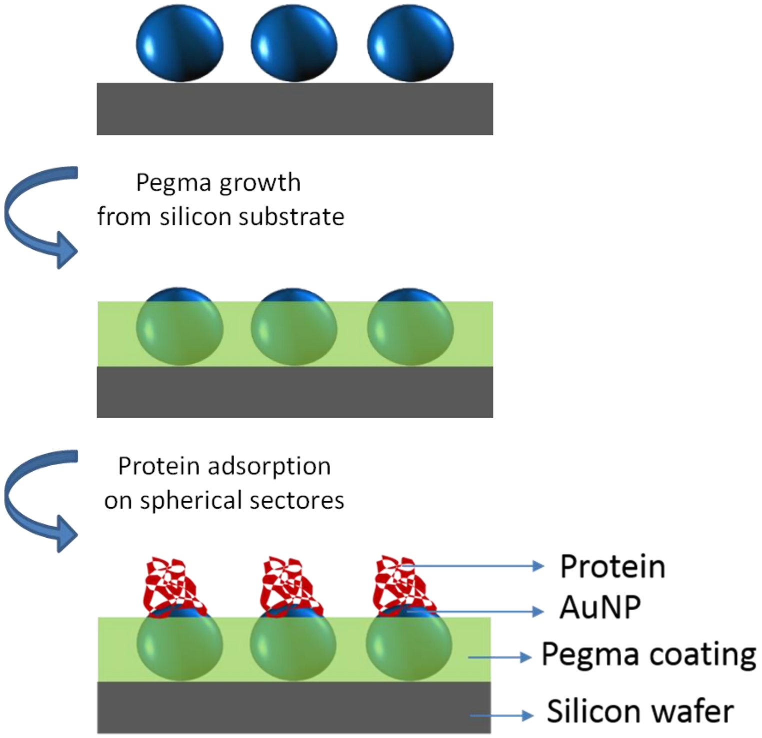

Figure 4.38: Schematic representation showing the preparation of nano-domains for site specific protein adsorption. Monolayers of gold nanoparticles were partially embedded into a protein resistant matrix by controlled PEGMA graft polymerization on a silicon surface. The non-embedded sectors of the particles constitute the adsorption sites.

By selecting nanoparticles with different diameter and changing the protein resistant matrix thickness, the lateral dimensions and the topography of the adsorption sites was intended to be tuned. The geometric relationship between protein resistant matrix thickness, gold nanoparticle diameter and the adsorption site diameter is shown in Figure 4.39.

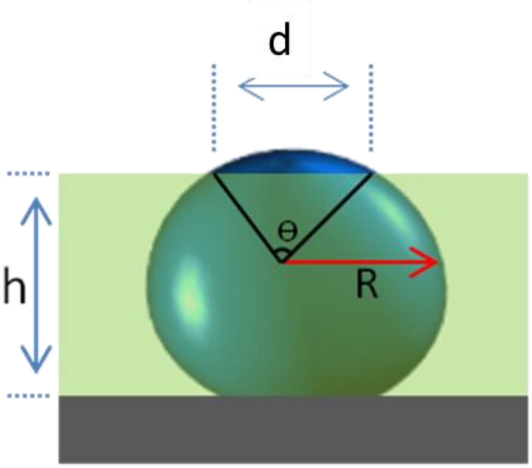

Figure 4.39: Schematic representation showing the relation between adsorption site diameter (d) with respect to gold nanoparticle radius (R), PEGMA layer thickness (h) and sector angle (ϴ).

Equation 4.4 states the mathematical relation between adsorption site diameter, polymer thickness and gold nanoparticle radius. With the help of this equation, the diameter of gold nanoparticles and the PEGMA layer thickness was decided on before starting synthesis of the structures.

$$\mathrm{d} = \sqrt{R^2 - (h-R)^2} \times 2$$

(Equation 4.4)

We decided to use gold nanoparticles with maximum diameter to obtain spherical caps with the smallest angle of curvature. The thickness of the polymer film must then be adjusted such that the area of the adsorption site corresponds to the size of the model protein. The maximum diameter of the gold nanoparticles that we were able to synthesize with reasonable size distribution was 80 nm. However, in this size regime gold nanoparticles tended to aggregate on silicon substrates instead of forming monolayers. To deposit them as monolayers, the density of the gold nanoparticles on substrate was decreased. To do this, two types of gold nanoparticle solutions were mixed to obtain the desired particle density on APTES coated silicon substrates. 80 nm gold nanoparticle solution and 15 nm gold nanoparticle solution were mixed in ratios of 1:1, 1:2 and 1:3 to deposit 80 nm gold nanoparticles as a monolayer by changing particle densities (Figure 4.40).

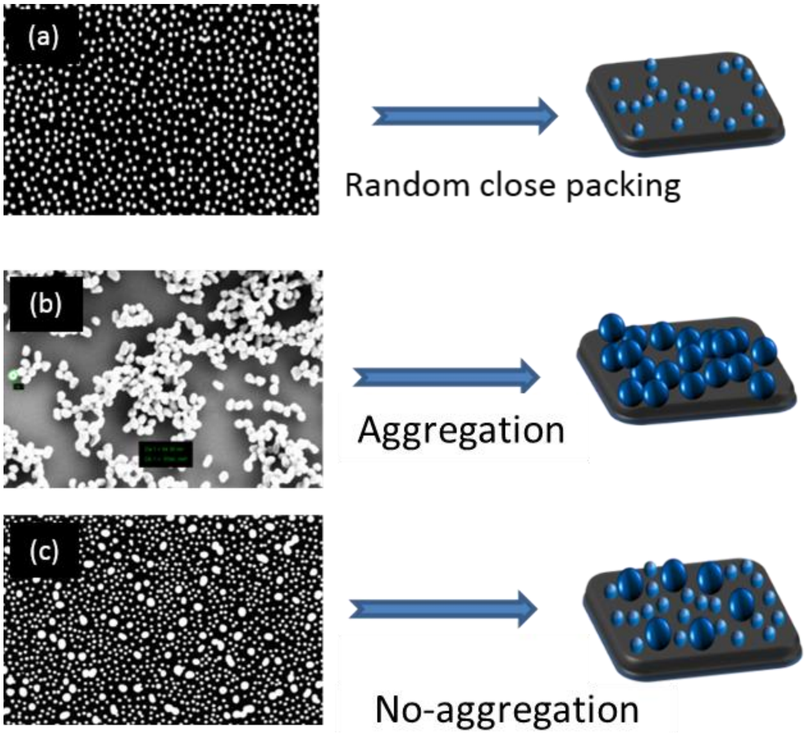

Figure 4.40: SEM images of gold nanoparticles on APTES coated silicon substrates with diameters of a) 15 nm, b) 80 nm and c) 15 and 80 nm.

The aim of this study was to fabricate adsorption sites in the size regime of 20-40 nm. To approach this size range by the synthesis method described above, 60 and 80 nm gold nanoparticles were used. The PEGMA layer thickness was calculated by equation 4.4 to obtain adsorption sites with the desired diameter. PEGMA graft polymerization was started from BIBB functionalized silicon substrates as described in section 3.1. The PEGMA thickness was directly dependent on the reaction time and the concentration of PEGMA. By selecting these two parameters properly, the intended PEGMA thicknesses were tried to be obtained. To generate 20-40 nm sized adsorption sites, the thickness of the PEGMA layer coating was decided to be in the range of 70-75 nm and 50-55 nm on 80 nm and 60 nm particles, respectively.

To fabricate the nanopatterns for protein adsorption as depicted in Figure 4.38, negatively charged gold nanoparticles with a diameter of 60 and 80 nm were synthesized as described in section 3.3.1. Next they were deposited as a monolayer on APTES coated silicon substrates. Afterwards the surface was functionalized with the initiator molecule BIBB. The functionalized substrates were analyzed under SEM to check whether there are any BIBB or APTES aggregates on substrate surface before starting PEGMA polymerization. Then the controlled PEGMA graft polymerization was started under inert atmosphere by immersing functionalized substrates into the reaction mixture. The reaction was carried out under nitrogen atmosphere because of the oxygen sensitivity of the reaction due to the susceptible nature of copper(I) bromide (reaction catalyst) with respect to oxidation. PEGMA polymerization was terminated after the planned reaction time by taking out the samples from reaction the solution with proper washing.

To obtain the intended PEGMA thickness to partially embed the gold nanoparticles, the appropriate PEGMA concentration and reaction duration were determined. This was done by measuring the average thicknesses of PEGMA layers which were prepared with different reaction parameters. Table 4.4 shows the thickness values obtained for different reaction parameters. The ellipsometric measurements, performed at different parts of the substrates, showed that the PEGMA thickness was varied approximately 10-15 % over the substrate. Also the average PEGMA thicknesses for the samples synthesized under the same reaction conditions were deviating from each other by approximately 20-30%.

PEGMA concentration	**Reaction Time**	**PEGMA Thickness**
20% (v/v)	10 h	35 ± 11 nm
33% (v/v)	10 h	52 ± 14 nm
45% (v/v)	10 h	61 ± 7 nm

20% (v/v)	15 h	48 ± 8 nm
33% (v/v)	15 h	75 ± 10 nm
45% (v/v)	15 h	81 ±16 nm
20% (v/v)	20 h	55 ± 13 nm
33% (v/v)	20 h	89 ± 11 nm
45% (v/v)	20 h	94 ± 17 nm

Table 4.4: PEGMA coating thickness on silicon substrates as a function of reaction time and PEGMA concentration. Thickness measurements were done by ellipsometry.

Ellipsometry measurements were also performed to determine the BIBB coating thickness. The average thickness values of APTES coated and APTES+BIBB coated substrates are shown in Table 4.5. The average BIBB layer thickness was determined as 3 nm.

Surface Functionalization	**Film Thickness (Å)**
Si+APTES	23 ± 3
Si+APTES+BIBB	52 ± 6

Table 4.5: Ellipsometric thickness measurements of APTES and APTES+BIBB films on silicon substrates.

According to Table 4.4, 10 to 12 h reaction time and 33% (v/v) PEGMA concentration were selected as experimental parameters to embed 60 nm gold nanoparticles. For 80 nm gold nanoparticles, 14 to 16 h reaction time and 33% (v/v) PEGMA concentration were chosen.

In Figure 4.41, SEM images of the gold nanoparticles embedded into a PEGMA matrix are shown. The sample was scratched intentionally to show the PEGMA coating (corresponding dark layer in Figure 5.39 (a)) together with gold nanoparticles.

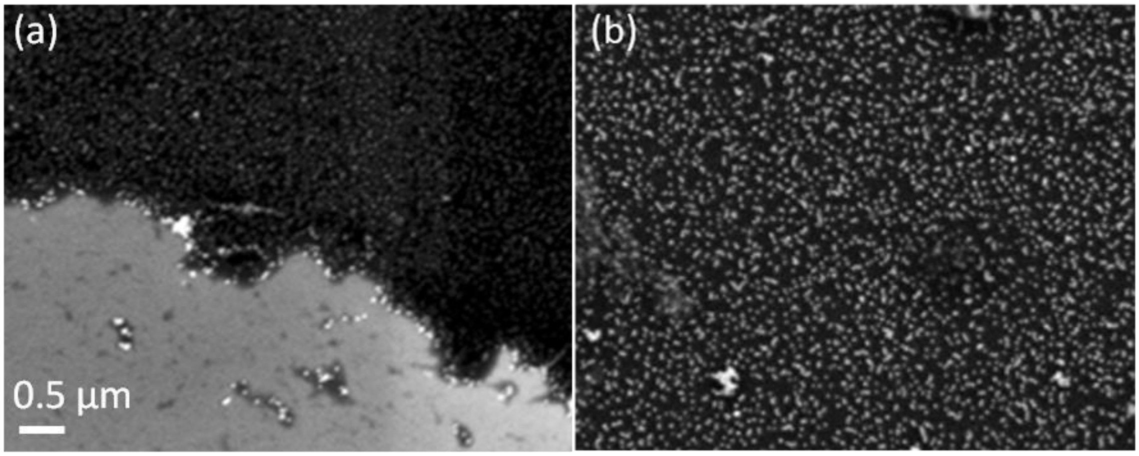

Figure 4.41: SEM images showing gold nanoparticles with 60 nm diameter partially embedded into a PEGMA matrix.

In Figure 4.42, the AFM image of partially embedded gold nanoparticles with 60 nm diameter are shown. The average diameter of the sphere sectors was intended to be 30 nm. To achieve this, the desired PEGMA thickness was calculated as approximately 50 nm by subtracting the height of the corresponding sphere sector from the particle diameter. The AFM image was indicated that PEGMA coating is not homogenous as expected, resulting non homogeneous size distribution of adsorption sites (sphere sectors).

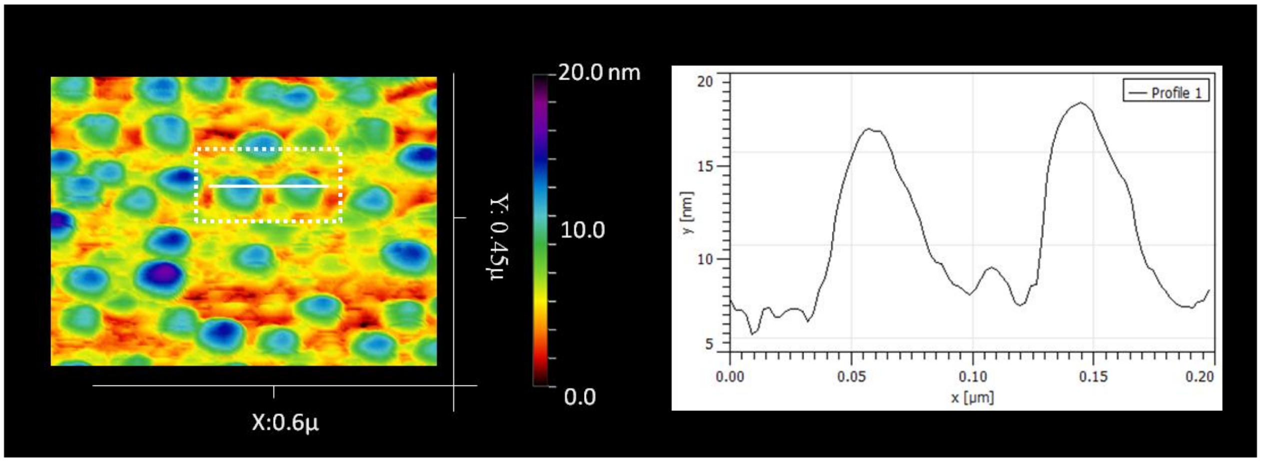

Figure 4.42: AFM image showing 60 nm gold nanoparticles embedded into a PEGMA matrix with 50-55 nm thickness

The limited reproducibility of PEGMA layers with precise thickness negatively affected the yield of the nanopatterns produced. Even though we were able to partially embed gold nanoparticles into the protein resistant matrix as proposed, the poor control over the PEGMA thickness drastically decreased the success of generating adsorption sites with a narrow size distribution. Nevertheless, the results of this study can be considered as reasonable proof-of-principle experiments for further studies.

4.1.5 Synthesis of nanopatterned OEG-silane films for site specific protein adsorption

In this section we demonstrate a bottom up and generally applicable technique to fabricate nanopatterned structures for site specific protein adsorption by employing deposition of OEG-silane monolayers and colloidal lithography. 2-[methoxy(polyethylenoxy)propyl]trichlorosilane was used as protein resistant OEG-silane and amine terminated dielectric silica particles were used as colloidal mask particles to construct the nano-patterned structures. Some of the results which are shown in this section were obtained together with Christine Dietrich in context of her master studies [103]. She also made significant contributions to the optimization of the technique discussed in this paragraph.

In literature, there many studies exist on nanopatterning with silane monolayers and colloidal lithography [60, 75, 104, 105]. In this work we have tried to fabricate nanopatterns using patterning methods analogous to previous works in literature by employing a different silane molecule. By intentionally choosing 2-[methoxy (polyethylenoxy) propyl] trichlorosilane, the protein resistivity of the silane film was expected to be obtained due to the long ethylene glycol chain of the molecule.

With this fabrication technique adsorption sites for specific protein adsorption with tunable dimensions and topography were generated. The silanization process was performed by two techniques: chemical vapor deposition and deposition from solution. The sustainability of these techniques for large scale production was investigated and tried to be optimized. Reaction temperature, duration, pressure and humidity showed significant impact on structure uniformity and yield. The samples were characterized by XPS, ellipsometry, SEM and AFM.

OEG-silane coating by chemical vapor deposition

In Figure 4.43, a schematic representation of nanostructured surface preparation by chemical vapor deposition is shown. Silica nanoparticles with 500 diameter were deposited on silicon substrates by the self-assembly floating technique. Then substrates were coated a with OEG-silane monolayer by chemical vapor deposition (CVD) in a desiccator at low pressure conditions (10-50 mbars as discussed in section 3.4.1). The removal of silica mask particles by ultrasonic cleaning after OEG-silane coating lead to the formation of porous patterns for protein adsorption.

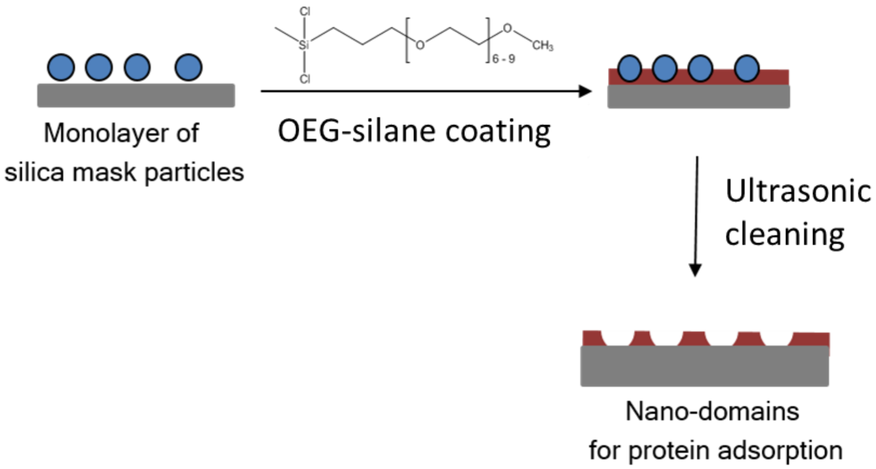

Figure 4.43: Preparation of patterned OEG-silane films by colloidal lithography. Surface areas which are covered with particles become protein adsorption sites after removal of the nanoparticles.

Assuming that the silane molecules used in these experiments only form monolayers, the dimension of the generated adsorption site only depends on the diameter of the mask particle. The equation 4.5 yields the adsorption site diameter, x, as a function of the mask particle radius, r, and the OEG-silane layer thickness, d (Figure 4.44).

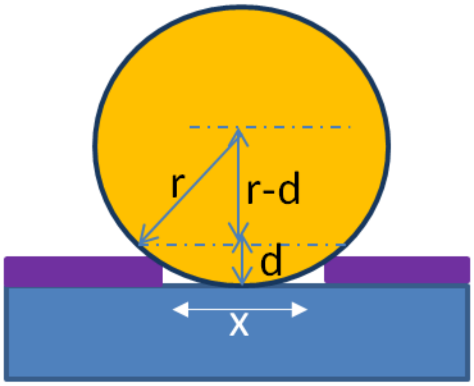

Figure 4.44: Sketch showing the relationship between adsorption the site diameter (x), the silica nanoparticle radius (r), and the OEG-silane layer thickness (d).

$$x=\sqrt{r^2-(r-d)^2}\times 2$$

(Equation 4.5)

The main challenge of this technique was reproducibility and sustainability to synthesize nanostructures with the same dimensional parameters. Since the silanization reaction is very sensitive in order to humidity, reaction temperature and the pressure, non-optimized parameters resulted in uncontrolled polycondensation or lack of OEG-silane layer formation on the substrates. By XPS and ellipsometry the presence of the OEG-silane monolayer, and by SEM and AFM the morphology and the dimensional details of the fabricated nanopatterns were analyzed.

Silicon substrates were exposed to UV light in order to remove any adsorbed organic compounds and most importantly activate the surface for the silanization reaction (Figure 4.45). Then the samples were silanized by CVD according to section 3.3.1. Several reaction temperatures (70, 80 and 90 ^{0}C) together with different reaction times (1, 2, 4, 8, and 16 hours) were used to determine the optimum chemical vapor deposition conditions. For each temperature and reaction time, three identical samples were fabricated to check the homogeneity and reproducibility of the OEG-silane monolayer and the uniformity of the nanostructures.

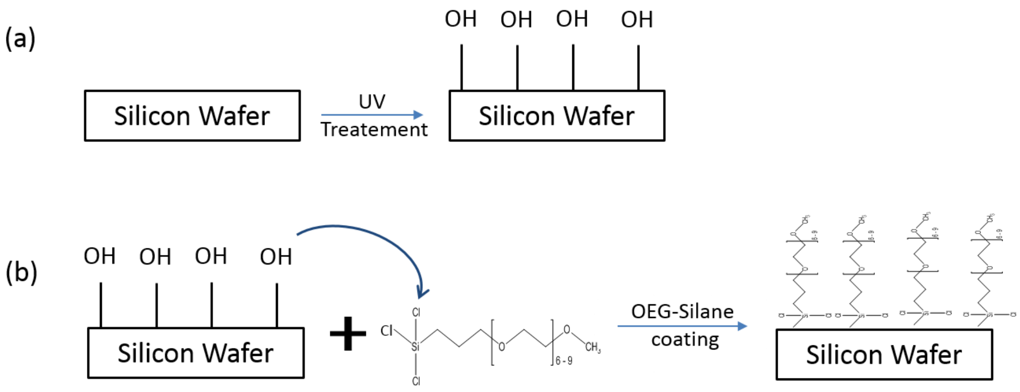

Figure 4.45: Schematic representation of a) surface activation of silicon wafers for the silanization reaction and b) OEG-silane monolayer formation on an activated silicon wafer.

To investigate the OEG-silane monolayer formation, the substrates were checked by SEM, XPS and ellipsometry. By SEM substrates were checked for any macroscopic residues remaining on the surface. Then the samples were analyzed by XPS to check for the intensity change in the C 1s, Si1s and O1s regions. Thickness measurements were done with ellipsometry at five different spots distributed all over the substrate to investigate the homogeneity of the OEG-silane monolayer and to determine the film thickness.

After analyzing the samples produced with different reaction parameters, 80 ^{0}C and 6 hours were found to be the optimum temperature and reaction time with respect to reproducibility and monolayer homogeneity. The following discussion refers to samples which were produced under such optimized conditions.

The XPS analysis of the OEG-silane coating on the bare silicon substrates is shown in Figure 4.46. Signal intensities of the Si1s, C1s and the O1s regions for the silane coated substrate and the reference sample (bare silicon wafer) are compared. The silanized sample has a higher signal intensity in the C 1s region due to long carbon chain of the silane molecule which was taken as an evidence for silane layer formation. The lower signal intensity in the Si region also indicates the presence of a silane as signal intensities from the substrate are shielded. In the O1s region the signal intensity was quite similar to the reference sample due to similar oxygen composition of the silicon substrate and the silane molecule.

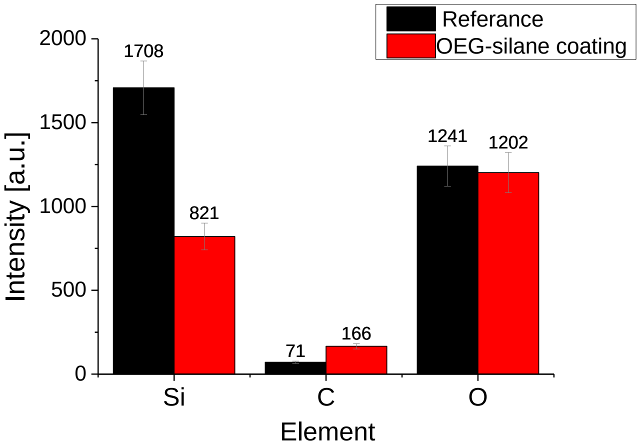

Figure 4.46: XPS analysis of the OEG-silane film on a silicon substrate. The silane coating was produced by chemical vapor deposition at 80 ^{0}C for 6 h.

In Figure 4.47 the SEM image of the patterned silane film is shown. It is clearly seen that hexagonally close-packed ring-like pores were produced. The black spots in the center of the rings are non-silanized areas (protein adsorption sites) which were blocked by the mask particles during the silanization process. The ring formation may be explained by polycondensation of silane molecules at the interface between mask particle and substrate due to water moieties. The SEM image indicates that the technique works quite fine to fabricate large scale nanopatterns for protein adsorption.

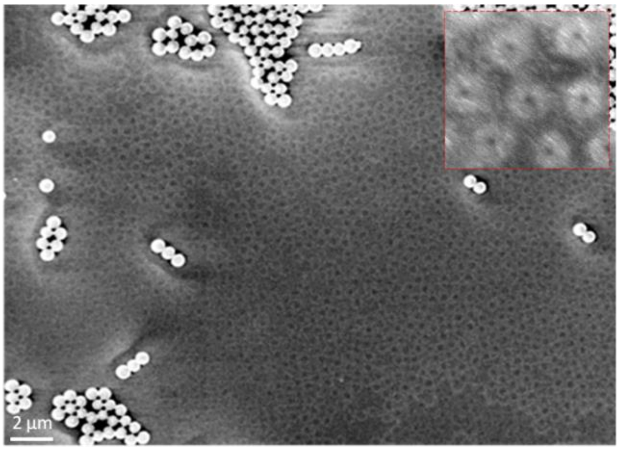

Figure 4.47: SEM image of a nanopatterned protein resistant silane films fabricated by chemical vapor deposition of 2-[methoxy(polyethylenoxy)propyl] trichlorosilane at 80 ^{0}C for 6 h. 500 nm mask particles were used.

The XPS analysis of patterned OEG-silane film is shown in the Figure 4.48. In the figure signal intensities of the Si 1s, C 1s and the O 1s regions for the silane coated substrate and the reference sample (bare silicon wafer) are compared. As expected the patterned silanized sample has a higher signal intensity in the C 1s region and a lower signal intensity in the Si 1s region. These observations were taken as an evidence for successful OEG-silane layer formation.

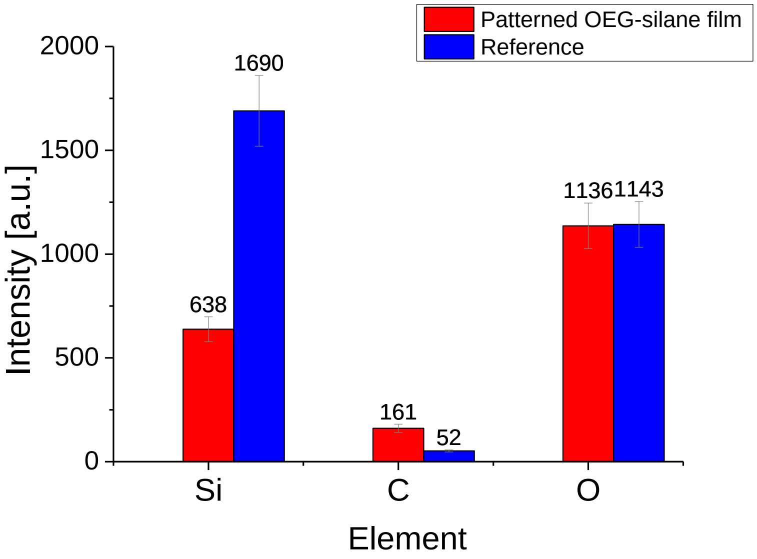

Figure 4.48: XPS analysis of a patterned OEG-silane film on a silicon substrate. The silane coating was produced by chemical vapor deposition at 80 ^{0}C for 6 h.

The ellipsometric thickness measurements showed that a homogeneous monolayer was formed by chemical vapor deposition. The thickness of the silane monolayer was determined as 1.5 nm for a non-patterned and 2.1 nm for the patterned silane layer. The higher thickness values measured for the patterned silane films in comparison to non-patterned silane films may be explained by polycondensation of silane molecules in the interface between mask particle and substrate due to water moieties. This will cause the formation of thicker silane layers at the walls of the pores.

OEG-silane coating by in solution deposition

Although chemical vapor deposition resulted in successful production of patterned OEG-silane films, it has several disadvantages. It requires a vacuum setup and undesirable polycondensation occurs frequently. In solution deposition

(ISD) was proposed as an alternative way for getting rid of these disadvantages. By using this alternative method, changes in the OEG-silane patterns were investigated. The same characterization techniques as in chemical vapor deposition were used to characterize the patterned OEG-silane films. The general mechanism for fabricating patterned OEG-silane films by the in solution deposition method was same as the CVD method and is depicted in Figures 4.43 and 4.44. Samples were prepared according to section 3.3.1 and the effect of reaction time and annealing of the substrate on patterning quality and the uniformity of the adsorption sites was analyzed. The results were compared with samples produced by chemical vapor deposition.

The XPS analyses of the OEG-silane coatings produced by chemical vapor deposition and in solution deposition were are in Figure 4.49. The signal intensities of the Si 1s, C 1s and the O 1s regions were compared. As expected the two patterned silanized samples have higher signal intensities in the C 1s region, and lower signal intensities in the Si 1s region. These were considered as an evidence for OEG-silane layer formation. On the other hand the sample prepared by in solution deposition showed a higher signal intensity in the C 1s region and a lower signal intensity in the Si 1s region. This may explained by more densely packing of OEG-silane molecules on substrate. The thickness of non-patterned OEG-silane layer produced by in solution deposition was measured 2.1 nm by ellipsometry. The silane layer was thicker when the samples were produced by in solution deposition method. The thickness of the non-patterned silane layer was 1,5 nm for the samples produced by chemical vapor deposition. This may also be explained by more densely packing of OEG silane molecules on substrate. It may speculated that the bending of the molecules are less when they are densely packed. And if they bend less, the average thickness of the monolayer has become higher. We can conclude that the ellipsometry measurements are correlating with XPS analyses.

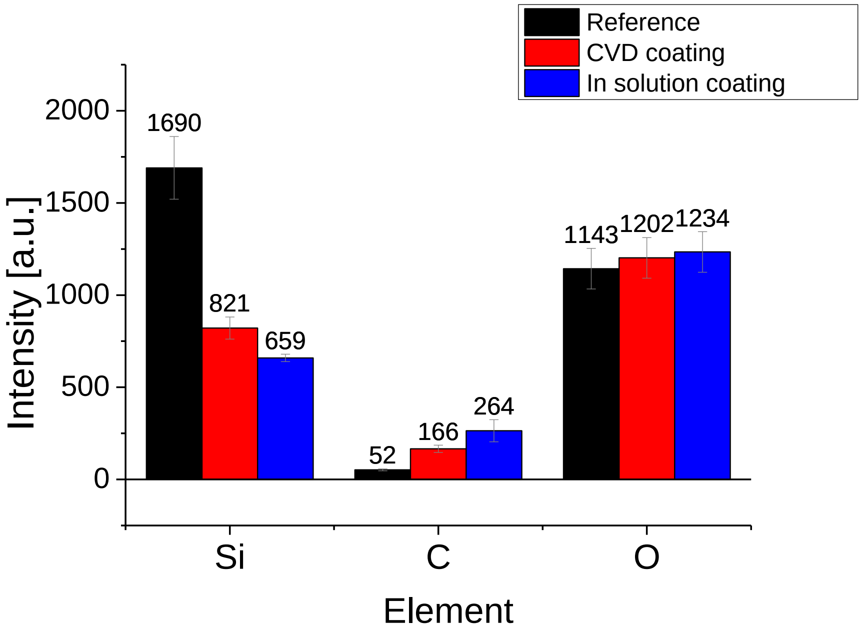

Figure 4.49: XPS analysis of patterned OEG-silane films on silicon substrate produced by chemical vapor deposition and in solution deposition. A bare silicon wafer serves as a reference.

In Figure 4.50 the SEM image of the patterned silane film is shown. Analogous to chemical vapor deposition hexagonally closed-packed ring-like pores was produced. The black spots in the center of the rings are non-silanized areas (protein adsorption sites) which were blocked by the mask particles during the silanization process. The SEM image indicates that the technique was working quite fine to fabricate large scale nanopatterns for protein adsorption. The in solution deposition has shown higher reproducibility in uniform OEG-silane nanopattern fabrication. Also compared to chemical vapor deposition a narrower size distribution of the nanopatterns was achievable by in solution deposition.

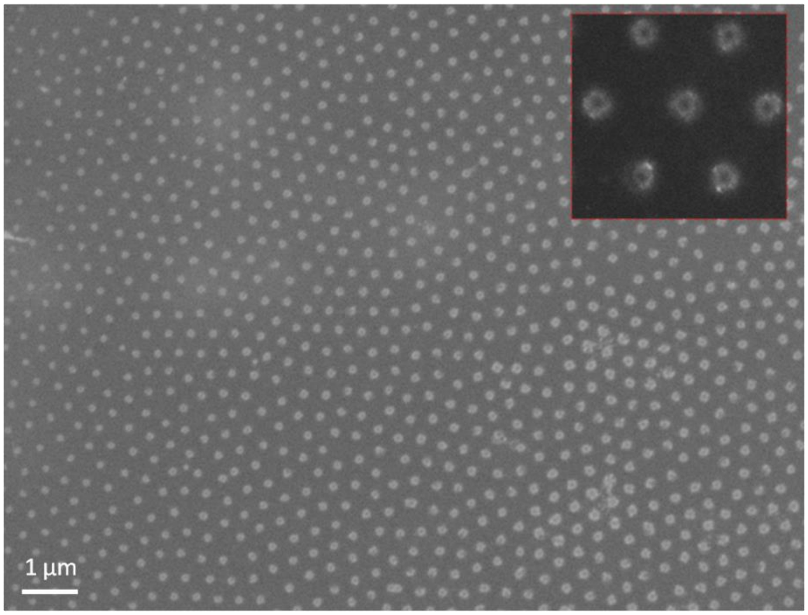

Figure 4.50: SEM image of nanopatterned OEG-silane films fabricated by in solution deposition of 2-[methoxy(polyethylenoxy)propyl]trichlorosilane. 500 nm mask particles were used.

The AFM analysis of the patterned OEG-silane film is shown in Figure 4.51 The height profile of the pore indicates that the depth of the pore is around 3 nm and the diameter is around 35-40 nm.

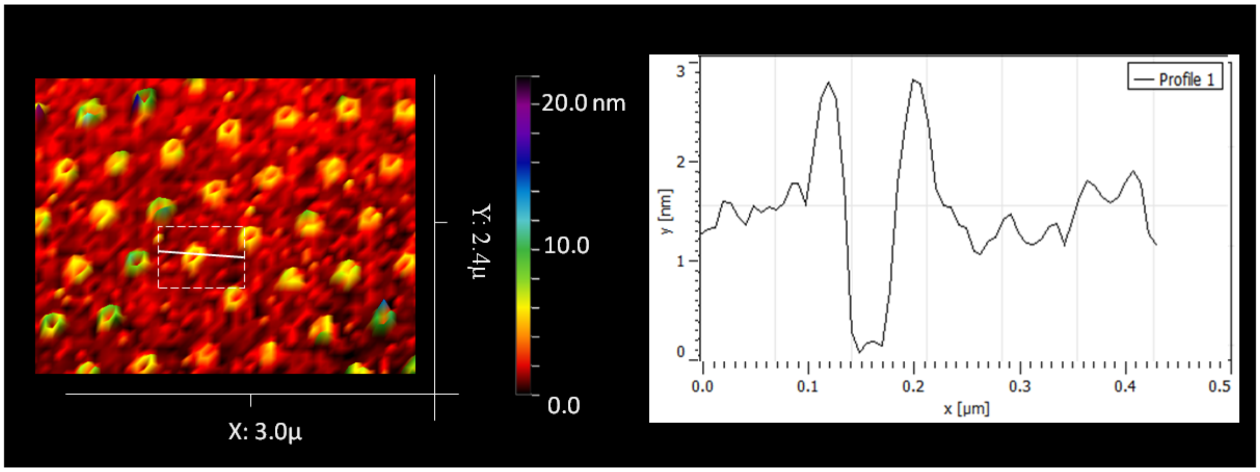

Figure 4.51: AFM image of a nanopatterned OEG-silane film fabricated by the in solution deposition method.

In solution deposition method was also employed to fabricate nanopatterns by using 200 nm silica particles. In figure 4.52 SEM image of a patterned OEG-silane film produced with 200 nm particles is shown. Reproducibility and yield are reduced when the mask particle diameter decreases.

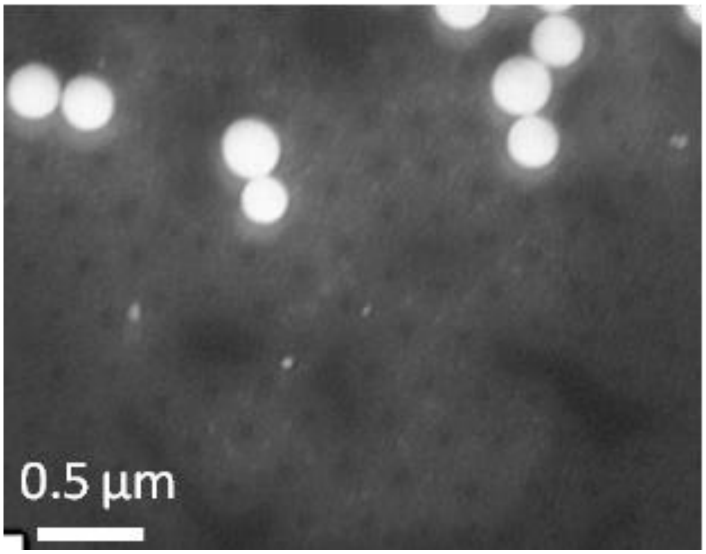

Figure 4.52: SEM image of nanopatterned OEG-silane films fabricated by in solution deposition of 2-[methoxy(polyethylenoxy)propyl]trichlorosilane. 200 nm mask particles were used.

The impact of the reaction time on in solution deposition was investigated by fabricating OEG-silane monolayers with different reactions times and analyzing the films by XPS and ellipsometry. Reaction times of 1, 2, 4, 8, 16 h were tested. In Figure 4.53 the XPS analysis of samples which were fabricated with different reaction times are shown. The signal intensities of the C1s region were compared. The carbon signal intensity was almost the same for all samples which were produced with more than 2 h reaction time. The thickness of the OEG-silane film reached a constant value of 2.1 mm after 4h reaction time.

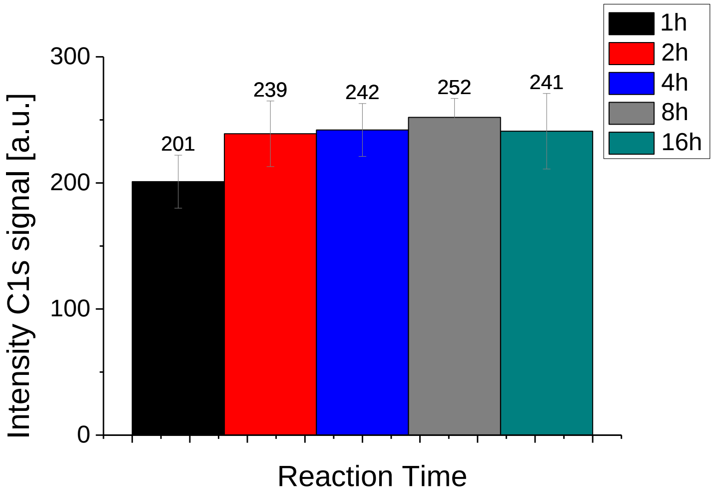

Figure 4.53: XPS analysis of patterned OEG-silane films on a silicon substrate. Silane coating was produced by in solution deposition with different reaction times.

The impact of annealing on structure quality was investigated by keeping the substrates at 100 ^{0}C for 3, 6 and 12 hours after the mask particles were deposited on the silicon substrates by self-assembly floating. Substrates prepared with different annealing times were analyzed under XPS after OEG-silane coating. C 1s signal intensities were compared and no significant difference was determined. Also the thickness measurements by ellipsometry were not able to detect any difference between the samples annealed for different times.

The adsorption site density and the adsorption site diameter values of patterned OEG silane films with different mask particles and different silanization methods are shown in Table 4.6. The diameters of the adsorption sites were measured by SEM and AFM.

Mask particle diameter and silanization method	Adsorption site per μm^2	Diameter of adsorption site measured by SEM	Diameter of adsorption site measured by AFM
500 nm, CVD	4	20-50 nm	-
500 nm, ISD	4	30-40 nm	35-40 nm
200 nm, ISD	30	20-30 nm	-

Table 4.6: Adsorption site density and diameter as a function of mask particle size and silane deposition method.

4.2 Site specific GOx adsorption on nanopatterned structures

In section 4.1 we have presented five different ways to fabricate large scale nanopatterned surfaces for site specific protein adsorption. Based on their excellent reproducibility and capability to produce uniform and high density nanopatterns, two techniques were selected for protein adsorption investigations. These are the techniques discussed in section 4.1.1 and 4.1.2. By these selected methods, porous metal-semiconductor nanopatterns with 25 and 60 nm adsorption site diameter and honeycomb-like dielectric nanopatterns with 60 and 100 nm adsorption site diameter were fabricated to perform protein adsorption studies. For convenience, these four substrates were named as Type A25, Type A60, Type B60 and Type B100, respectively, in this section. The structural properties of the selected substrate types and their theoretical protein immobilization capacities are given in Table 4.7.

	Type A25	**Type A60**	**Type B60**	**Type B100**
Matrix Coating	EG_7-SH	EG_7-SH	PAA-PEG2000	PAA-PEG2000
Adsorption Site Coating	PAH	PAH	PAH	PAH
Adsorption Site Diameter (nm)	25	60	60	100
Adsorption Site Depth (nm)	5-6	5-6	2-3	7-8
Adsorption Site Area (nm^2)	490	2820	2820	7850
Adsorption Site Coverage (%)	35	29	7	19
Number of Adsorption Sites/cm^2	7.2×10^{10}	1.0×10^{10}	2.4×10^{9}	2.4×10^{9}
n_{max}(GOx)/Adsorption Site	1	9	9	26
m_{max}(GOx)/cm^2 (ng)	15.5	19.4	4.9	14.1

Table 4.7: Surface parameters of Type A25, Type A60, Type B60 and Type B100 substrates and theoretical protein adsorption capacities.

After GOx incubation samples were investigated with XPS. The presence of the N1s signal was taken as a reliable marker for protein deposition and the peak intensity was used to compare the relative amount of GOx on the surfaces having different functionalization and surface pattern. In Figure 4.54 the N 1s signal intensities of Type A25 and Type A60 substrates and samples with homogeneous gold, EG7 and PAH coatings are shown. According to Figure 4.54 it was concluded that the EG7 coating provided a surface with good protein resistance. The relatively low N 1s signal intensities on nanostructured substrates in comparison to homogeneous PAH and gold coated substrates may considered as an evidence of site specific adsorption of GOx on Type A25 and Type A60 substrates.

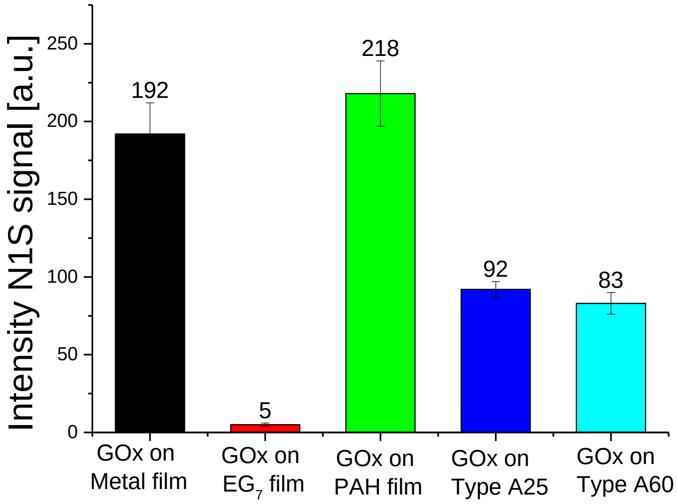

Figure 4.54: XPS analysis showing N1s signal intensity of GOx adsorbed onto Type A25 and Type A60 substrates. Homogeneous gold, EG7 and PAH coated silicon substrates incubated with GOx were used as reference samples.

In Figure 4.55 the N 1s signal intensities of GOx adsorbed to Type B60 and Type B100 substrates and samples with homogeneous PAA-PEG and PAH coatings are shown. The N1s signal intensities of the Type B60 and Type B100 substrates after GOx were lower than that of PAH coating and higher than that of PAA-PEG coating, this may concluded as an evidence of site specific adsorption of GOx on Type B60 and Type B100 substrates.

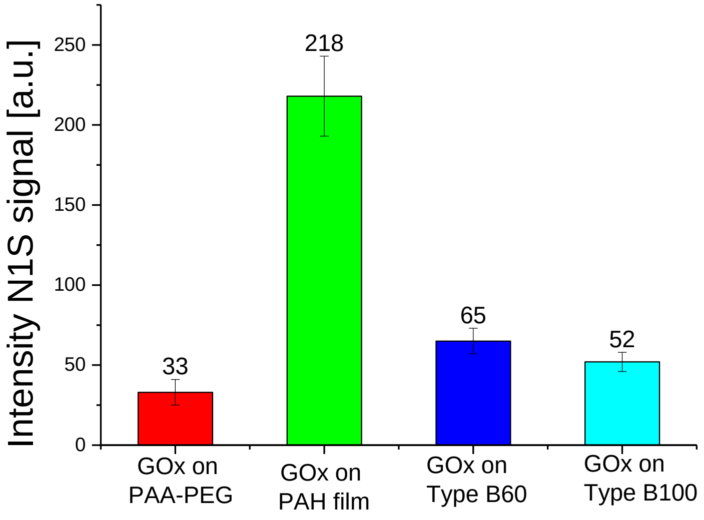

Figure 4.55: XPS analysis showing N1s signal intensity of GOx adsorbed onto Type B60 and Type B100 substrates. GOx-incubated, homogeneous PAA-PEG and PAH coated silicon substrates were used as reference samples.

4.2.1 Quantification of GOx on nanopatterned structures

The adsorbed amount of GOx on homogeneous PAH films as well as Type A25, Type A60, Type B60 and Type B100 substrates were determined by the use of enzyme linked immunosorbent assays (ELISA). As described in section 3.9, adsorbed GOx was first reacted with a specific primary antibody (anti-GOx rom rabbit), and then with a specific, HRPO-conjugated secondary antibody (HRPO-anti-rabbit). From the HRPO-mediated color reaction, the amount of surface-bound GOx was determined: The amount of generated ABTS$^+$ was proportional to the amount of surface-bound HRPO and, thus, to the amount of adsorbed GOx. For absolute quantification, the measured extinction per time due to ABTS$^+$ formation was compared to a calibration curve, which was obtained by measuring the corresponding reaction kinetics for well-defined concentrations of HRPO-anti-rabbit IgG in solution (Figure 4.56).

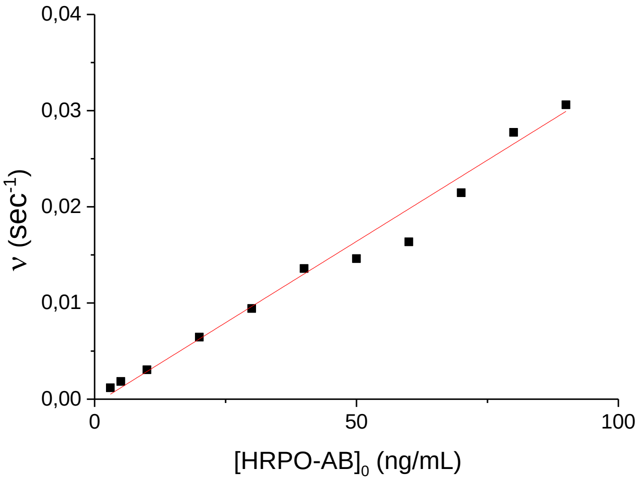

Figure 4.56: Calibration curve for the ELISA experiment.

In Table 4.8 the experimentally determined amounts of GOx on the four differently patterned substrates and the homogeneous PAH film are shown together with theoretical calculations. The GOx amounts on these four substrates were correlating well with the theoretically calculated values. For substrates Type A25, Type A60 and Type B100 it can be seen that there was positive deviation from the theoretical values by approximately 10-20 %. This may explained by possible unspecific adsorption of GOx onto the protein resistant matrix or surface defects. For the substrate Type B60 the determined GOx amount on surface was lower than the theoretical value and measurements was showed high variatiom. This may due to the low density of adsorption sites on substrate Type B60. The amount of GOx on this substrate was close to the detection limit of the ELISA technique.

Substrate	**C_{GOx} (ng/cm^2)**	**n_{exp}(GOx)/Ad.Site**	**n_{theor}(GOx)/Ad.Site**
Type A25	19±3	1.2±0.2	1
Type A60	23±5	10±2	9
Type B60	3±2	5.5±3	9

Type B100	17±5	31±5	26
PAH film	83±6	-	-

Table 4.8: Amount of GOx adsorbed onto different types of nanostructured substrates. A substrate coated with a homogeneous PAH film serves as a reference**.**

The quantitative determination of GOx on nanopatterned structures having different surface parameters showed quite well correlation with theoretical calculations. This can be considered as an evidence for the site specific adsorption of proteins on these chemically contrasted nanopatterned structures. It can be concluded that the proteins are immobilized in well-defined domains by generating adsorption sites which are embedded into protein resistant matrices.

4.2.2 Activity of GOx on nanopatterned structures

Activity of the adsorbed GOx was determined by UV/Vis spectroscopy. A two-step detection mechanism was required as the amount of generated H_2O_2 cannot be analyzed by simple means. Therefore, in a subsequent reaction, H_2O_2 in combination with horse radish peroxidase (HRPO) was used to induce a color reaction, in which 2,2'-azino-bis(3-ethylbenzthiazoline-6-sulphonic acid) (ABTS) is converted to the green radical cation $ABTS^+$ as described in section 3.10. The amount of generated $ABTS^+$ was followed by UV/Vis spectroscopy measuring the extinction at 405 nm wavelength. This value is proportional to the amount of generated H_2O_2. The concentrations were selected such that c[HRPO] >> c[GOx] so that the reactions kinetics were dictated by GOx.

As the reaction follows a Michaelis-Menten kinetics. Both the activity of GOx and its affinity to glucose was determined by a plot of reaction speed versus glucose concentration (Figure 4.57). The activity was obtained from the maximum reaction speed V_{max}, the substrate affinity from the glucose concentration C_M for which ½ V_{max} was observed. Note that $C_M = K_M$ and that the substrate affinity is inversely proportional to K_M.

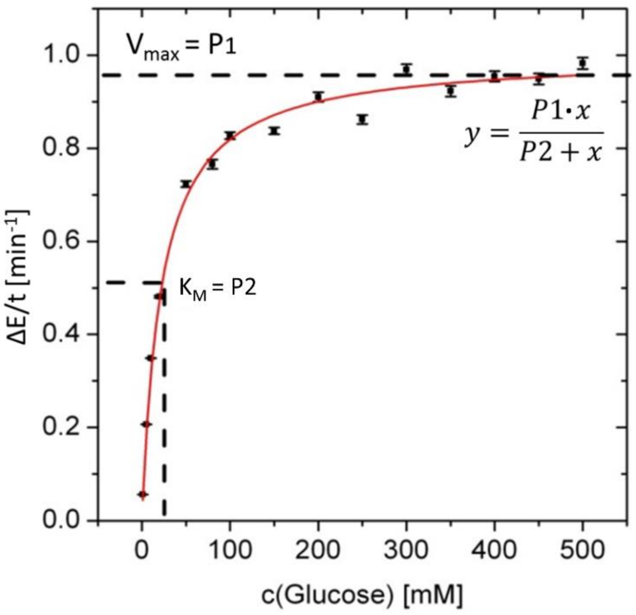

Figure 4.57: Michaelis-Menten plot to determine GOx activity and its affinity to glucose. The activity was obtained from the maximum speed V_{max} of $ABTS^+$ formation and the substrate affinity from the glucose concentration for which ½ V_{max} was observed. The fit parameters of Michaelis-Menten plot (P1 and P2) directly define the V_{max} and K_M (= C_M) values.

The specific activity of the model enzyme GOx was determined on the four different types of nanostructured substrates. By comparing these values with the activity of GOx in its native state, the impact of surface nanostructures on specific enzyme activity was determined. In Figure 4.58 the results of the activity measurements for GOx on the substrates type A25, type A60, type B60, type B100 and – as a reference – a homogeneous PAH film and GOx in solution phase (concentration: 100ng/ml) are shown. The reaction speeds at different glucose concentrations were plotted and a hyperbolic curve was fitted to the data set by using the equation: $y = (P1 \cdot x)/(P2+x)$. The Vmax and K_M values are also represented in Figure 4.57. By using the Vmax (P1) and K_M (P2) values and equation 3.3, the activity and the substrate affinity values were calculated. The results are given in Table 4.9.

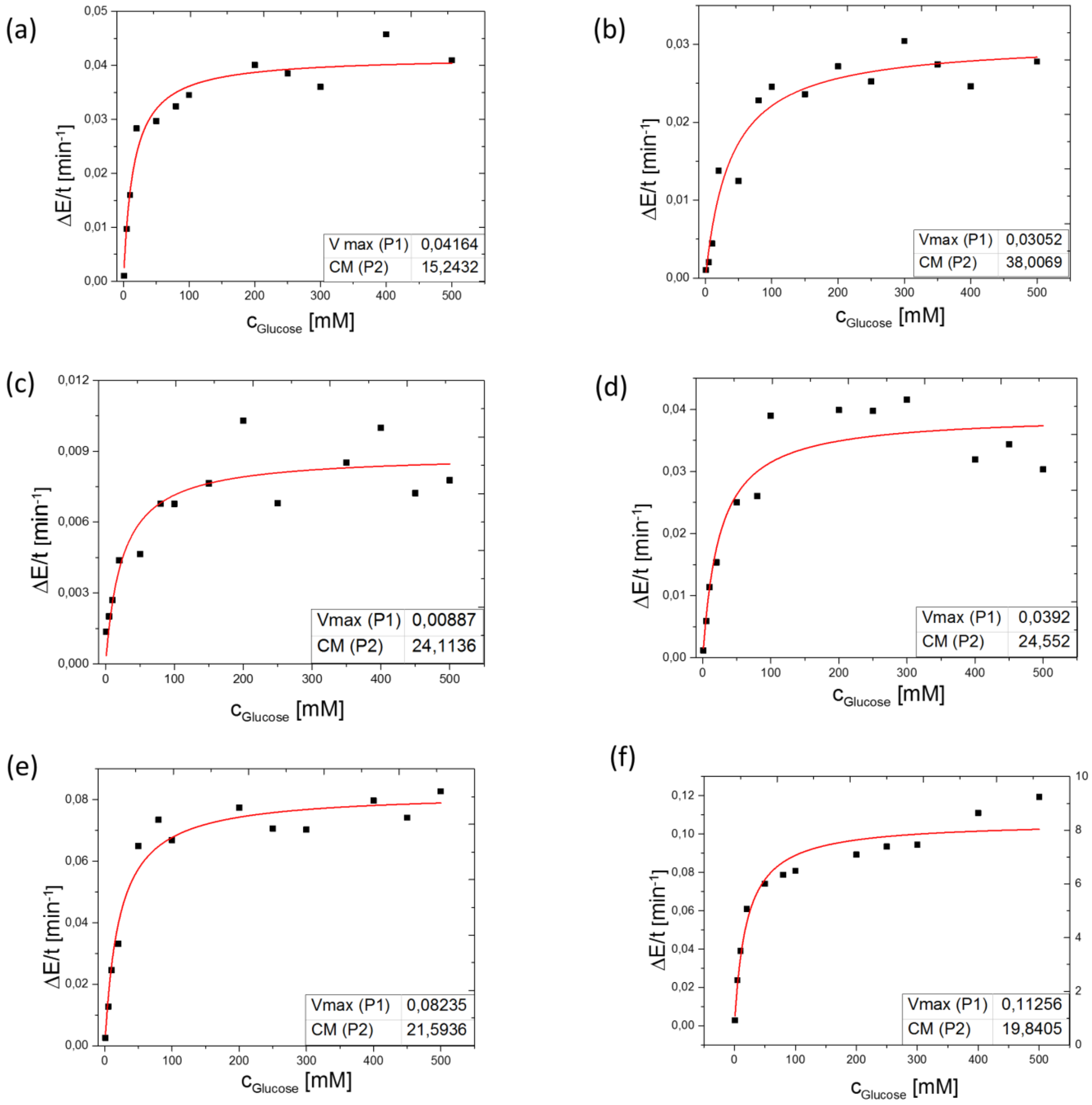

Figure 4.58: Activity of GOx a) on Type A25, b) on Type A60, c) on Type B60, d) on Type B100 samples, e) on a substrate coated with a homogeneous PAH film and f) in solution phase (GOx concentration: 100ng/ml). (pH = 5.5, T = 37 °C).

Sample	A(U/mg)	K_M (mM)
GOx on Type A25	113±12	15±3
GOx on Type A60	69±7	38±3
GOx on Type B60	75±10	24±2

GOx on Type B100	67±6	24±2
GOx on PAH film	39±3	21±2
GOx in solution	152±11	19±2

Table 4.9: Activity and substrate affinity of GOx on different substrates and GOx in solution phase.

To compare the GOx activity on nanopatterned structures to its native state, the activity value of GOx in solution was used for the concentration of 100ng/ml. Extensive studies on the activity of GOx in solution phase were done in our research group by Andrea Seehuber within the context of her PhD thesis and our results correlate well with her findings [86].

According to the results shown in Table 4.9, GOx on Type A25 showed the best activity values compared to the Type A60, Type B60 and Type B100 substrates. Also, the substrate affinity of GOx was also found highest corresponding to the smallest K_M value. When the activity and affinity of GOx on Type A25 substrates is compared to reference values of GOx in solution, it can be concluded that there was no significant change. In the activity measurements of GOx adsorbed on Type A60, Type B60 and Type B100 substrates, all samples showed almost same values when compared to each other. The activity values only almost half of the activity of GOx in solution. Yet, the activity of GOx on these three nanopatterned substrates still resulted in a much better activity than for GOx adsorbed on homogeneous PAH films. The K_M values obtained for type A60, type B60 and type B100 substrates were higher than the reference values (GOx in solution) which is indicating that the affinity of the GOx decreased by adsorption on these surfaces.

We may, thus, conclude that the confinement of GOx into nano-domains of patterned substrates has a significant effect on protecting the enzymatic activity of GOx. When the adsorption site diameter was selected similar to enzyme size, the activity of the protein was well protected and only a small loss of activity was observed. This is in line with the observation that proteins tend to unfold and lose their activity upon contact with surfaces which offer sufficient free surface area. The above results show that geometrical confinement is a promising strategy to overcome this problem and stabilize surface-bound enzymes.

5 SUMMARY AND CONCLUSIONS

The aim of this study was to investigate the impact of surface nanostructures on the activity of a model protein, Glucose oxidase (GOx). GOx was confined into nanoscale adsorption sites of well-defined size, chemical functionality and topography in order to prevent unfolding and loss of its biological function. For this purpose, novel approaches based on colloidal lithography were developed to fabricate five different types of nanopatterned surfaces: i) metal-semiconductor nanopatterns, ii) charge heterogeneous 2D and 3D nanopatterned polyelectrolyte multilayers (PEMs), iii) gold nanoparticle arrays on charge heterogeneous nanopatterned PEMs, iv) metal-dielectric hybrid nanopatterns, and v) nanopatterned OEG-silane self-assembled monolayers (SAMs).. One of the common properties of these surfaces is that they are all chemically contrasted, long-range ordered and large-scale (centimeter regime) with feature sizes between 10 and 100 nm. All of the fabricated nanopatterned surfaces were characterized by X-ray photoelectron spectroscopy (XPS), atomic force microscopy (AFM), scanning electron microscopy (SEM), ellipsometry and UV-visible spectroscopy.

Metal-semiconductor nanopatterns were fabricated by adsorption of randomly close-packed monolayers of monodisperse gold nanoparticles onto polyelectrolyte coated silicon substrates, followed by gold sputter coating and successive formation of a protein resistant ethylene glycol SAM on the gold metal surface. The embedded gold nanoparticles were removed from the surface by a newly developed particle removal method which was shown to remove nanoparticles down to 10 nm with an efficiency close to 100%. In this technique polystyrene or silica nanoparticles with 60 - 1500 nm in size were used as bullet nanoparticles in ultrasonic cleaning. The adsorption site diameter of the nanopatterned surfaces can be deliberately adjusted from 15 to 60 nm by properly selecting the experimental conditions. As demonstrated for 15 nm particles, adsorption site densities can be varied from 0 to 1000 per 1 μm^2 by changing incubation time.

Charge heterogeneous 2D and 3D nanopatterned polyelectrolyte multilayers (PEMs) were fabricated by combining colloidal lithography and layer-by-layer (LbL) deposition of polyelectrolytes to obtain honeycomb and brush-like patterned polyelectrolyte films with adjustable dimensions and charge patterns. The dimensions of the nanopatterns were changed from 2 to 10 nm in adsorption site depth, from 7 to 20% in adsorption site coverage and from 60 to 150 nm in adsorption site size. Additionally, charge patterns were changed by changing the order and number of polyelectrolyte layers in the LbL deposition process.

Gold nanoparticle arrays on charge heterogeneous nanopatterned PEMs were fabricated by successive selective deposition of gold clusters and resulted in a variety of 2D and 3D metal nanoparticle arrays, such as dot, grid, ring, multi-ring, out-of-ring, and circular patch structures. Geometry of gold nanoparticle arrays as well as density and dimension of specific adsorption sites were varied.

Metal-dielectric hybrid nanopatterns were fabricated by partially embedding 80 and 60 nm gold nanoparticles into a protein resistant matrix with thicknesses in the range of 70-75 nm and 50-55 nm respectively. The protein resistant matrix was generated by controlled poly(ethylene glycol)methacrylate (PEGMA) graft polymerization and its thickness was controlled by monomer concentration and duration of polymerization. The limited reproducibility of PEGMA layers with precise thicknesses negatively affected the yield of the nanopatterns produced. Even though gold nanoparticles were partially embedded into the protein resistant matrix as proposed, the poor control over the PEGMA thickness drastically decreased the success of generating adsorption sites with a narrow size distribution.

Nanopatterned oligo(ethylene glycol) (OEG) silane films were considered to be an alternative nanopatterned surface for site specific adsorption and fabricated by employing deposition of OEG-silane monolayers and colloidal lithography. Silica nanoparticles were deposited as a densely packed monolayer by self-assembly floating technique to serve as a mask in the next step, which is the deposition of OEG-silane monolayers by using either CVD or ISD. The ISD was found to show higher reproducibility in the fabrication of uniform OEG-silane nanopatterned surfaces than CVD. Moreover, compared to CVD a narrower size distribution, 20-30 nm, of the nanopatterns was achievable.

Protein adsorption studies were carried on metal-semiconductor nanopatterns and charge heterogeneous 2D and 3D nanopatterned PEMs. These surfaces were chosen due to their excellent reproducibility and the capability to produce uniform and high density nanopatterns. Specifically, porous metal-semiconductor nanopatterns with 25 nm (type A25) and 60 nm (type A60) adsorption site diameter and honeycomb-like dielectric nanopatterns with 60 nm (type B60) and 100 nm (type B100) adsorption site diameter were fabricated to investigate the enzymatic activity of surface-bound GOx. As a first step, the amount of GOx adsorbed to these nanopatterned surfaces were quantified by enzyme linked immunosorbent assays (ELISA). The ELISA measurements suggested the site specific adsorption of GOx. The specific enzymatic activity of GOx on these selected nanopatterned surfaces were identified to be 113±12 U/mg for type A25, 69±7 U/mg for type A60, 75±10 U/mg for type B60 and 67±6 U/mg for type B100. The specific activity of GOx on nanopatterned structures were compared with the specific activity of GOx on poly(allylamine hydrochloride) coated non-patterned surfaces (39±3 U/mg) and in solution phase (152±11 U/mg). Moreover, the values of the Michaelis-Menten constant K_M, which are inversely proportional to the substrate affinity of of GOx on these surfaces were calculated. As a conclusion, it was found that the confinement of GOx into nano-domains of patterned substrates has a significant effect on protecting the enzymatic activity of GOx. When the adsorption site diameter was selected similar to enzyme size, the activity of the protein was well protected and only a small loss of activity was observed. This observation is in line with the expectation that proteins tend to unfold and lose their activity upon contact with surfaces which offer sufficient free surface area.

6 REFERENCES

1. Fodor, S.P.A., *DNA sequencing - Massively parallel genomics.* Science, 1997. **277**(5324): p. 393-&.
2. Norde, W. and J. Lyklema, *PROTEIN ADSORPTION AND BACTERIAL ADHESION TO SOLID-SURFACES - A COLLOID-CHEMICAL APPROACH.* Colloids and Surfaces, 1989. **38**(1-3): p. 1-13.
3. C. P. Price and D. J. Newman, e., Principles and Practice of Immunoassay , Stockton Press,New York, , 1991.
4. Slack, S.M. and T.A. Horbett, *The Vroman effect - A critical review*, in *Proteins at Interfaces Ii: Fundamentals and Applications*, T.A. Horbett and J.L. Brash, Editors. 1995, Amer Chemical Soc: Washington. p. 112-128.
5. Sluzky, V., et al., *KINETICS OF INSULIN AGGREGATION IN AQUEOUS-SOLUTIONS UPON AGITATION IN THE PRESENCE OF HYDROPHOBIC SURFACES.* Proceedings of the National Academy of Sciences of the United States of America, 1991. **88**(21): p. 9377-9381.
6. Welle, A., M. Grunze, and D. Tur, *Plasma protein adsorption and platelet adhesion on poly bis(trifluoroethoxy)phosphazene and reference material surfaces.* Journal of Colloid and Interface Science, 1998. **197**(2): p. 263-274.
7. Ulman, A., *Formation and structure of self-assembled monolayers.* Chemical Reviews, 1996. **96**(4): p. 1533-1554.
8. Elemans, J., S.B. Lei, and S. De Feyter, *Molecular and Supramolecular Networks on Surfaces: From Two-Dimensional Crystal Engineering to Reactivity.* Angewandte Chemie-International Edition, 2009. **48**(40): p. 7298-7332.
9. Schreiber, F., *Structure and growth of self-assembling monolayers.* Progress in Surface Science, 2000. **65**(5-8): p. 151-256.
10. Barlow, S.M. and R. Raval, *Complex organic molecules at metal surfaces: bonding, organisation and chirality.* Surface Science Reports, 2003. **50**(6-8): p. 201-341.

11. Love, J.C., et al., *Self-assembled monolayers of thiolates on metals as a form of nanotechnology.* Chemical Reviews, 2005. **105**(4): p. 1103-1169.
12. *<Structure and growth of self-assembling.pdf>.*
13. Dobrynin, A. and M. Rubinstein, *Theory of polyelectrolytes in solutions and at surfaces.* Progress in Polymer Science, 2005. **30**(11): p. 1049-1118.
14. Kotz, J., S. Kosmella, and T. Beitz, *Self-assembled polyelectrolyte systems.* Progress in Polymer Science, 2001. **26**(8): p. 1199-1232.
15. Hales, K. and D.J. Pochan, *Using polyelectrolyte block copolymers to tune nanostructure assembly.* Current Opinion in Colloid & Interface Science, 2006. **11**(6): p. 330-336.
16. Schonhoff, M., *Self-assembled polyelectrolyte multilayers.* Current Opinion in Colloid & Interface Science, 2003. **8**(1): p. 86-95.
17. Claesson, P.M., et al., *Polyelectrolyte-mediated surface interactions.* Advances in Colloid and Interface Science, 2005. **114**: p. 173-187.
18. Ballauff, M. and O. Borisov, *Polyelectrolyte brushes.* Current Opinion in Colloid & Interface Science, 2006. **11**(6): p. 316-323.
19. Kwon, H.J. and J.P. Gong, *Negatively charged polyelectrolyte gels as bio-tissue model system and for biomedical application.* Current Opinion in Colloid & Interface Science, 2006. **11**(6): p. 345-350.
20. Van Tassel, P.R., *Polyelectrolyte adsorption and layer-by-layer assembly: Electrochemical control.* Current Opinion in Colloid & Interface Science, 2012. **17**(2): p. 106-113.
21. Ariga, K., J.P. Hill, and Q. Ji, *Layer-by-layer assembly as a versatile bottom-up nanofabrication technique for exploratory research and realistic application.* Phys Chem Chem Phys, 2007. **9**(19): p. 2319-40.
22. Cuomo, F., et al., *Vesicle-templated layer-by-layer assembly for the production of nanocapsules.* Langmuir, 2010. **26**(13): p. 10555-60.
23. Zhu, D., et al., *A versatile approach to fabricate ordered heterogeneous bull's-eye-like microstructure arrays.* Langmuir, 2010. **26**(7): p. 5172-8.
24. Peyratout, C.S. and L. Dahne, *Tailor-made polyelectrolyte microcapsules: from multilayers to smart containers.* Angew Chem Int Ed Engl, 2004. **43**(29): p. 3762-83.

25. Kotov, N.A., *Layer-by-layer self-assembly: The contribution of hydrophobic interactions.* Nanostructured Materials, 1999. **12**(5-8): p. 789-796.

26. Ke, B.B., et al., *Selective layer-by-layer self-assembly on patterned porous films modulated by Cassie-Wenzel transition.* Phys Chem Chem Phys, 2011. **13**(11): p. 4881-7.

27. Schmitt, J., et al., *INTERNAL STRUCTURE OF LAYER-BY-LAYER ADSORBED POLYELECTROLYTE FILMS - A NEUTRON AND X-RAY REFLECTIVITY STUDY.* Macromolecules, 1993. **26**(25): p. 7058-7063.

28. Lvov, Y., G. Decher, and H. Mohwald, *ASSEMBLY, STRUCTURAL CHARACTERIZATION, AND THERMAL-BEHAVIOR OF LAYER-BY-LAYER DEPOSITED ULTRATHIN FILMS OF POLY(VINYL SULFATE) AND POLY(ALLYLAMINE).* Langmuir, 1993. **9**(2): p. 481-486.

29. Prime, K.L. and G.M. Whitesides, *SELF-ASSEMBLED ORGANIC MONOLAYERS - MODEL SYSTEMS FOR STUDYING ADSORPTION OF PROTEINS AT SURFACES.* Science, 1991. **252**(5009): p. 1164-1167.

30. Herrwerth, S., et al., *Factors that determine the protein resistance of oligoether self-assembled monolayers - Internal hydrophilicity, terminal hydrophilicity, and lateral packing density.* Journal of the American Chemical Society, 2003. **125**(31): p. 9359-9366.

31. Schilp, S., et al., *Settlement and adhesion of algal cells to hexa (ethylene glycol)-containing self-assembled monolayers with systematically changed wetting properties.* Biointerphases, 2007. **2**(4): p. 143-150.

32. Dicke, C. and G. Hahner, *Interaction between a hydrophobic probe and tri(ethylene glycol)-containing self-assembled monolayers on gold studied with force spectroscopy in aqueous electrolyte solution.* Journal of Physical Chemistry B, 2002. **106**(17): p. 4450-4456.

33. Xia, Y.N. and G.M. Whitesides, *Soft lithography.* Annual Review of Materials Science, 1998. **28**: p. 153-184.

34. Mrksich, M. and G.M. Whitesides, *Using self-assembled monolayers to understand the interactions of man-made surfaces with proteins and cells.* Annual Review of Biophysics and Biomolecular Structure, 1996. **25**: p. 55-78.

35. Kane, R.S., et al., *Patterning proteins and cells using soft lithography.* Biomaterials, 1999. **20**(23-24): p. 2363-2376.
36. Morhard, F., et al., *Immobilization of antibodies in micropatterns for cell detection by optical diffraction.* Sensors and Actuators B-Chemical, 2000. **70**(1-3): p. 232-242.
37. Pipper, J., in *University of Heidelberg.* 2000.
38. Cicero, R.L., M.R. Linford, and C.E.D. Chidsey, *Photoreactivity of unsaturated compounds with hydrogen-terminated silicon(111).* Langmuir, 2000. **16**(13): p. 5688-5695.
39. Golzhauser, A., et al., *Chemical nanolithography with electron beams.* Advanced Materials, 2001. **13**(11): p. 806-+.
40. Harnett, C.K., K.M. Satyalakshmi, and H.G. Craighead, *Low-energy electron-beam patterning of amine-functionalized self-assembled monolayers.* Applied Physics Letters, 2000. **76**(17): p. 2466-2468.
41. Spatz, J.P., et al., *Ordered deposition of inorganic clusters from micellar block copolymer films.* Langmuir, 2000. **16**(2): p. 407-415.
42. Lohmüller, T., *Micelle lithogrraphy.* 2008: University of Heidelberg.
43. Burmeister, F., et al., *Colloid monolayers as versatile lithographic masks.* Langmuir, 1997. **13**(11): p. 2983-2987.
44. Li, F., D.P. Josephson, and A. Stein, *Colloidal assembly: the road from particles to colloidal molecules and crystals.* Angew Chem Int Ed Engl, 2011. **50**(2): p. 360-88.
45. Ye, X. and L. Qi, *Two-dimensionally patterned nanostructures based on monolayer colloidal crystals: Controllable fabrication, assembly, and applications.* Nano Today, 2011. **6**(6): p. 608-631.
46. Nidetz, R. and J. Kim, *Directed self-assembly of nanogold using a chemically modified nanopatterned surface.* Nanotechnology, 2012. **23**(4): p. 045602.
47. Maury, P., D. Reinhoudt, and J. Huskens, *Assembly of nanoparticles on patterned surfaces by noncovalent interactions.* Current Opinion in Colloid & Interface Science, 2008. **13**(1-2): p. 74-80.

48. Ozin, G.A., et al., *Nanofabrication by self-assembly.* Materials Today, 2009. **12**(5): p. 12-23.
49. Rybczynski, J., U. Ebels, and M. Giersig, *Large-scale, 2D arrays of magnetic nanoparticles.* Colloids and Surfaces A: Physicochemical and Engineering Aspects, 2003. **219**(1-3): p. 1-6.
50. Retsch, M., et al., *Template-free structuring of colloidal hetero-monolayers by inkjet printing and particle floating.* Soft Matter, 2010. **6**(11): p. 2403.
51. Huang, Z.P., et al., *Growth of large periodic arrays of carbon nanotubes.* Applied Physics Letters, 2003. **82**(3): p. 460.
52. Ho, C.C., et al., *Fabrication of monolayer of polymer/nanospheres hybrid at a water-air interface.* ACS Appl Mater Interfaces, 2011. **3**(2): p. 204-8.
53. Wang, X.D., C.J. Summers, and Z.L. Wang, *Large-scale hexagonal-patterned growth of aligned ZnO nanorods for nano-optoelectronics and nanosensor arrays.* Nano Letters, 2004. **4**(3): p. 423-426.
54. Liu, Y.F., et al., *A floating self-assembly route to colloidal crystal templates for 3D cell scaffolds.* Chemistry of Materials, 2005. **17**(20): p. 4918-4924.
55. Kralchevsky, P.A. and K. Nagayama, *CAPILLARY FORCES BETWEEN COLLOIDAL PARTICLES.* Langmuir, 1994. **10**(1): p. 23-36.
56. Guvenc, H.O., *Label-free Detection of Biospecific Interactions in Peptide Arrays Using Core-shell Nanoparticle Films*, in *University of Heidelberg.* 2013.
57. Denkov, N.D., et al., *MECHANISM OF FORMATION OF 2-DIMENSIONAL CRYSTALS FROM LATEX-PARTICLES ON SUBSTRATES.* Langmuir, 1992. **8**(12): p. 3183-3190.
58. Xie, F., et al., *Au nanostructures by colloidal lithography: from quenching to extensive fluorescence enhancement.* Journal of Materials Chemistry B, 2013. **1**(4): p. 536-543.
59. Tabrizi, A., F. Ayhan, and H. Ayhan, *Gold Nanoparticle Synthesis and Characterisation.* Hacettepe Journal of Biology and Chemistry, 2009. **37**(3): p. 217-226.
60. Jin, Y., et al., *Controlled Nucleation and Growth of Surface-Confined Gold Nanoparticles on a (3-aminopropyl)trimethoxysilane-Modified Glass Slide: A*

Strategy for SPR Substrates. Analytical Chemistry, 2001. **73**(13): p. 2843-2849.

61. Grabar, K.C., et al., *Preparation and Characterization of Au Colloid Monolayers.* Analytical Chemistry, 1995. **67**(4): p. 735-743.
62. Frens, G., *Particle size and sol stability in metal colloids.* Kolloid-Zeitschrift und Zeitschrift für Polymere, 1972. **250**(7): p. 736-741.
63. Kohli, R. and K.L. Mittal, *Developments in Surface Contamination and Cleaning: Methods for Removal of Particle Contaminants*. 2011: Elsevier Science.
64. Kohli, R. and K.L. Mittal, *Developments in Surface Contamination and Cleaning: Particle Deposition, Control and Removal.* 2009: Elsevier Science.
65. Kim, I., K. Hwang, and J. Lee, *Removal of 10-nm contaminant particles from Si wafers using CO2 bullet particles.* Nanoscale Res Lett, 2012. **7**(1): p. 211.
66. Hwang, K.-s., et al., *Removal of 10-nm contaminant particles from Si wafers using argon bullet particles.* Journal of Nanoparticle Research, 2011. **13**(10): p. 4979-4986.
67. Hwang, K.-s., et al., *Removing 20 nm ceramic particles using a supersonic particle beam from a contoured Laval nozzle.* Thin Solid Films, 2009. **517**(14): p. 3866-3869.
68. Yi, M.-Y., et al., *Molecular dynamics (MD) simulation on the collision of a nano-sized particle onto another nano-sized particle adhered on a flat substrate.* Journal of Aerosol Science, 2005. **36**(12): p. 1427-1443.
69. Vereecke, G., et al., *Evaluation of Megasonic Cleaning for Sub-90nm Technologies.* Solid State Phenomena, 2005. **103-104**: p. 141-146.
70. Brash, J.L., *Behavior of proteins at interfaces.* Current Opinion in Colloid & Interface Science, 1996. **1**(5): p. 682-688.
71. Gray, J.J., *The interaction of proteins with solid surfaces.* Curr Opin Struct Biol, 2004. **14**(1): p. 110-5.
72. Hlady, V. and J. Buijs, *Protein adsorption on solid surfaces.* Current Opinion in Biotechnology, 1996. **7**(1): p. 72-77.

73. Rabe, M., D. Verdes, and S. Seeger, *Understanding protein adsorption phenomena at solid surfaces.* Adv Colloid Interface Sci, 2011. **162**(1-2): p. 87-106.
74. Shen, L. and X.Y. Zhu, *Evidence of a mobile precursor state in nonspecific protein adsorption.* Langmuir, 2011. **27**(11): p. 7059-64.
75. Li, J.K., et al., *Differential Conductivity in Self-Assembled Nanodomains of a Diblock Copolymer Using Polystyrene-block-Poly(ferrocenylethylmethylsilane).* Advanced Materials, 2008. **20**(10): p. 1989-1993.
76. Kowalczyk, D., S. Slomkowski, and F.W. Wang, *Changes in Conformation of Human Serum Albumin (HSA) and Gamma Globulins (G) upon Adsorption to Polystyrene and Poly(styrene/acrolein) Latexes: Studies by Fluorescence Spectroscopy.* Journal of Bioactive and Compatible Polymers, 1994. **9**(3): p. 282-309.
77. Elwing, H.B., et al., *Protein displacement phenomena in blood plasma and serum studied by the wettability gradient method and the lens-on-surface method*, in *Proteins at Interfaces Ii: Fundamentals and Applications*, T.A. Horbett and J.L. Brash, Editors. 1995, Amer Chemical Soc: Washington. p. 138-149.
78. Malmsten, M., *PROTEIN ADSORPTION AT PHOSPHOLIPID SURFACES.* Journal of Colloid and Interface Science, 1995. **172**(1): p. 106-115.
79. Sheldon, R.A. and S. van Pelt, *Enzyme immobilisation in biocatalysis: why, what and how.* Chem Soc Rev, 2013. **42**(15): p. 6223-35.
80. Popat, A., et al., *Mesoporous silica nanoparticles for bioadsorption, enzyme immobilisation, and delivery carriers.* Nanoscale, 2011. **3**(7): p. 2801-18.
81. Beatriz M. Brena, F.B.-V., *Immobilization of Enzymes*, in *Immobilization of Enzymes and Cells*, J.M. Guisan, Editor., Humana Press: 2006.
82. Brady, D. and J. Jordaan, *Advances in enzyme immobilisation.* Biotechnol Lett, 2009. **31**(11): p. 1639-50.
83. Cao, L., *Immobilised enzymes: science or art?* Curr Opin Chem Biol, 2005. **9**(2): p. 217-26.

84. Secundo, F., *Conformational changes of enzymes upon immobilisation.* Chem Soc Rev, 2013. **42**(15): p. 6250-61.

85. Gan, S.D. and K.R. Patel, *Enzyme immunoassay and enzyme-linked immunosorbent assay.* J Invest Dermatol, 2013. **133**(9): p. e12.

86. Seehuber, A., *Konformation und aktivität von glucose oxidase auf homogen beschichteten und nanostrukturierten oberflachnen*, in *University of Heidelberg*. 2011, University of Heidelberg.

87. Hecht, H.J., et al., *CRYSTAL-STRUCTURE OF GLUCOSE-OXIDASE FROM ASPERGILLUS-NIGER REFINED AT 2 .3 ANGSTROM RESOLUTION*. Journal of Molecular Biology, 1993. **229**(1): p. 153-172.

88. http://www.rcsb.org/pdb/101/motm.do?momID=77.

89. Purich, D.L., *Enzyme Kinetics: Catalysis & Control*. 2010: Elsevier Inc.

90. Johnson, K.A. and R.S. Goody, *The Original Michaelis Constant: Translation of the 1913 Michaelis-Menten Paper*. Biochemistry, 2011. **50**(39): p. 8264-8269.

91. Rubinow, S.I. and J.L. Lebowitz, *TIME-DEPENDENT MICHAELIS-MENTEN KINETICS FOR AN ENZYME-SUBSTRATE-INHIBITOR SYSTEM*. Journal of the American Chemical Society, 1970. **92**(13): p. 3888-&.

92. Weilie Zhou, Z.L.W., *Scanning Microscopy for Nanotechnology Techniques and Applications*. 2006: Springer Science+Business Media, LLC.

93. Waly, N., *Optimization of core-shell nanoparticle layers for optical biosensing*, in *University of Heidelberg*. 2011, University of Heidelberg: University of Heidelberg.

94. Teppner, H.M.a.R., *Ellipsometry in Interface Science*. Max-Planck-Institut fôur Grenzàôachenforschung, Golm.

95. Paul E. West, *Atomic Force Microscopy*. 2006: P. West, 2006.

96. Owen, T., *Fundamentals of modern UV-visible spectroscopy*. 2000: Agilent Technologies.

97. N. Winograd, S.W.G., *Physical Methods in Modern Chemical Analysis, Vol 2*. 1980: Academic Press. Inc.

98. Harvey, D., *MODERN ANALYTICAL CHEMISTRY*. 2000: The McGraw-Hill Companies, Inc.

99. C. Richard Brundle, C.A.E., Jr., Shaun Wilson, *<Encyclopedia of Materials Characterization Surfaces, Interfaces, Thin Films.pdf>*. 1992, Butterworth-Heinemann 80 Montvale Avenue Stoneham, MA02180: Butxetworch-Heinemann, a division of Reed Publishing CUSA) Inc.

100. Polte, J., et al., *Mechanism of Gold Nanoparticle Formation in the Classical Citrate Synthesis Method Derived from Coupled In Situ XANES and SAXS Evaluation.* Journal of the American Chemical Society, 2010. **132**(4): p. 1296-1301.

101. Seehuber, A., D. Schmidt, and R. Dahint, *Poly(acrylic acid)-poly(ethylene glycol) layers on positively charged surface coatings: molecular structure, protein resistance, and application to single protein deposition.* Langmuir, 2012. **28**(23): p. 8700-10.

102. Seehuber, A. and R. Dahint, *Conformation and activity of glucose oxidase on homogeneously coated and nanostructured surfaces.* J Phys Chem B, 2013. **117**(23): p. 6980-9.

103. Christine, D., *Synthese großflächig nanostrukturierter Oberflächen mittels Selbstaggregation zur Steuerung von Proteinadsorptionsprozessen.* 2013, University of Heidelberg: University of Heidelberg.

104. Roper†, W.A.a.D.K., *Periodic Nanotemplating by Selective Deposition of Electroless Gold Island Films on Particle-Lithographed Dimethyldichlorosilane Layers.* ACS Nano.

105. Saner, C.K., et al., *Self-assembly of octadecyltrichlorosilane: Surface structures formed using different protocols of particle lithography.* Beilstein Journal of Nanotechnology, 2012. **3**: p. 114-122.

7 APPENDIX

TABLE OF TABLES

TABLE OF FIGURES

LIST OF ABBREVIATIONS

A	Absorbance
ABTS	2,2’-Azinodi(3-ethylbenzothiazoline)-6-sulfonic
AcBS	Acetate buffered saline
AFM	Atomic force microscopy
APTES	(3-Aminopropyl)triethoxysilane
BSA	Bovine serum albumin
BSE	Backscattered electron
CCD	Charge-coupled device
CRT	Cathode ray tube
CVD	Chemical vapor deposition
DCM	Dichloromethane
DLC	Dry laser cleaning
EDC	N-(3-dimethylaminopropyl)-N′-ethylcarbodiimid hydrochloride
EG	Ethylene glycol
EG7-SH	O-(2-mercaptoethyl)-O′-(2 carboxyethy)heptaethylene glycol
ELISA	Enzyme-Linked Immunosorbent Assay
ESCA	Electron spectroscopy for chemical analysis
HRPO	Horseradish peroxidase
HRPO-AB	Horse radish peroxidase-tagged antibody
I_0	Incident radiation
I	Transmitted radiation
ISD	In solution deposition
K_M	Michaelis-Menten constant
LBL	Layer-by-layer
LIP	Laser induced plasma
MTCS	2-[methoxy(polyethylenoxy)propyl] trichlorosilane
NHS	N-hydroxysuccinimide
OEG	Oligo(ethylene glycol)
PAH	Poly(allylaminehydrochloride)
PBS	Phosphate-buffered saline

PE	Polyelectrolyte
PEG	Poly(ethylene glycol
PEO-b-PPO	Poly(ethylene oxide)-block-poly(propylen oxide)
PEGMA	Poly(ethyleneglycol)methacrylate
PEM	Polyelectrolyte multilayer
PSS	Poly(styrenesulfonate)
R	Reflectance
RT	Room temperature
SAMs	Self-assembled monolayers
SDS	Sodium dodecyl sulphate
SE	Secondary electron
SEM	Scanning Electron Microscopy
SFM	Scanning force microscopy
SPS	Sulfonated polystyrene
T	transmittance
TSC	Tri-sodiumcitrate-dihydrate
UHV	ultra-high vacuum
UV-Vis	Ultraviolet–visible
V_{max}	maximum reaction rate
WLC	wet/steam laser cleaning
XPS	X-ray photoelectron spectroscopy
μCP	Microcontact printing

ACKNOWLEDGEMENT

I would like to extend thanks to the people who so generously contributed to the work presented in this thesis.

First and foremost I want to express my sincere gratitude to my supervisor Prof. (apl.) Dr. Reiner Dahint who has always showed maximum support that a supervisor can. In my life I have met few people who had such great patience and understanding.

I would like to thank the current and past members of Biosensor and Bioelectronics Research group for their help and scientific discussions. Namely; Andrea Seehuber, Anna Grab, Felicitas Scwörer, Elliard Roswell Yanza, Christine Dietrich and my dear friend Haci Osman Güvenc.

I would like to express my thankfulness to the remaining colleagues in Applied Physical Chemistry Institute for their support and collaboration during my study. Particularly to my office mates: Swen Schuster, Tobias Wächter and Can Yildirim

Lastly, I would like to thank my family for all their love and encouragement. For my parents who raised me with a love of science and supported me in all my pursuits. And most of all for my loving, supportive, encouraging, and patient wife Kübra whose faithful support during the final stages of this Ph.D. is so appreciated. Thank you.

Mustafa Sayin

University of Heidelberg
September 2014